Deterministic control of nanoantenna and single-photon emitter interaction at the nanoscale

PhD Thesis

By:

Nicola Palombo Blascetta

Advisor:

Niek F. van Hulst

ICFO - The Institute of Photonic Sciences

Universitat Politecnica de Catalunya

February 2021

Abstract

The study of light-matter interaction at the nanoscale is a very promising field of research, providing the possibility to manipulate the interaction with single quantum systems like single atoms, molecules, atomic defects or quantum dots, systems that can emit one photon at a time, so-called single-photon emitters (SPEs).
From the fundamental point of view, light-matter interaction at the nanoscale allows the exploration of the ultrasmall, providing super-resolution and decomposition of the ensemble. From the applied point of view, it offers the possibility to manipulate SPEs and control their optical properties for important applications in the field of ultrasensitive detectors development and quantum communications.

Yet, the ultrasmall SPEs have a relatively small absorption cross-section, making their interaction with light quite weak. In fact, even in a tight excitation focus at room temperature they only absorb one photon over ten million. Additionally, in many cases such emitters have a low quantum efficiency, making them hard to detect. Furthermore, they can be optically quite fragile and tend to blink and bleach, thus no high illumination powers can be used in order to increase their emission of light.

Fortunately, nanoantennas allow to confine light well below the diffraction limit, and through efficient coupling can increase the effective absorption cross-section of SPEs, allowing effective excitation and high-resolution imaging. Moreover, nanoantennas coupled to SPEs modify the local mode density, shortening the emitters excited state lifetime, increasing the internal quantum efficiency, resulting in bright SPEs.

In this thesis, we study the interaction of light and matter at the nanoscale through deterministic coupling between a SPE and

a nanoantenna, using nanometer scale control. We use scanning probe technology to scan a single nanoantenna in close proximity to a single emitter. First, we show a novel near-field probe based on a dipolar nanoantenna design that provides a higher optical and topographical resolution compared to the state-of-the-art. Next, we apply such novel antenna probes to the study of recently discovered single atomic defects in hBN, ultrastable SPEs in an atomically thin layer, ideal for nanoscale control. Despite the hBN high refractive index, and the low absorption cross-section of the defect, we provide high-resolution imaging of single hBN emission centers, enhanced by the hot-spot of our antenna probe. The controlled interaction is demonstrated by lifetime mapping, showing a shorter lifetime for the coupled emitter-antenna case. Finally, we develop a novel light confinement mechanism based on local subwavelength field suppression by near field interference: generating "cold" spots. We obtain such dark spots by antenna phase engineering through length control. We image optically for the first time and with high resolution the cold spots, and measure fluorescence lifetime reduction, inhibition of emission for the coupled system, despite the losses of the metallic nanoantenna. Such low-intensity sub-wavelength dark spots provide novel tools for high-resolution imaging of SPEs with ultralow intensity and nanoscaling of advanced super-resolution techniques like MINFLUX.

Contents

Chapter 1

Introduction

Light, propagating in the form of electromagnetic waves quanta called photons, plays a key role for the existence of life on earth allowing us to see the world. Nevertheless, our capability to visualize the world using light is limited to details of a few hundreds of nanometers due to the intrinsic diffraction limit ($\sim \lambda/2$). Challenging such limitation is particularly important in the field of light-matter interaction at the nanoscale where emitters with a size of a few nanometers like single molecules or atomic defects are studied. In this introductory chapter I will first start describing the interaction between light and single-photon emitters (SPEs), systems that emit one photon at a time. Next we show how nanoantennas can be used as ¨nanolenses¨ concentrating light at sub-wavelength level, overcoming the diffraction limit. The antennas can be used for high resolution nanoscale images of individual SPEs. Nanoantennas acting as nanocavities with sub-wavelength mode volume, are ideal candidates for SPEs manipulation through deterministic coupling. In fact the nanoantennas can modify the SPEs spontaneous emission lifetime, providing a tool for emission rate manipulation. The last paragraph of this introductory chapter describes the state-of-the-art of SPE-nanoantenna deterministic nanocavity coupling, briefly reviewing the literature and introducing the presented research in each chapter of the thesis.

1.1 Nanoscale light-matter interaction

The field of light-matter interaction at the nanoscale involves the study of single photon emitters and nanostructures in the spatial domain of few hundreds of nanometers, challenging the diffraction limit of light. Such emitters can be studied in ensemble configurations, when many of them are excited at the same time, or they can be studied at the level of single entities. A single emitter that is capable of emitting a single photon at a time is called single-photon emitter (SPE) and is essentially described as a two-level system [1]. Among SPEs we find atoms [2, 3], ions [4, 5], single molecules [6, 7], quantum dots (QD) [8, 9], color centers [10, 11] and more recently atomic defects in 2D materials [12, 13]. Together with a strong interest in fundamental research, the study of SPEs is also promising for advanced technological applications, such as the realization of bright and pure single-photon sources (SPS) [1] and for advanced sensing applications [14]. The understanding of interaction between SPEs and nanostructures is of paramount importance for the progress of light manipulation at the nanoscale [15].

When light illuminates a SPE, first the system gets excited to an electronic excited state with the absorption of a photon. Subsequently it decays to the ground electronic state with the spontaneous emission of another photon typically at lower energy. The time scale of the emission is probabilistically described by a characteristic time defined as lifetime τ, where the distribution of emitted photons decays exponentially with the time after excitation $\sim e^{-t/\tau}$. A two level system located in vacuum absorbs photons with a certain probability quantified by the absorption cross-section σ_{abs}:

$$\sigma_{abs} = \frac{\Gamma_{exc}\, h\nu}{I_0} \tag{1.1}$$

where Γ_{exc} is the excitation rate, i.e. the number of photons absorbed per unit time, h is the Planck constant, ν is the frequency of

the absorbed photons and I_0 is the illumination light intensity. One of the main limitations of the interaction between light and SPEs is the weak interaction with light, due to the low oscillator strength. Typical SPEs like single molecules embedded in transparent polymer have a $\sigma_{\text{abs}} \sim 10^{-16}\ cm^2$ at room temperature. Considering that the typical size of a diffraction limited spot is in the order of $\sim 10^{-9}\ cm^2$, this means that a single molecule absorbs on average only one of every $\sim 10^7$ incident photons. Such small absorption cross section makes it very hard to detect and image the emitters in absorption. Generally single molecules are detected in emission, counting the background free fluorescence photons [16]. It is highly beneficial to adopt valuable strategies to increase the efficiency of interaction between light and SPEs, like using the extreme light confinement of nanoantennas and manipulation through deterministic coupling.

On the emission side, a SPE in vacuum decays from the excited state to the ground one with the emission of a photon with a given intrinsic rate of emission Γ_{em0}. Nevertheless the emission rate is not an intrinsic property of the emitter.

In general, considering the spontaneous emission of a two-level quantum system the transition probability per unit time from an initial state $\langle i|$ to a set of final states $\langle f|$ can be described in terms of first order perturbation theory leading to the so-called Fermi golden rule:

$$\Gamma_{\text{em}} = \frac{2\pi}{\hbar^2} \sum_f |\langle f|\hat{H}_{\text{I}}|i\rangle|^2 \delta(\omega_{\text{i}} - \omega_{\text{f}})) \tag{1.2}$$

Where $\hat{H}_{\text{I}} = -\hat{\boldsymbol{\mu}} \cdot \hat{\boldsymbol{E}}$ is the interaction Hamiltonian in the dipole approximation and $\delta(\omega_{\text{i}} - \omega_{\text{f}})$ ensured the conservation of energy between the initial and final states.

The equation 1.2 can be written in terms of local density of states in the following form:

$$\Gamma_{\mathrm{em}} = \frac{2\omega}{3\hbar\epsilon_0}|\boldsymbol{\mu}|^2\rho(\omega_0) \tag{1.3}$$

where ω_0 is relative to the emitted photon, $\boldsymbol{\mu}$ is the dipole moment of the emitter and $\rho(\omega_0)$ is the partial local density of state as defined in reference [17], which depends on the emitter surrounding environment. In fact if a SPE is located in an homogeneous medium with a refractive index n>1 the local density of states changes with respect to vacuum and the emitter rate of emission changes correspondingly. The ratio between the rate of emission of the emitter in the homogeneous medium and the rate of emission of the emitter in vacuum is the so-called Purcell factor F_{p} [18]. A more complex case is represented by an emitter located inside a cavity [4] or in close proximity to a nanoantenna [19], both resonant objects with a specific quality factor $Q = \frac{\nu}{\Delta\nu}$. When the emitter is positioned in an antinode (constructive interference point) of a cavity or in a hotspot of a nanoantenna, F_{p} can be expressed as follows:

$$F_{\mathrm{p}} = \frac{3{\lambda_{\mathrm{f}}}^3}{4\pi^2}\frac{Q}{V_{\mathrm{m}}} \tag{1.4}$$

where λ_{f} is the transition wavelength, Q is the quality factor of the resonator and $\mathrm{V_m}$ is its volume, which in the case of the nanoantenna is the hotspot volume. Equation 1.4 indicates how the rate of spontaneous emission can be modified. In the case of photonic microcavities the Purcell factor is increased by the high quality factor Q of the resonator, while the cavity size is typically in the micrometer size. Nanoantennas operate in a different manner, their Q factor is relatively low, but the Purcell enhancement is given by the ultrasmall volume $\mathrm{V_m}$ of the hotspots that have a size of a few tenths of nanometers. While the typical lifetime τ of a SPE is in the order of 1-10 nanoseconds, deterministic manipulation and coupling to plasmonics nanostructures can decrease τ down by 3 orders of magnitude, in theory providing emitters that could operate with

an emission rate in the range of tens of GHz [20–22]. Of course the decay rate $\Gamma = 1/\tau$ is not the only factor limiting the rate of emission of a SPE and normally intrinsic non-radiative channels that compete with radiative decay come to play. The coupling between nanoantenna and the emitter provides lifetime shortening, which is particularly beneficial for SPEs with a very low internal quantum efficiency. In fact due to the coupling with a nanoantenna the emitter quantum yield can be substantially increased, allowing high resolution imaging of SPEs that would normally fall below the detection sensitivity threshold.

In the following section I will show how nanoantennas can be efficiently applied as SPEs manipulation tools.

1.2 Nanoantennas for light confinement

Conventional antennas are able to efficiently emit and retrieve electromagnetic signals in the radio wave regime, and nano-antennas do the same with visible light [23–25], with the extra complication of the strong dispersion and metallic absorption in the visible regime. Nanoantennas are sub-wavelength objects that support localized plasmonic resonances. They have a typical size varying from a few nanometers to $\lambda/2$ and are able to confine light in sub-wavelength volumes so-called ¨hot-spots¨, points of strongly increased electric-field intensity.

Hence, when properly designed and coupled to SPE, nanoantennas can enhance the effective SPE absorption cross section σ_{abs} as described in equation 1.1, concentrating the light in sub-diffraction limited spots $\sim$20x smaller than visible light and increasing the excitation rate [24]. Such property is particularly useful when nanoantennas are used as near-field probes, since they can provide SPEs super resolution imaging, with excitation spots typically as small as $\sim$20-30 nm, allowing subnanometer localization precision [26–28]. Furthermore, dipolar nanoantennas also provide

a vectorial nanostructuring of the near-field due to their typical dipolar scattering pattern, with typically a strong out-of-plane electric field component, allowing the detection of completely out-of-plane oriented molecules that would otherwise not be detected in normal confocal microscopy [29].

Nanoantennas can also be defined in a framework of cavity quantum electrodynamics (QED) [19], see equations 1.1, **??**, 1.4. In this picture, nanoantennas are characterized as low Q factor ∼5-20 resonators with a photon time of storage in the order of picoseconds, relatively short compared to high Q factor cavities with storage times in the order of microseconds. Importantly, nanoantennas are characterized by extremely small mode volumes V_m $\sim 10^2$-$10^4\, nm^3$. Indeed nanoantennas as cavities present very different characteristics when compared to the typical Fabry-Perot resonators [30]. While the latter have extremely high Q factors ($Q > 10^4$) and relatively high, micrometer size mode volumes V_m, nanoantennas show both low Q factors and V_m. According to equation 1.4, both nanoantennas and Fabry-Perot cavities have the capability to modify the intrinsic spontaneous emission rate Γ_{em0} of SPEs. On the other hand, the different LDOS enhancement mechanisms between the two systems determine different optical properties when they couple to SPEs. In contrast to conventional photonic cavities that exhibit a relatively slow response and a very narrow bandwidth, nanoantennas having a relatively low Q factor provide a very fast response (∼100 fsec), with a large bandwidth of operation. This is particularly beneficial for coupling with SPEs at room temperature where the emission bands are inhomogeneously broadened [19, 31]. On the other hand, equation 1.4 also shows that the extremely small V_m competes with low Q and can provide an increase in rate of spontaneous emission with a Purcell factor $F_p \sim 10^3$ [21, 22]. In other words, nano-antennas provide sub-wavelength volumes, that most of the times coincide with the hotspots, where they increase the radiative decay rate, increase internal quantum efficiency (QE)

of systems that have an intrinsically very low QE, and increase the brightness of SPEs increasing the rate of optical cycles [32, 33]. This aspect is important for detecting very dark emitters that otherwise would be below the minimum threshold of sensitivity [33], and for development of efficient SPEs [21]. Moreover, nanoantennas can direct light emission as well, increasing collection efficiency, and controlling polarization of emission [24].

As we have seen nano-antennas have a strong potential for manipulation of SPEs. In the following paragraph I will further describe deterministic SPE-nanoantenna coupling, introducing the thesis content.

1.3 Deterministic coupling of nanoantenna-SPE

In this thesis we focus on the use of near-field scanning optical microscopy (NSOM) in order to get controlled, deterministic coupling between a nanoantenna and a SPE. I will now shortly review the state-of-the-art coupling strategies, while a more in depth description is presented in section 2.1. The majority of experimental approaches provides stochastic or quasi-deterministic coupling. In fact the most popular techniques use colloidal or electron- beam lithography (EBL) fabricated nanoantennas with SPEs dispersed on top in thin polymeric layers [32], or in liquid solutions [34]. An approach that provides a more controlled coupling is the use of a DNA string that keeps together two metal nanospheres creating a dimer with a SPE linked to the DNA and located in the plasmonic gap, or more complex DNA structures with emitters attached, the so-called origami technology [35–37]. Lately researchers started to exfoliate 2D materials on EBL fabricated antenna arrays with the possibility to produce SPEs by the strain induced by nanoantennas [38]. More deterministic coupling is obtained with 2 step-EBL-lithography, where nanoantennas are fabricated by EBL that also controls with a certain efficiency SPEs positioning [39]. A

fully deterministic but static technique is given by the atomic-force microscopy (AFM) assisted assembly of nanoantennas, like dimers, containing a SPE embedded in the gap [40, 41]. On the other hand, the use of NSOM provides full deterministic control at nanometer level, with additionally the possibility to control the coupling in a dynamic configuration. Such technique also provides high resolution imaging of the coupled system. In principle one can scan a SPE located on the apex of a NSOM probe in close proximity to a single nanoantenna [42, 43]. Nevertheless, this approach presents the disadvantage that the position of a SPE at the apex of a probe is non trivial. Most importantly after a given number of optical cycles in the order of 10^6 the SPE typically bleaches and the fabrication of another probe is required.

To avoid bleach problem we decided to work with a slightly different configuration where we fabricate a single nanoantenna on the apex of our NSOM probe and scan it in close proximity to SPEs embedded in the sample surface [29, 44]. At the state-of-the-art, on the excitation side dipole nanorod antennas used as NSOM probes provide high resolution imaging with two bright hotspots of 40 nm lateral size and fluorescence enhancement that reaches two orders of magnitude compared to far-field confocal microscopy [27, 29]. Of course their capability to image SPEs is still limited by the presence of two close ($\sim$200 nm) hotspots per emitter, which is particularly inconvenient especially in case of densely packed systems. Additionally, the relatively big contact area of dipolar probes ($\sim$200x50 nm^2) limits the topographical resolution of the probes and their capability to approach the surface, increasing the vertical distance between the nanoantenna-SPE, a key parameter for the coupling. As described in chapter 3, in order to overcome these limitations we developed a novel dipolar probe configuration that is tilted with respect to the horizontal plane. Such probe improves optical and topographical resolutions with respect to near-field dipolar

probes state-of-the-art, by providing a resonant object with single a hotspot, with confined and enhanced electric field.

1.3.1 Deterministic coupling with accessible ultra stable SPEs

One of the most crucial parameters in the coupling between SPE and nanoantenna is their relative distance. The optimal enhancement is typically observed at 5 nm distance, while the near-field of a nanoantenna decays in a couple of tens of nanometers, hence the capability to locate the probe in close proximity to the emitter is a key aspect for their effective coupling. Part of the problem can be solved with an accurate antenna-sample surface vertical distance control. On the other hand, in order to have the antenna-emitter vertical distance minimized we need to have SPEs located in very thin matrices. What typically happens with SPEs is that decreasing the thickness of the protective volume around the optically active region results in less optically stable emitters. In order to overcome such limitation we decided to work with a novel kind of SPEs, the atomic defects in the 2D materials. Such emitters are located in a few or single atomic layers, having the active area directly exposed at the surface and easily accessible for antenna coupling. One of the most interesting emitters in 2D materials are the ones embedded in hexagonal boron nitride (hBN) characterized by their outstandingly robust and stable single-photon emission [12, 45].

Even though far-field super resolution imaging shed some light on the spatial arrangement of such SPEs in hBN flakes [46], the spatial extent and orientation of hBN defects emission centers is still not well understood. On the emission side, a couple of approaches have been tried in order to couple a single hBN emission center to a nanoantenna. In the first case atomic force microscopy has been used in order to assemble a dimer of plasmonic particles around

a single hBN emitter located on a small piece of hBN flake [40]. In the second case a wet transfer technique has been employed in order locate an hBN flake with atomic defects on top of an array of lithographically fabricated nanoantennas [47]. Both the studies showed that the hBN emitters lifetime can be shortened by the coupling with a nanoantenna. Nevertheless, both the configurations used are static and the data analysis doesn't adopt any specific strategy to discriminate between the metal luminescence and the one of the hBN defects. As shown in chapter 4, we challenged the limits of antenna-SPE deterministic coupling at the nanoscale, showing for the first time a fully controlled coupling, providing high resolution images of the SPEs [48]. We also for the first time actively modified and mapped the lifetime of hBN defects [49] by nanoantenna coupling, in a dynamic configuration with nanometer precision. We additionally introduced time-gating techniques in order to efficiently separate the hBN emitters light from the metallic luminescence background. We provided more insight in the physical extent and orientation of hBN emission centers.

1.3.2 An interferometric description of deterministic coupling

The typical approach for the manipulation and high resolution imaging of SPEs through nanoantenna coupling is based on the confinement and enhancement of light. The electric field is squeezed in sub-wavelength sized regions called ¨hotspots¨, that correspond to the maxima of field distribution around antenna accessible to the emitter. According to equations 1.1 and 1.4 an emitter located in a hotspot will absorb and emit more light compared to an emitter in vacuum or in an homogeneous material with a given refractive index. Interestingly, considering an interferometric description of nanoantenna-emitter coupling it is equally possible to manipulate

a SPE into a local intensity minimum, a sub-wavelengths ¨coldspots¨. In order to engineer such coldspots it is important to exploit the resonant nature of the nanoantenna. The phase of the local antenna field varies spatially on sub-wavelength scale. The exact phase value depends on the resonance, and therefore on the antenna shape. Thus phase is an additional knob to the manipulation of light at the nanoscale. Compared to other non-resonant antenna probes such as pyramidal ones [50], our probes exhibit a plasmonic resonance that can be tuned through length control [27]. Such resonance condition plays an important role both in the excitation and emission response of nanoantenna-SPE coupling. In fact, when a nanoantenna is illuminated by an incoming laser beam with a given electric field $\mathbf{E}_{\text{inc}}$, it scatters light with an electric field $\mathbf{E}_{\text{sc1}}$, and the total intensity I_{tot1} at a given point in space is given by the following relation:

$$I_{\text{tot1}} = |\mathbf{E}_{\text{inc}}(\mathbf{r},\omega_0)|^2 + |\mathbf{E}_{\text{sc1}}(\mathbf{r},\omega_0)|^2 + 2\sum_i |E^i_{inc}(\mathbf{r},\omega_0)||E^i_{sc1}(\mathbf{r},\omega_0)|\cos(\Delta\phi_{1i}) \quad (1.5)$$

Where ω_0 is the frequency of the excitation field, i = x, y or z for the vectorial components of the field and $\Delta\phi_1$ is the phase accumulated between $\mathbf{E}_{\text{inc}}$ and $\mathbf{E}_{\text{sc1}}$. This means that a SPE located in close proximity to a nanoantenna will locally detect an electric field that is the combination of two pure terms relative to $\mathbf{E}_{\text{inc}}$ and $\mathbf{E}_{\text{sc1}}$ respectively, but also a contribution related to their interference. While the pure terms are necessarily positive, the interference term can also be negative. For local electric field enhancement obtained in excitation resonant condition $\mathbf{E}_{\text{sc1}} >> \mathbf{E}_{\text{inc}}$, interference term can be ignored. However, for regimes where $\mathbf{E}_{\text{sc1}} \sim \mathbf{E}_{\text{inc}}$ the interference term is not negligible anymore and does play a role. When the

scattered light phase $\Delta\phi_1 = \pi$ the interference term is maximum and has a negative sign, hence it can be used to nullify the local intensity of light, generating sub-wavelengths coldspots. A SPE located in a coldspot is practically in complete darkness, even though it is illuminated by a focused laser spot. Such sub-wavelength low excitation spot could be used to localize SPEs with high precision while requiring low emission of photons. Coldspots might be of interest for downscale of super resolution localization microscopy techniques like MINFLUX [51], particularly promising for rapidly bleaching emitters. An initial proof of principle has been shown by Haggui et al. [52], where they used a photochemical near-field imaging technique in order to indirectly visualize the coldspots. The authors coated some metallic nanocubes with a thin layer of azobenzene containing photosensitive polymers. Under laser illumination the azo molecules went through cycles of isomerization and subsequent nanodisplacements inducing topographical changes that were characterized by atomic force microscopy. Supporting their data with electromagnetic simulations they retrieved the positions of coldspots. Nevertheless, this was an indirect, non-optical imaging of the coldspots, obtained in a static configuration. Thus a direct optical imaging of coldspots and an experimental demonstration of their potential for high resolution microscopy is missing.

Near-field interference and local phase equally influence the emission properties of a coupled SPE Nanoantenna system. The main difference is that when a SPE is emitting in close proximity to a nanoantenna producing an electric field $\mathbf{E}_{\mathrm{em}}$, the nanoantenna itself is now illuminated by the emitter instead of by the laser and scatters emitted light with electric field $\mathbf{E}_{\mathrm{sc2}}$. In a specific point in

space the total intensity of emitted light I_{tot2} is the following:

$$I_{\mathrm{tot2}} = |\mathbf{E}_{\mathrm{em}}(\mathbf{r},\omega)|^2 + |\mathbf{E}_{\mathrm{sc2}}(\mathbf{r},\omega)|^2 + 2\sum_i |E^i_{em}(\mathbf{r},\omega)||E^i_{sc2}(\mathbf{r},\omega)|\cos(\Delta\phi_{2i}) \quad (1.6)$$

Where now ω the frequency of the emitted field, normally slightly red-shifted with respect to excitation, and $\Delta\phi_2$ is the phase accumulated between $\mathbf{E}_{\mathrm{em}}$ and $\mathbf{E}_{\mathrm{sc2}}$. The interference as a function of emission wavelength and emitter position modifies the decay channels, as shown in a insightful picture by Drexhage many decades ago [53]. In his work Drexhage showed how it is possible to both increase and decrease the emitter lifetime by interference with a metal mirror surface. In principle, such phenomenon allows both increase or decay of emitter lifetime. It has been widely shown in literature that nanoantennas can provide Purcell factor F_{p} ∼1-2 orders of magnitude, similarly speeding up the optical cycles [21, 44, 54]. Much less has been done to show that the optical cycles can be slowed down, especially with metallic plasmonic antennas, since they have a very small Q factor and strongly scatter the light. The increase of lifetime with a consequent decrease in emission rate is important for the realization of threshold-less lasers [55]. In chapter 5 we show for the first time how we tuned nanoantenna phase in order to obtain coldspots, that we imaged with high resolution using a single molecule [56]. We additionally describe how our detuned aluminum antenna provided for the first time a reduction of SPE lifetime despite the high scattering behaviour of a metallic nanoantenna.

1.4 Thesis organization

This thesis has four main chapters, organized as follows:

- **Chapter 2**

  This chapter starts with description of the local field simulations that we use for design of nanoantennas optical properties as antenna resonance, near-field enhancement and light confinement. The robust and reliable four steps nanofabrication technique that we use for their realization is discussed. Lastly, we present our experimental technique for deterministic antenna-SPE coupling, describing its components and functioning together with the typical optical measurements presented in the thesis.

- **Chapter 3**

  This chapter focuses on development of two novel near-field optical probes for enhanced high resolution microscopy, based on titled nanoantennas and sharp metal-glass transition for extreme light confinement. We describe their design and fabrication techniques, together with experimental measurements using molecular probes, showing their novel optical properties. Inspired by cutting edge nanofabrication technologies, a theoretical study of ultimate light confinement and enhancement with use of sharp nanoantennas is introduced.

- **Chapter 4**

  In this chapter is presented the near-field high resolution imaging and emission control of hexagonal boron nitride (hBN) single emission centers by means of resonant and non-resonant nanoantenna probes. We show how we apply the strategy of photon time-tagging detection for a highly efficient photon discrimination and high resolution lifetime imaging. We discuss our data analysis with theoretical models that explain

excitation and emission coupling, with the proposal of a realistic novel configuration that provides emission enhancement.

- **Chapter 5**

  Here we show our work on antenna scattering phase and intensity tune through length control. We describe how we locally modulate interference using a single dibenzoterrylene (DBT) molecule as detector for mapping antenna sub-wavelength volumes with strong excitation field enhancement (hotspots) or reduction (cold-spots). Finally, we describe how antennas can be engineered using the same principles to provide partial emission inhibition at single molecule level.

Chapter 2

Nanoantenna probes and experimental methods

This chapter describes the strategies adopted for nanoantennas control and manipulation of single-photon emitters (SPEs) that are extensively used in the rest of the thesis. At the beginning there is a review of the different state-of-the-art approaches used for SPEs-nanoantenna coupling. Then the design of the nanoantennas is described, that allows to tune their optical spectral resonance and optimize their performance with respect to the emitters. Then are presented the advanced nanofabrication techniques that we use in order to realize nanoantennas, providing us with a full control, robust and reliable working methodology. The sample preparation techniques are presented, for the types of SPEs used in the rest of my work. Then are described the experimental technique that we employ to manipulate SPEs with deterministic control and nanometer precision, the near-field scanning optical microscopy (NSOM). Finally, the experimental setup and its operation modes are described, showing some examples of near-field high resolution images and time-resolved measurements.

2.1 Experimental methods for SPE-nanoantenna coupling

In literature different strategies have been adopted in order to control antenna-SPE coupling. In the majority of the cases the coupling is not deterministic but rather the result of a random event. This section starts reviewing the more standard approaches based on stochastic coupling, moving towards the fully deterministic position controlled antenna-emitter coupling.

A quite versatile approach depicted in Figure 2.1a is given by the use of electron-beam lithography (EBL) for nano-antennas fabrication. Such technique allows control of antenna size, shape and position with a precision in the order of 10 nm, allowing antenna resonance tuning. The coupling with SPE is obtained by spin-coating a thin layer of transparent polymer containing SPEs like single molecules or quantum dots (QD) on such antenna arrays [32, 57, 58]. The control of SPE concentration in the polymer allows to have on average a single emitter coupled to a single antennas. However the method lacks deterministic control on relative antenna-emitter position and only provides stochastic coupling.

A slightly different possibility is given by the use of EBL fabricated antenna arrays with on top single molecules free to diffuse in a liquid solution [34, 59], as presented in Figure 2.1b. Such technique has the advantage to be a dynamic system with higher interaction probability, where more coupling events can happen in time compared to the previous case, increasing the total number of events. On the other hand, there is no control on molecule motion in liquid, and depending on their diffusion time, the duration of every coupling event is limited to few μs-ms. This sets a limit to the maximum number of photons detected, hence a maximum to signal-to-noise ratio per event that is often too low for time-dependence or photons statistics measurements.

A relatively recent approach depicted in Figure 2.1c is given by direct exfoliation of so-called 2D materials on EBL fabricated metallic nano-antennas [38, 60]. It has been demonstrated that the strain induced by nanostructures can locally generate SPE [61]. Such technique has the advantage to provide simultaneous emitter generation and partial coupling to antenna, even though the position where the defect is generated due to strain non necessarily coincides with antenna hotspots. Furthermore, such technique provides a relatively low efficiency of SPE formation by strain and lack of versatility due to fixed configuration.

A much more deterministic technique described in Figure 2.1d is the 2 steps EBL procedure [39]. In this case both antenna array fabrication and emitter (QD) positioning are controlled by EBL. It basically solves the problem of antenna-emitter relative distance, even though a fundamental issue of reproducibility remains unresolved. On top of that, it only allows the generation of fixed antenna-emitter configurations and only works with emitters compatible with EBL procedures like QDs.

A different interesting approach shown in Figure 2.1e is based on the use of chemically synthesized colloidal particles with high plasmonic performances, self-assembled by DNA-origami with single molecules linked to them [35–37, 62]. Such technique doesn't require complicated nanofabrication techniques to build optically active nanostructures, however the number of possible geometries is limited and once built the antenna-emitter configuration is fixed.

Another very different possibility shown in Figure 2.1f is to use atomic force microscopy (AFM) in order to manipulate single emitters and metallic nanoantennas in order to assemble them in a coupled system [40, 41]. This approach provides a nanometer control on relative position, however it presents low reproducibility and fixed configuration as all previous cases.

So far we discussed mainly stochastic or fixed antenna-emitter configurations, now the dynamic and fully deterministically con-

trolled coupling strategies will be described. Near-field scanning optical microscopy (NSOM), depicted in Figure 2.1g and Figure 2.1h, allows the scan of a nanostructured object in close proximity to sample surface (∼10 nm) with deterministic nanometer control. The deterministic control provides the unique possibility to couple antenna and emitter in a dynamic configuration, building a complete interaction mapping. One possible NSOM configuration is given by the scan of a SPE like a single-molecule or QD on top of plasmonic structures [42, 43].

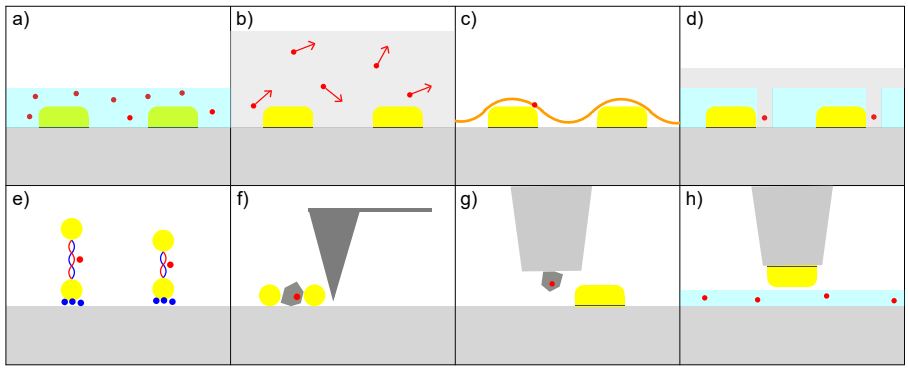

Figure 2.1: Experimental approaches for SPE-nanoantenna coupling. (a) EBL fabricated array of nanoantennas with a thin polymeric layer with SPEs embedded. (b) EBL fabricated array of nanoantennas with an aquarium containing SPEs diffusing in solution. (c) EBL fabricated array of nanoantennas with 2D materials exfoliated on top, at antenna edges the strain stochastically generates SPEs. (d) EBL 2 steps lithography procedure, a single SPE is located in close proximity to nanoantennas. (e) DNA-origami self-assembled dimers with a SPE located in the gap. (f) AFM deterministically assembled systems with a SPE positioned in a dimer. (g) NSOM probe with a single SPE, deterministically scanned in close proximity to a nanoantenna. (h) NSOM probe with a single nanoantenna, deterministically scanned in close proximity to SPEs. (a-h) The relative sizes of objects have been modified for the sake of clarity.

It provides high resolution imaging of dynamically coupled antennas and SPE. On the other hand, the measurements are limited

by the total amount of photons provided by a SPE, that normally tends to bleach after a few seconds or minutes of measurements. Additionally the positioning of a single emitter exactly at the tip apex is non trivial and once it bleaches it need to be replaced.

Our approach presented in Figure 2.1h keeps the benefits of the NSOM technique, without the drawbacks of working with a single emitter per probe. Our NSOM configuration consists in the use of a single metallic nanoantenna fabricated as near-field probe, scanned over single SPEs embedded in sample surface [54, 63, 64]. Such choice allows us to have deterministic control on antenna-emitter coupling, with nanometer precision, in a dynamic configuration, with high resolution and the chance to move to a new emitter when one bleaches. Additionally we obtain sub-wavelength interaction maps of the antenna-emitter coupling. Indeed the design and especially the fabrication of nanoantennas as near-field probes, together with the experimental setup operation can result quite critical.

2.2 Design of near-field nanoantenna probes

Nanoantennas are very effective nanostructures for light manipulation at the nanoscale. They provide high level of light confinement ($\lambda/10$) that can be exploited for high resolution imaging, field enhancement and for very sensitive microscopy [29]. Since the antennas modify the local density of optical states (LDOS), they can affect and enhance the decay rate, increasing the brightness of emitters with a low quantum efficiency (QE) [33]. Such outstanding optical properties are very sensitive to the resonance conditions of the nanoantenna, that has to be designed and adapted with respect to the optical properties of the emitter and the surrounding material. The nanoantenna resonance can be scanned with the excitation laser, to match the maximum of emitter absorption, providing a high excitation enhancement. Alternatively the antenna

resonance can be matched with emission spectrum, in order to efficiently control emission properties. Furthermore, studying the size and shape of the hotspots of the nanoantenna provides a valuable insight on the optical resolution of the probe. In the following part of the chapter I will describe our strategies in order to engineer the nanoantenna probe, first tailoring its optical properties in excitation and then in emission.

Finite-difference time-domain (FDTD) calculations

In order to engineer the near-field nanoantenna probes we perform calculations of the electric field patterns generated by the nanoantenna by means of finite-difference time-domain (FDTD) method, using a FDTD tool, Lumerical. The first step of the method is to generate a 3D model that physically describes the system, namely the antenna probe and the SPE sample, as depicted in Figure 2.2a. The probe is modeled as a single metallic nanorod that can be oriented flat or partially tilted with respect to the horizontal plane. The substrate, a transparent medium containing SPEs, is modeled as a thick piece of glass. The lateral size of the nanoantenna is set to 50 nm, while changing its length it is possible to tune its resonance along the visible and near-infrared spectrum. The nanoantenna is connected to a glass socket, with a height of a few hundreds of nanometers. Between the socket and the nanoantenna is located a 3 nm titanium adhesion layer. The nanoantenna is located at 10 nm distance from the sample surface. Depending on the specific case, we place thin layers of additional materials on the substrate. In the computation volume a 3D grating is defined, technically called ¨mesh¨. The light source has to be modeled in order to accurately describe the laser beam, for such purpose we inject light in the simulation as a plane wave. The incident polarization can be set as linear or circular, depending on the specific experimental requirement. The source injects a pulse of light in the simulation volume

that is propagated solving Maxwell equations at the nodes of the mesh. The amplitude of the sources is normalized in order to get a unitary total electric field intensity in absence of the probe, in close proximity of the surface and inside the material where the emitter is located. In order to study the electric field patterns around the emitter, we record the light by placing field monitors. We use horizontal monitors, located 15 nm below the probe, as depicted in blue in Figure 2.2a, and vertical monitors cutting through the probe and sample. The monitors record both the intensity of the illumination beam and the light scattered by the nanoantenna, providing full information on the interference happening between the two. In order to get the best compromise between accuracy and computational efficiency we optimize the following items. The optical properties of every single component are described by their materials refractive indices, therefore it is essential that they are properly introduced in the simulations, for all the wavelengths. The step size and position of the mesh is a key parameter since it defines the precision and the time required for the calculation. The step has to be fine enough especially where small components are located and it has to ensure a minimum number of computational steps between sources and monitors (> 10), in order to avoid problems of solution convergence. Also, the mesh step size where the monitors are located is critical since it defines the resolution of the field maps. All the FDTD calculations have been performed by the author of the thesis.

Dipolar nanoantenna excitation resonance

In Figure 2.2b is shown a typical vertical monitor with the total field intensity plotted in log10 scale for the sake of clarity. The illumination light has linear polarization along the X axis.

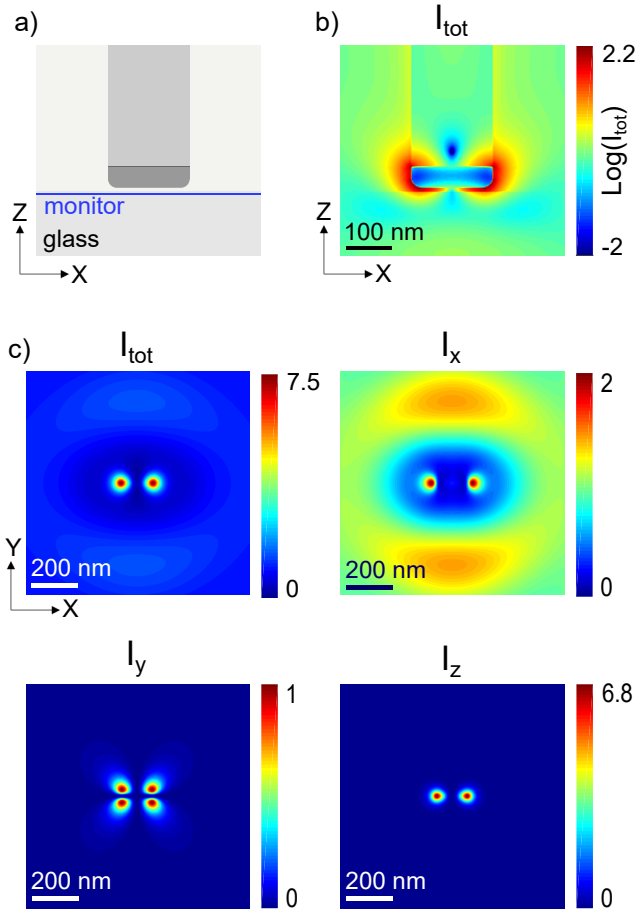

Figure 2.2: FDTD calculated near-field maps in close proximity to a dipolar nanoantenna probe. (a) sketch of a flat dipolar nanoantenna near-field probe with a lateral size of 50 nm and a length of 180 nm. The nanoantenna is located at 10 nm form the glass. (b) Simulated total field intensity map of the probe presented in (a). The field is strongly localized at the edges of the nanoantenna, providing two bright hotspots. (c) Simulated fields intensity horizontal maps, located 15 nm below the probe. Since the nanoantenna is excited with linear polarization in X direction at a wavelength of 670 nm, the Y and Z components of the electric field only show the scattering of the probe, while the X and the total fields also show the interference with the incoming beam.

The map shows the high level of field enhancement, that can be two orders of magnitude higher than the excitation beam on the nanoantenna surface, localized at the edges of the nanoantenna at the so called hotspots. The intensity maps presented in Figure 2.2c are horizontal monitors located below the nanoantenna, showing the intensity patterns for total and single components of the fields. The total field and the X component intensities show two bright spots in the center of a dark area, and an external bright ring. The Y and Z components of the field intensities show the typical four and two lobes pattern of a dipolar emitter. The horizontal monitors show that a dipolar nanoantenna probe can provide an excitation enhancement close to 10x for in-plane oriented emitters and allow the detection of out-of-plane molecules that would not be excited in a far-field measurement. Figure 2.2c shows clearly that, depending on the incoming beam polarization, the near-field intensity maps can exhibit interference (I_{tot} and I_X) or not (I_Y and I_Z). The components affected by interference also show a non-zero background due to the presence of illumination light. Since in these maps the incoming beam is X oriented this is the only single component of the electric field that is affected by interference.

Depending on nanoantenna metal, we now study the dependence of the resonance of the probe with respect to its length and metal, as reported in Figure 2.3a. The graph shows that, for each metal, the resonance of the nanoantennas red-shifts with the increase of the length. Even though nanoantennas of different materials and same length support resonances in different areas of the spectrum, the amount of red-shift due to length increase is similar for aluminum, gold and silver. Figure 2.3a shows that both the full visible and the near-infrared ranges can be covered tuning the nanoantenna length.

In Figure 2.3b are shown total intensity enhancements calculated for different antenna lengths, in each case for respective resonance wavelength. Such enhancements are relative to the hotspots

positions calculated 15 nm below the nanoantenna, inside glass substrate. For the sake of clarity the different cases have been studied for the same vertical distance. The red, blue and green rectangles in Figure 2.3b represent the areas that correspond to resonances in wavelength range between 600 nm and 800 nm. The graph shows how enhancement depends on antenna length, since nanoantennas absorption cross section also increase with their lateral size. Furthermore, for a given length, enhancement also depends on the material of nanoantenna. Nevertheless, the colored rectangles show how in the visible regime gold, silver and aluminum provide similar enhancements. Given the fast decay of the near-field intensity, operating the antenna at lower vertical distance provides higher excitation enhancements. Despite the different skin-depths of gold, silver and aluminum, that in the visible are respectively of $\sim$30, 25 and 13 nm [65], even for minimal vertical distances under antenna ($<$5 nm) in our configuration we don't find relevant different levels of light confinement due to the use of different metals among aluminum, silver and gold. Such result is due to the fact that our nanoantennas as thicker than the skin-depth of the three studied metals. Additionally, compared to gold and silver, that are relatively soft (gold) or oxidize easily (silver), aluminum is mechanically robust and only gets oxidized at level of external layers (few nanometers) [66].

The sketches in Figure 2.3c represent two cases of 25 and 10 nm radii of curvature for the lower nanoantenna edges. Such a small variation on the shape doesn't really affect the resonance of the probe, but has an effect on the local field enhancement. Figure 2.3d shows the dependence of the total intensity enhancement, for different aluminum nanoantenna lengths for the two cases presented in Figure 2.3c. Enhancements have been calculated with nanoantennas in contact with glass substrate and at a vertical distance of 4 nm below nanoantenna, where for both radii of curvature intensity reaches a value of 1/e with respect to metal. It reports on

the fact that the sharpness of the antenna edges has an effect on the excitation enhancement and that antennas with a 10 nm radius of curvature provide higher enhancement that antennas with 25 nm radius of curvature.

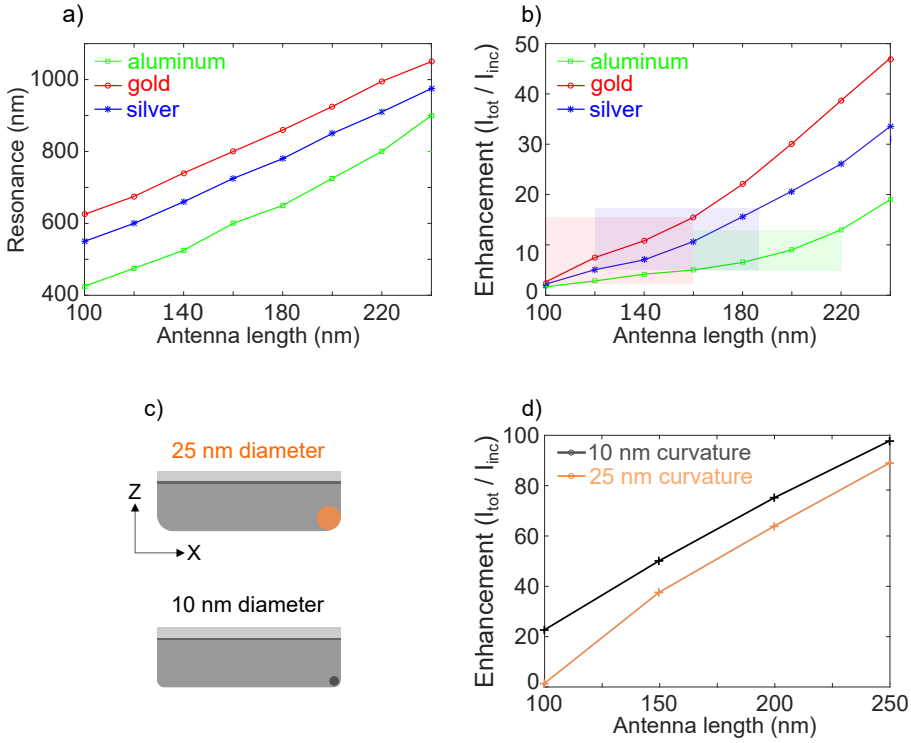

Figure 2.3: FDTD calculated excitation optical properties of dipolar nanoantenna probes. (a) Dipolar resonance dependence of the probe with respect to the antenna length, for aluminum, gold and silver. The studied range of lengths covers the full visible spectrum. (b) Total near-field intensity enhancement calculated 15 nm below the nanoantenna in glass for different materials for each case at its resonant wavelength. The colored rectangles correspond to a resonance wavelength range of 600-800 nm. (c) Sketches of probes with different radii of curvature of the lowest edges, of 25 and 10 nm. (d) Total near-field intensity enhancement calculated 4 nm below the probe for different nanoantenna lengths. Nanoantennas are in contact with glass substrate. The enhancements are relative to respective resonance wavelengths.

Dipolar nanoantenna emission resonance

Besides excitation enhancement also the emission properties of SPE are affected by nanoantennas. Here using FDTD simulations we investigate the effect of our probe on the emission properties of SPEs, calculating their normalized fluorescence lifetime change depending on the coupling with nanoantenna, hence the change of normalized total rate, with its radiative and non-radiative contributions. A sketch of the typical FDTD emission configuration is presented in Figure 2.4. The emitter is modeled as a dipole assuming an internal quantum efficiency $QE_{int} = 1$. In this case the only source in the simulation is the emitter itself. The emitter be oriented in X, Y, or Z direction, or it can be considered as an approximately isotropic emitter. While the single direction emitters can be used to represent single molecules, the isotropic one represents emitters constituted by many emitters closely packed, as molecular beads or densely packed atomic defects in 2D materials. The exact representation of an isotropic emitter requires the use of a big number of differently oriented emitters, with random relative phases. This goes beyond our computational capabilities, therefore we provide an approximated isotropic emitter representation given by the combined use of three perpendicular emitters located in the same point. Placing the emitter in different positions with respect to the nanoantenna, it is possible to obtain the lifetime at each point normalized to the lifetime of the uncoupled case which is considered as unity, providing normalized lifetime profiles. When we measure the lifetime of the uncoupled emitter we provide lifetime profiles multiplying the uncoupled emitter lifetime by our normalized lifetime profiles(see chapter 4).

For the normalized lifetime profiles the total power radiated by the emitter alone, measured by the black cubic box in Figure 2.4a), and the one of the emitter located in every specific configuration with respect to the nanoantenna, measured by the black cubic box

in Figure 2.4b), are compared. The ratio between the two powers is the normalized lifetime at each nanoantenna-emitter position. We can simulate the normalized radiative and non-radiative rates as well in a similar way, taking into account that the light absorbed by the metallic nanoantenna constitutes the non-radiative rate, while the light radiated in the far-field represents the radiative one. Figure 2.4b) shows that in our FDTD calculations the normalized radiative rate η_{rad} is measured by the red cubic box that contains emitter and nanoantenna, while the normalized non-radiative rate is obtained as follows $\eta_{\text{non-rad}} = \eta_{\text{total}}$- η_{rad}, where the normalized total rate η_{total} is calculated considering the light propagating through the small black cubic box that contains only the emitter. The QEs values are obtained according to following relation QE = η_{rad} / (η_{rad}+$\eta_{\text{non-rad}}$).

In Figure 2.4c) are reported the normalized total, radiative, non-radiative rates and lifetime respectively in black, red, blue and green of a dipolar emitter in close proximity to a dipolar nanoantenna. The emitter is located 15 nm under antenna, in a thin layer of hBN and it is oriented parallel to antenna. The antenna is 160 nm long and the calculation has been carried out for a wavelength of 650 nm. The graph shows how a resonant dipolar antenna can modify both radiative and non-radiative rate of a SPE. In the specific case both rates are increased, especially in correspondence of antenna hotspots. Since the total rate is increased in hotpots positions, in such positions the model also shows a strong decrease of emission lifetime. In the next chapters we will typically present the calculated normalized rates and the calculated change of lifetime expressed in nanoseconds, obtained multiplying the calculated normalized lifetime by the measured lifetime of the uncoupled emitter.

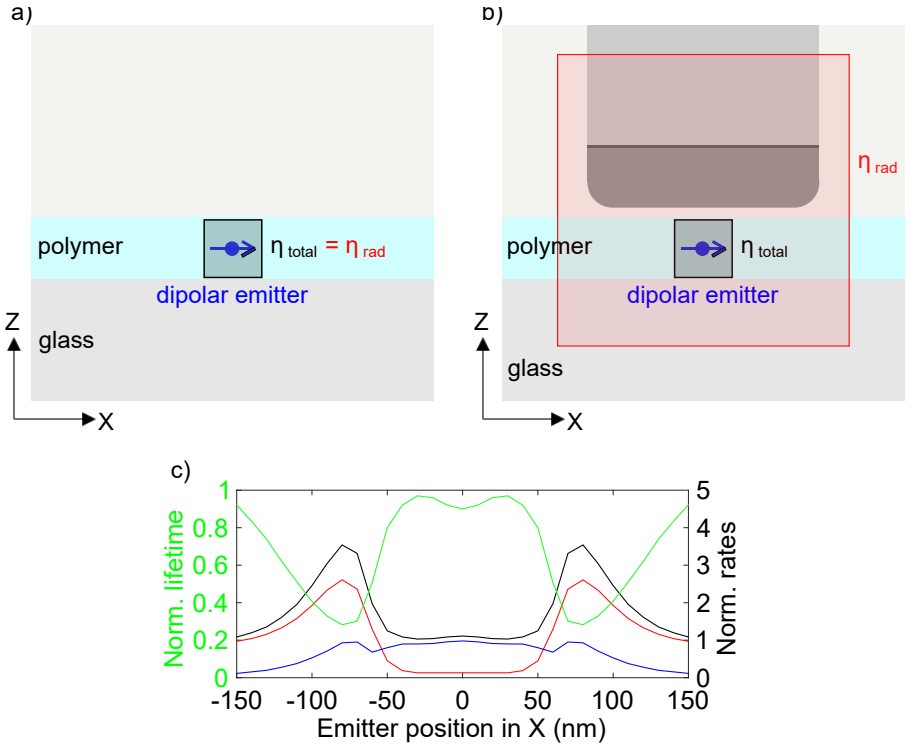

Figure 2.4: FDTD calculation configurations of nanoantenna probes emission properties. (a) Sketch of a dipolar emitter embedded in a thin (∼40 nm) transparent polymer layer, located on a glass substrate. The black cubic box measures the total and the radiative rates of emission $\eta_{\text{total}} = \eta_{\text{rad}}$. (b) Sketch of the same configuration in (a) with the additional presence of a nanoantenna probe in close proximity (∼10 nm) to polymer surface. In this case the black cubic box measures η_{total}, while the red one measures η_{rad}. (c) Simulated normalized total (black) rate, radiative (red) and non-radiative (blue) rates and normalized emitter lifetime (green). The emission wavelength is at 650 nm, the emitter is oriented parallel to antenna, located 15 nm under it inside a transparent polymer thin layer. Emitter has unity internal quantum efficiency, antenna is long 160 nm.

The mentioned FDTD calculations provide a full characterization of a dipolar near-field probe, taking into account its excitation and emission effects on SPEs optical properties.

2.3 Fabrication of near-field probes

Once that the dipolar probe has been fully engineered, the next step is its realization. This step involves advanced nanofabrication techniques in order to sculpt a 3D nanostructure, on the apex of an optical fiber, with full control on shape, size and orientation in the space. For this purpose we start with a piece of optical fiber with a diameter of ∼100 µm that will act as the final support of the near-field probe, and we heat-pull it using a micropipette puller (Sutter P2000). This way we obtain a tapered end piece of optical fiber with a diameter <100 nm, as shown in Figure 2.5a.

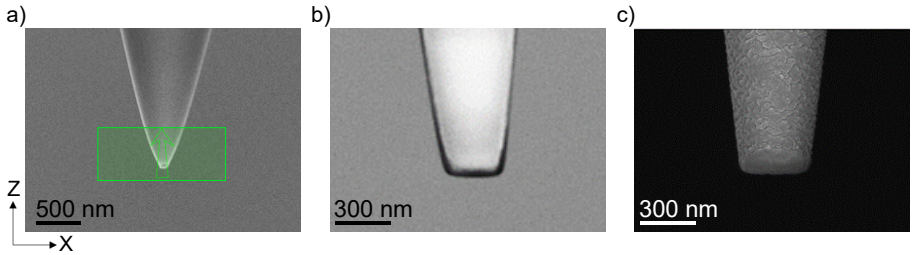

Figure 2.5: SEM images of the three initial phases of probe fabrication. (a) A tapered end optical fiber obtained by heat-pulling, with a typical diameter < 100 nm. (b) The optical fiber is cut flat at the end with Ga FIB, the typical dimeter is now ∼ 400 nm. (c) A 3 nm titanium adhesion layer and a 50 nm aluminum layer are deposited by thermal evaporation, to act as a robust base for the nanoantenna fabrication.

At this point, since we need to mill material with a precision of a few nanometers, we use the gallium focused ion beam technology (FIB) to cut flat the heat-pulled optical fiber at the end, etching its last part, as represented in Figure 2.5a by the green rectangle. The green arrow represents the milling direction. This operation provides a flat base of a diameter of ∼300-400 nm, shown in Figure 2.5b. On this flat-cut fiber we deposit first 3 nm of titanium

adhesion layer and then 50 nm of aluminum by thermal evaporation, the result is shown in Figure 2.5c.

We employ two different FIB systems, the Zeiss-Auriga crossbeam, that is equipped with Gallium (Ga) FIB for the fabrication and an electron-beam for the imaging of the structures, and the Zeiss-Orion nanofab, that is equipped with a helium (He) and a neon (Ne) FIB system. Both the systems use a tightly focused beam of ions, highly accelerated, to etch material with high precision. Nevertheless, gallium and helium FIBs present some important differences. The first one has a beam of a minimum size of 7 nm and a high etching rate that allows the fabrication of 3D structures with a precision of $\sim$10 nm. For the fabrication of structures of a size $<$ 100 nm, the etching process is so fast that the control is limited.

On the other hand, the He FIB technology is based on a more focused beam, of a size of nominally 0.5 nm and since the helium ions are much lighter than the gallium ones, its etching rate is also lower [67]. This results in a higher precision in the fabrication, with a control on 3D structures fabrication of $\sim$5 nm and in a higher control during the process, since the helium etching results in a slower and more precise material removal. The main limit of the helium FIB technology is that, due to its low etching rate, the fabrication of structures larger than a few hundred of nanometer takes huge amounts of time, making the all fabrication process particularly exposed to drift problems. The best condition is then given by a combination of Ga and He FIBs where the first one is used in order to provide the milling of the biggest parts, while the second is used for the finest details. In both cases, the ions are accelerated with high voltages (30keV), and the size of the beam is controlled through the current of the beam ($\sim$2-4 pA). At this stage it is possible to use both the FIBs for the next nanofabrication steps. Figure 2.6a shows a Ga FIB top view image of a flat-cut fiber coated with aluminum, already shown from the side in Figure 2.5c.

The four green rectangles represent again the milling areas, with their milling directions, that are always inwards, in order to have the milled material deposited outward. The detailed design and control of such milling profiles is obtained with the NPVE software provided by Zeiss. Each rectangle is milled with a current of 2 pA, single repetition scan, a dose = 0.1 $nC/\mu m^2$ and a dwell time = 700 µs. The Ga FIB imaging is particularly dangerous for the probe, since it can etch tens of nanometers of metal in a few seconds. Figure 2.6b and c are SEM images taken respectively from top and from side of a flat dipolar nanoantenna probe, with a lateral size of 50 nm and a length of 180 nm. Its resonance is around 650 nm wavelength. The nanoantenna is sitting on a glass socket of a few hundreds of nanometers high. The typical radius of curvature of the lower edge of such a probe is of ∼25 nm.

Starting from the last step of fabrication reported in Figure 2.5 c, it is also possible to proceed using the He FIB technology, as reported in Figure 2.7. Figure 2.7a is a top view He FIB image of a fiber at the stage of fabrication presented in Figure 2.5c.

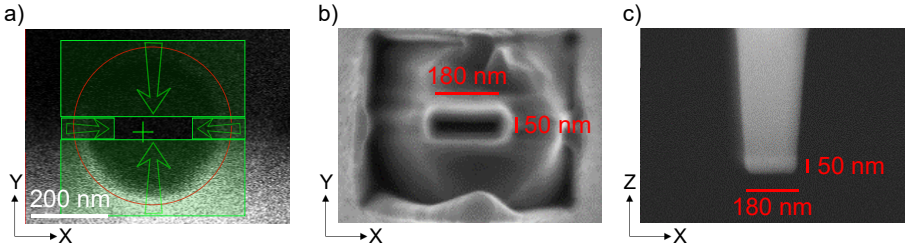

Figure 2.6: Milling techniques for the nanoantenna probe fabrication by gallium FIB. (a) Ga FIB top view of an aluminum coated fiber similar to the one reported in Figure 2.5c, the green rectangles represent the milled areas, the arrows the milling directions. (b) SEM top view of a fabricated dipolar nanoantenna probe with a lateral size of 50 nm and a length of 180 nm. (c) SEM lateral view of the nanoantenna presented in (b), it is supported by a glass socket of a few hundreds of nanometers length.

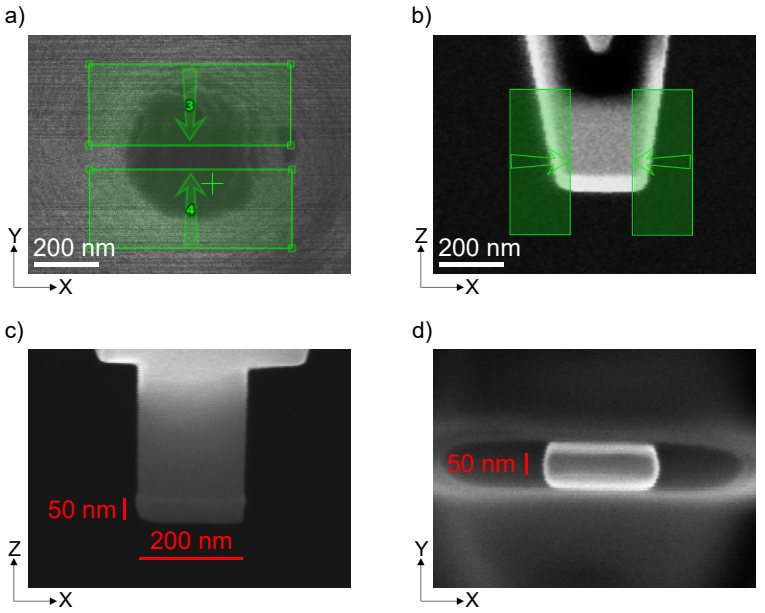

Figure 2.7: Milling techniques for the nanoantenna probe fabrication by helium FIB. (a) He FIB top view of an aluminum coated fiber, similar to the one reported in Figure 2.5c. The green rectangles with the arrows represent respectively the areas milled by He FIB from top and the milling directions. (b) He FIB lateral view of an aluminum coated fiber after the step reported in (a). The bright external layer of the fiber is an aluminum layer with a lateral size of 50 nm. The two green rectangles represent the areas milled in order to get the final dipolar nanoantenna probe. (c) SEM lateral view of the fabricated nanoantenna, with a length of 200 nm and a lateral size of 50 nm. (d) SEM image, top view of the probe.

The etching of the two green rectangular shapes depicted in Figure 2.7a, determines the formation of a thin slice of material (∼50 nm), as shown in Figure 2.7b, another He FIB image side view. At this point, the last lateral cut depicted in Figure 2.7b generates the nanoantenna probe, setting its length and defining its dipolar resonance in the spectrum. Figure 2.7c and d are SEM side and top images, showing a stand-alone nanoantenna probe with a lateral size of 50 nm and a length of 200 nm. Its resonance is at

∼700 nm wavelength. The typical radius of curvature of the lower edge of such a probe is of ∼10 nm, providing a slightly higher excitation enhancement, as discussed previously in section 2.2. Since the upper part of the coated fiber shown in Figure 2.7a is only ∼400 nm wide, the typical milling time with the He FIB is below one minute, hence the fabrication is not limited by significant drift problems. At the same time, the low etching rate of the He FIB allows to image multiple times the structures and mill them with unprecedented precision and control. All the nanoantenna probes have been fabricated by the author of the thesis.

2.4 Fabrication of single emitter samples

For the study of the interaction between single nanoantennas and SPEs, we use different types of emitter systems. We focus on molecular systems and atomic defects in ultra-thin so called 2D materials. In both cases, the sample thickness is a key parameter, since the typical depth of the probe evanescent near-field is of ∼25 nm in the vertical direction.

Terrylene diimide (TDI) molecules. We used TDI molecules because of their high internal QE and photostability [68]. In this case we spin-coated a solution of 10^{-8} M concentration of molecules in 1 % w/w of poly methyl methacrylate (PMMA) in toluene on a clean cover-slip, obtaining a thin transparent layer of ∼20 nm thickness. The absorption and emission peaks for the TDI molecules are around 650 and 680 nm respectively.

Dibenzoterrylene (DBT) molecules in anthracene. For the study of interference effect in nanoantenna-molecule interaction, we used dibenzoterrylene (DBT) molecules in anthracene (AC) [69]. In this configuration DBT molecules are exceptionally photostable and are only in-plane oriented, ideal case for experiments where the interference effect has to be addressed, since it doesn't affect purely vertically oriented molecules (chapter 5). The AC is dispersed in

diethyl ether with a concentration of 2.5 mg/ml and 10 µl/ml of benzene are added. The latter serves to improve the quality of the crystals obtained from the spin-coating process. The DBT is dispersed in toluene in a concentration of 10 µM and then diluted by a factor of 100 in the AC/diethyl ether mixture. The final solution is spin coated on a clean cover-slip providing a thin transparent layer of ∼40 nm. The absorption and emission peaks for the DBT molecules are around 750 and 790 nm respectively.

Polystyrene fluorescent nanobeads and LH2 nanospheres. For probe test measurements we used fluorescent nanobeads made of polysterene of a size of ∼20 nm, containing few hundreds of fluorophores (Invitrogen FluoSpheres 8783) and LH2 nanospheres of a size of ∼20 nm made of few tenths of LH2 complexes sinthetically arranged in spherical shape. Both the molecular systems are dispersed in aqueous ∼2% w/w polyvinyl alcohol (PVA) solutions at a concentration of 10^{-6} M and spin coated on a cleaned glass cover-slip in order to provide a thin transparent layer of ∼40 nm thickness. The absorption and emission peaks for the nanobeads are around 650 and 680 nm respectively, while for LH2 nanospheres they are at 850 and 870 nm.

Atomic defects in hBN. The hexagonal boron nitride (hBN) single atomic defects samples are obtained by scotch tape exfoliation of single flakes (thickness of ∼5-10 nm) on clean cover-slips. To increase the density of photostable defects into the hBN flakes, the samples are exposed to Oxygen and Argon plasma etching (with respectively 150 and 80 W power for 2 minutes) [70]. The samples are then thermally treated for 30 minutes at 850 °C in Argon atmosphere to stabilize the emitters [45, 71]. In the case of the hBN atomic defects, they can be efficiently excited at 520 and 620 nm wavelength and their emission ranges from 550 to 750 nm depending on the single emitter [72].

For the molecular samples we use standard coverslips of 170 µm thickness, while for the hBN defects samples we use quarts cover-

slips of the same thickness, because of the lower optical background (a factor of ∼10x lower). Such optical background in standard glass coverslips can be related to the presence of impurities that emit light when illuminated by laser light [73]. All the coverslips are cleaned with sonication in acetone, water and methanol and exposed to UV. All the molecular solutions are spin-coated at a speed of 6000 rounds/min for 60 seconds, except for the DBT solution that is spin-coated at different speeds from 2000 to 7000 rounds/min, depending on the thickness required for the specific experiments. The TDI, LH2 and nanobeads samples have been fabricated by the author of the thesis, while the hBN and DBT ones have been provided by respectively the groups of Efetov and Toninelli.

2.5 Experimental Techniques

Since the nanoantenna hotspot has a lateral size of a few tenths of nanometers (∼40 nm), the controlled coupling with SPEs requires few nm control especially for distance dependence, while the emitter is excited and its emission collected. Here we use a home-built near-field scanning optical microscope (NSOM) in order to control independently nanoantenna and emitter. The scheme of the experimental setup is reported in Figure 2.8. For the excitation of the system we use a supercontinuum white light pulsed laser (SuperK Extreme, NKT Photonics). Such system provides light with a wide range of wavelengths (400-850 nm), its versatility allows the study of emitters that absorb at visible and near-infrared wavelength. The laser light is collimated and spectrally filtered with the use of narrow bandpass filters. The polarization of the laser light is controlled with a linear polarizer. The light is coupled into a confocal microscope (Axiovert 135 TV, Zeiss) through a beam splitter (90:10) and focused through an oil immersion objective with high numerical aperture (NA=1.3). The sample is positioned on a 3D piezo driven stage (Nano-PDQ 350, MCL Inc.). The light emitted is

collected by the same objective and spectrally separated from the illumination beam by means of long pass optical filters. With the use of a flipping mirror, the emission light can be sent to two avalanche photo diodes (APDs, PDM series 50 µm, Micro Photon Devices) or to an home built spectrometer through an optical fiber. For the dispersion of the light in the spectrometer we use a prism, for its collection an electron-multiplying charge-coupled device (EM-CCD, ImagEM X2 EM-CCD C9100-23B, Hamamatsu). The spectrometer allows the measurement of point spectra and spectral images, since it is synchronized with the scanning systems. For lifetime measurements the two APDs are connected through a router (PHR 800, PicoQuant) to a time-correlated single-photon counting module (TCSPC, PicoHarp 300, PicoQuant). In this configuration the router has the purpose of integrating the signals of the two APDs. The laser is also connected to the TCSCP module for laser pulse synchronization. For antibunching measurements the APDs are directly connected to the TCSPC module. Sending the light to the APDs through a 50:50 beam splitter we obtain obtain fluorescence images, lifetime images and antibunching point measurements.

The near-field module of the NSOM is represented in Figure 2.8 upper part and it is constituted by the following elements. The most delicate part is the near-field nanoantenna probe, fabricated at the apex of a piece of optical fiber and glued on a quartz tuning fork. The tuning fork is controlled through a 3D piezo stage that is controlled by the shear-force feedback system. The feedback is based on custom-built electronics that detect the phase between the driving signal, oscillated by means of a piezo with a voltage of 50 mV, and the phase response of the tuning fork itself. Any interaction between the tip and the surface results in a change of phase that is used by the feedback loop in order to keep the nanoantenna-surface z distance constant with $<$ nanometer accuracy. Such shear-force feedback mechanism does not provide a direct measurement of the

absolute nanoantenna-surface z distance. However, based on various near-field measurements and z-scans we estimated such distance to be of approximately 10 nm. The force feedback system automatically provides topographical images of the surface, with a resolution in z direction of 1 nm. Having the sample and the probe mounted on two different piezo stages provides five independent axes, hence the possibility to scan the sample or the probe with respect to the optical axis of the microscope, as shown in the sketches (a) and (b) of Figure 2.9. In the first case presented in Figure 2.9a, the sample scan configuration, the nanoantenna is positioned on top of the diffraction limited spot, hence it is continuously illuminated. While the nanoantenna is kept stationary on top of the illumination spot the sample is scanned, providing super resolution images of SPEs. In the second case, sketched in Figure 2.9b, it is shown the probe scan modality. In this configuration the emitter is kept stationary at the center of the diffraction limited spot, continuously illuminated, and the nanoantenna is raster scanned on the emitter. This configuration allows the mode mapping of the nanoantenna using a SPE and provides information on the optical properties of the coupled system.

Such experimental setup represents an ideal instrument for deterministic control and manipulation of SPEs by means of nanoantennas.

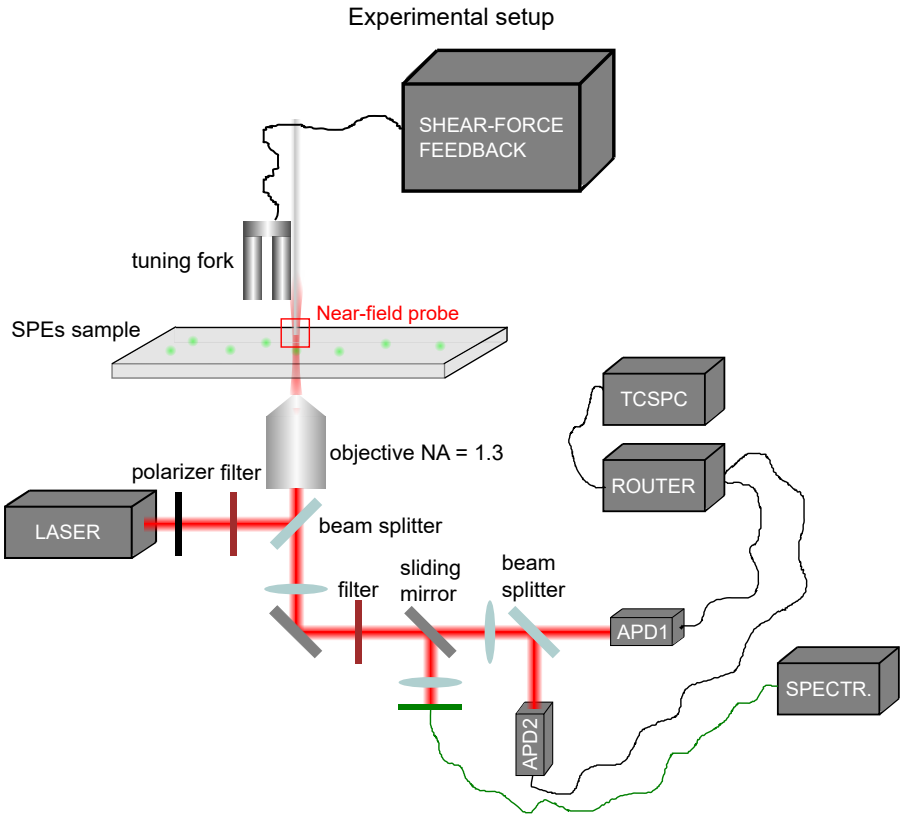

Figure 2.8: Scheme of the experimental setup. A super continuum laser beam is focused down to the diffraction limit on a sample with a thin layer (∼40 nm) of SPEs with an oil immersion objective with numerical aperture NA=1.3. On the sample surface, a dipolar nanoantenna probe located at the apex of an optical fiber is scanned in X-Y direction, while the z distance (∼10 nm) is kept constant by means of a shear-force feedback loop. The fiber is glued on top of a quartz tuning fork resonator, the feedback loop is based on the phase signal between the driving signal and the response of the tuning fork, that is sensitive to the probe-surface interaction. The light is collected with the same objective and separated by the illumination with an optical filter. A sliding mirror is used in order to send the light to a spectrometer or to two APDs. In front of the APDs there is a 50-50 beam splitter. The APDs are connected to a time-correlated single photon counting system (TCSPC) for lifetime imaging and second order cross correlation measurements.

In the next two parts we show examples of near-field and time-resolved measurements.

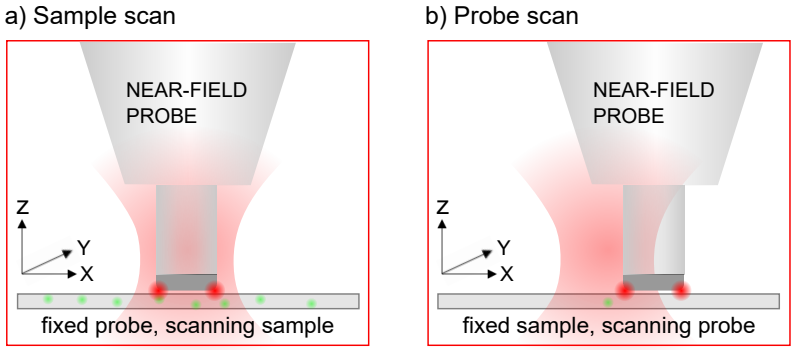

Figure 2.9: Schemes of the NSOM modes of operation. (a) and (b) are zooms of the near-field probe in two differerent operation modes. (a) Represents the sample scan mode, where the nanoantenna is kept stationary in the centre of the illumination spot and the sample is raster scanned, it provides near-field super resolution images. (b) Represents the probe scan mode, where the nanoantenna is raster scanned over a continuously illuminated SPE. It provides near-field images of the mode of the nanoantenna coupled to the emitter.

Optical near-field measurements

Our NSOM provides high resolution images of SPEs, enhancing their emission through excitation and emission processes [29]. The excitation enhancement is provided by the capability of the nanoantenna to focus the light down to sub-diffraction limited size hotspots. In order to efficiently excite the probe, the resonance of the nanoantenna has to be tuned with the maximum of absorption of the emitter and the excitation laser light. In emission they can enhance the brightness of the SPEs increasing their decay rates, especially if they have a low QE [32]. Figure 2.10 presents two near-field intensity maps of different molecular systems. Figure 2.10a is a near-field map of a sample of TDI single molecules, obtained with an excitation at 630 nm wavelenght and a dipolar nanoantenna probe of

a length of 180 nm. The image shows two sharp spots located at the edge of the nanoantenna, of a lateral size of ∼40 nm per emitter, superimposed to a confocal diffraction limited spot of ∼300 nm. The intensity enhancement provided by the probe depends on the emitter orientation. Since the near-field of the nanoantenna is nanostructured, it provides vectorial components of the electric field along the three directions of space. This allows the detection of molecules Z oriented, that would not be excited confocally, enhancing the sensitivity of the confocal microscope. While for the in-plane oriented molecules the maximum enhancement is of ∼10x compared to far-field confocal microscopy, for the Z oriented molecules the enhancement can reach much higher values, since they are simply not excited by a classical in-plane oriented excitation field. While the in-plane oriented molecules present a background due to confocal illumination, the purely Z oriented emitters only show the two near-field high resolution spots.

Figure 2.10b is a near-field intensity map of a different molecular system, constituted by LH2 nanospheres of a size of ∼30 nm, as presented by the SEM image in the inset, located in a thin transparent polymeric film. For the illumination is used a light of 800 nm wavelength, hence a resonant dipolar nanoantenna of 220 nm length. Those systems also provide a confocal spot with superimposed two sharp near-field enhanced spots (∼50 nm). In this case, since every nanosphere is made of many emitter, they behave like isotropic absorbers and emitters. For this reason the confocal background is always present, while the near-field effect of the probe can be more or less pronounced depending on the nanoantenna-emitter distance. The best fluorescence enhancement is in this case of ∼3x. The examples reported in Figure 2.10 show the capability of the experimental setup to provide enhanced high resolution images of SPEs.

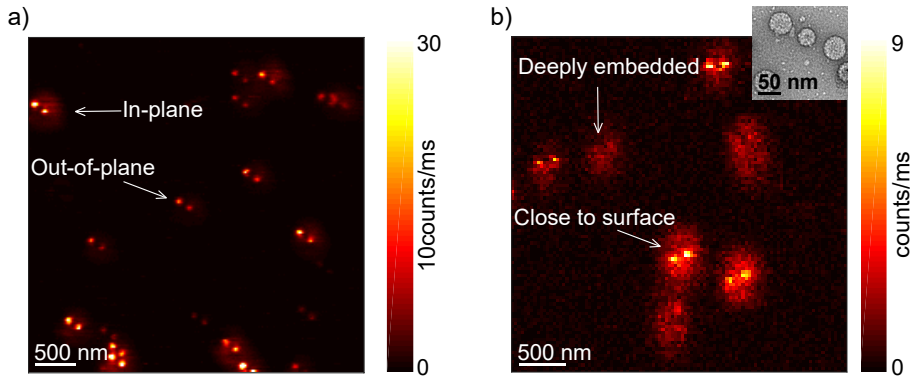

Figure 2.10: Nanoimaging of single-photon emitters by means of a dipolar nanoantenna probe. (a) Near-field scan of a single-molecule (TDI) sample, using a nanoantenna probe. Every molecule shows the typical two hotspots pattern. While the totally out-of-plane emitters only show two bright spots, the in-plane ones also show the confocal one. The optical resolution is of 40 nm, the excitation wavelength of 630 nm. (b) Near-field scan of an LH2 nanospheres (∼30 nm) sample, top-left inset is an SEM of the nanospheres. The nanospheres are made of many emitters, hence they result in isotropic systems. Superimposed to the two typical near-field spots is always visible the confocal one. Only the nanospheres that are close enough to the surface interact with the nanoantenna, thus the two enhanced hotspots are not always present. The optical resolution is of 50 nm, the excitation wavelength of 800 nm.

Time-resolved measurements

The typical lifetime of a SPE is in the order of 10^{-9} - 10^{-8} seconds and it is a probabilistic concept referred to the characteristical decay time of an emitter from the first excited state to the ground one. SPEs are generally defined as two level systems capable of emitting a single photon at a time (antibunching), instead of emitting multiple photons together (bunching). These two properties, namely the lifetime and the photon statistics are key elements for the characterization of SPEs [31].

We can operate our experimental setup in two different configurations, in the first one we can perform time-resolved measurements (lifetime measurements), in the second one we can characterize the emitter photon statistics (antibunching measurements). The instrument response function (IRF) of our system is limited by our APDs (PDM series 50 µm, Micro Photon Devices) time resolution, that is wavelength dependent and spans from ∼45 ps at 800 nm to ∼250 ps at 400 nm.

In the time-resolved measurements configuration, we can measure the arrival time of every photon (stop signal), with respect to the excitation pulse (synchronization signal), using a TCSPC system [74]. In Figure 2.11 are reported the IRF of the instrument at 620 nm wavelength (black), the photons histogram of an hBN defect uncoupled (green) and coupled (red) to a nanoantenna probe. The blue lines represent single exponential fits of the data, after time-gating the photons at >2 ns. In this case, the lifetime of the emitter has been shortened of a factor of ∼2.2x. Synchronizing the piezo scanner with the TCSCP system it is possible to obtain maps where the photons histogram is recorded at each pixel. Fitting the photons histograms at each pixel it is possible to obtain a lifetime map, as depicted in the inset sketch in Figure 2.11. We also perform point-measurements where we collect the photons histogram locally and then obtain the lifetime fitting the photons distribution. The time-tagged photon detection allows us to time-gate the photons, integrating the signal in a specific time interval, as represented by the yellow area in Figure 2.11. With this strategy we can reject the first ∼2 ns of photons detected, where all the nanoantenna luminescence is located in the time domain. This is particularly useful for separating the nanoantenna luminescence from the emitter contribution. We use time-gating for the cases where the emitter has a relatively low absorption cross section (single atomic defects, see chapter 4) or its emission is depleted (see chapter 5).

In the emitter photon statistics configuration, we use a Hanbury-Brown-Twiss setup to determine the second-order photon autocorrelation. We connect the two APDs directly to the TCSPC module and use it in histogramming mode in order to get the number of coincidences between the detectors, performing antibunching measurements. In this case one APD provides the start and the other the stop signal.

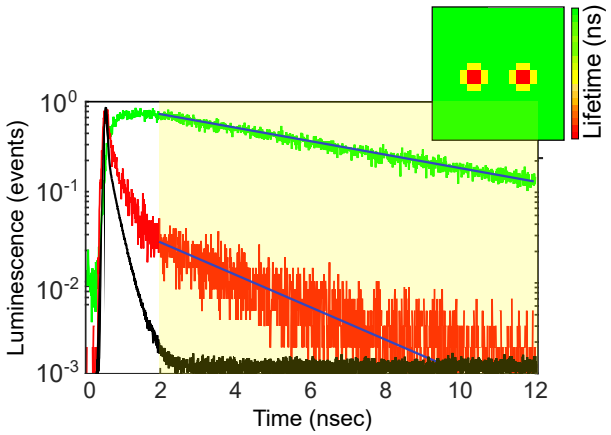

Figure 2.11: Near-field lifetime imaging. Photons histograms extracted from a typical near-field lifetime image. The black plot is the instrument response function (IRF), that is of 45 psec. The green and red plots represent the photons histograms of respectively an uncoupled and coupled hexagonal boron nitride SPE to the nanoantenna probe. The yellow area represents the time domain considered for the linear fit (photon time-gating), with the rejection of the photons emitted in the first 2 ns from the excitation laser pulse. The coupling with the nanoantenna results a lifetime shortening. The lifetime can be mapped scanning an area, providing a lifetime image, as sketched in the sketch at up-right corner.

The start stop measurement is accurate for emitters that have a lifetime that is short compared to the time between subsequent laser pulses (∼12 ns). Additionally it is important that the laser pulse duration (∼40 ps) is short enough in order not to have repump of the emitter during a single laser pulse. With a cross-

correlation analysis of the data we can retrieve the second-order cross-correlation function, that gives a quantitative information of the SPE purity of emission, in this framework the capability to emit only one photon at a time.

2.6 Conclusion

In this chapter the main technical aspects of the thesis have been discussed, starting with a detailed review of the antenna-emitter state-of-the-art coupling strategies and describing the computational and experimental techniques that have been adopted. In the following chapters are described the applications of such strategies to the development of original high resolution near-field probes, the study of novel SPEs and the implementation of novel high resolution imaging approaches based on controlled local field depletion.

Chapter 3

Tilted dipolar antenna probes for high resolution imaging

In this chapter are discussed the achievements in the implementation of the novel concept of tilted dipolar antenna probes for high resolution NSOM applications. The goal is to overcome the limit of state-of-the-art high resolution imaging of flat dipolar antenna probes. Two different types of tilted probes are described, discussing their implementation, the design, the nanofabrication and the optical test with molecular beads. First It is shown that a 30° tilted dipolar antenna (TDA) preserves its resonance, while it provides a single sub-wavelength hotspot interacting with the emitters instead of two. The TDA probes provide better topography maps than the state-of-the-art flat dipolar antennas. As second development it is presented the case of a 30° tilted antenna with a special metal-glass interface at the apex (MGTDA), that provides additional light confinement due to refractive index discontinuity. The conclusion is that the optical resolutions of the two types of probes are comparable and both provide a single hotspot per excitation point.

Manuscript in preparation.

3.1 Introduction

In the last decades near-field scanning optical microscopy (NSOM) has been successfully employed as advanced experimental technique for the manipulation and imaging of SPEs [42, 75, 76]. Using nanoantennas as near-field probes [29], or attaching a SPE at the probe apex [77], relevant work has been presented, controlling the optical properties of SPEs and localizing them with a precision 10-20x better than the size of the optical wavelength. Nevertheless, among the two approaches, the incorporation of the emitter at the probe presents a weakness, since the SPE tends to bleach, hence has a limited photon budget that intrinsically limits the life of the probe [77, 78].

On the other hand, the fabrication of the probe as a metallic nanoantenna virtually provides a tool with unlimited life, mainly defined by its mechanical stability and the operation conditions [27, 29]. This approach can be differentiated into two types of implementation: illumination of the probe and of the emitter embedded in the sample is provided through the near-field tip itself [26] or from the far-field by the microscope objective [63]. Both the approaches present advantages and drawbacks. While the top illumination is a background free technique that provides high resolution imaging, it also suffers from very low throughput, due to very low light transmission in tapered fibers and subwavelength apertures [28, 79]. Conversely, the far-field illumination doesn't suffer from low throughput, since the illumination and collection are provided by the microscope objective. Indeed, the price to pay is given by the background due to diffraction limited size excitation beam, hence in this case the interference effect between incoming and scattered field has to be taken into account. Nevertheless, the strong field enhancement due to the light confinement in close proximity of the antenna ensures that the intensity of the light emitted at

the hotspots is considerably stronger than the background due to far-field illumination [29].

In far-field excited near-field microscopy, the illumination of the probe can be obtained with different polarization conditions of the excitation beams. Radial polarization, characterized by a strong z component of the electric field, is ideal for light confinement at the apexes of vertically oriented sharp tips [50, 63]. Unfortunately, the generation of radially polarized light is not straightforward as in-plane polarization with strong x-y component electric field. Furthermore, robust vertically oriented tips are typically non-resonant. Conversely, the use of dipolar probes doesn't require any specific illumination polarization, in fact they can be employed with normal in-plane polarization beams. At the state-of-the-art, relevant work has been produced using flat dipolar antennas as near-field probes, for high resolution and enhanced single molecule microscopy, as well as studying antennas as cavities coupled to SPEs [19, 29]. Unfortunately, the potential of these near-field probes is limited by the presence of the two bright hotspots. Indeed, they provide two strongly enhanced fluorescence spots per emitter, limiting the capability to discriminate single emitters, especially in highly densely packed systems [29]. At the same time, the relatively big ($\sim$100-200 nm) contact area of the flat probes limits the topographical resolution as well as the possibility to scan the tip very close to the sample surface, where the SPEs are embedded. Finally, a small antenna-emitter distance is particularly relevant for the exploration of novel physical regimes like strong coupling, where a total emitter-antenna distance $<$5 nm is required [19, 80].

In order to overcome these limitations, while keeping the resonant enhancement of antennas, we developed two types of tilted resonant probes. In the first case we tilted the well known flat dipolar antennas by a given angle (TDA), in the second case we exploited the sharp metal-glass transition at the interface (MGTDA) between the two materials in order to provide an additional light

confinement. For both the types of near-field probes, we initially engineered their optical properties, studying the optimal antenna tilt in order to obtain a resonant object providing a single hotspot per emitter. It turned out that, for antennas operating in the visible range, the optimal tilt is ∼30°. Next we developed a robust and reliable nanofabrication procedure for the realization of tilted antenna tips. Finally, we tested their optical properties, verifying their superior performances compared to the state-of-the-art flat dipole antenna probes.

3.2 Design and fabrication of TDA probes

The design of tilted dipole antenna probes requires the careful engineering of their optical properties. Figure 3.1a represents the concept of a tilted dipolar probe. Instead of scanning a flat antenna in close proximity to the sample surface, the aluminum antenna, of a lateral size of 50 nm and a length of 180 nm in this case, is tilted by a given angle with respect to the X direction. The shear-force feedback guarantees a constant z distance between the lowest part of the probe and the surface (section 2.5). Figure 3.1b shows a FDTD vertical map of the total field intensity across the probe, excited with linear polarization at 670 nm wavelength. The antenna can provide hundreds-times electric field enhancement, when excited resonantly. We define the enhancement Enh of the total field intensity as follows: $Enh = I_{\mathrm{tot}}/I_{\mathrm{inc}}$, where $\mathrm{I_{tot}}$ is the maximum intensity recorded at the hotspot and $\mathrm{I_{inc}}$ is the laser incoming intensity. Figure 3.1b also shows how the volume with main field enhancement (hotspots) are located at the two edges of the antenna, as in the case of a flat dipolar probe [29]. The main difference is given by the fact that now the hotspots are located at different Z heights. In fact, while the lowest edge of the antenna is scanned very close to the surface, the other one is at ∼80 nm z distance from it for an antenna of 180 nm length. Due to the fact that antenna near-field

decays exponentially in Z direction, a few tenths of nanometers below the metal there is effectively no field enhancement at the surface anymore. In other words, the tilt guarantees that only the lowest hotspot interacts with the emitters on the surface.

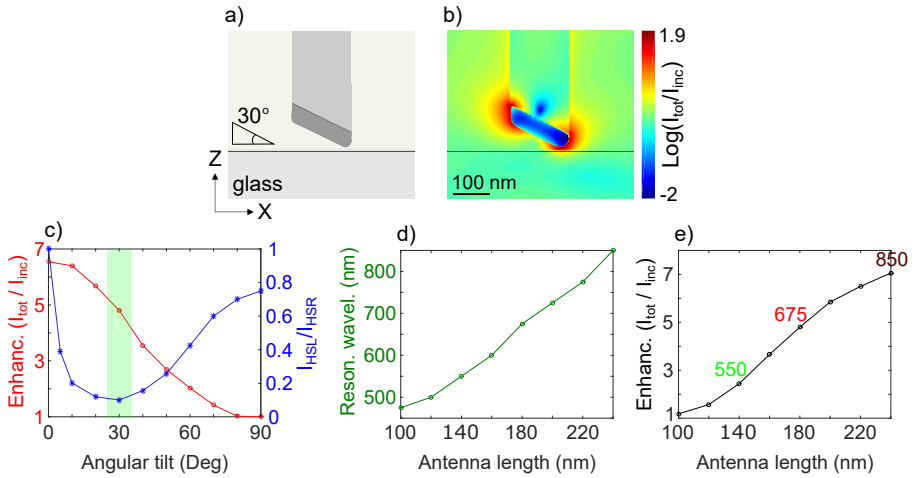

Figure 3.1: FDTD optical characterization of a 30° tilted dipolar nanoantenna probe. (a) sketch of a 30° tilted dipolar nanoantenna near-field probe with a lateral size of 50 nm and a length of 180 nm. (b) Calculated total field intensity map of the probe presented in (a), excited with linear polarization at 670 nm wavelength. (c) Dependence with respect to antenna angular tilt of the total field intensity enhancement calculated in the antenna hotspot 15 nm below the probe, and of the ratio between left hotspot (HSL) and right hotspot (HSR) intensities with respect to antenna angular tilt. (d,e) Dependences of respectively the resonance and the total field intensity enhancement with respect to antenna length. In e) are reported with the respective colors the resonance wavelengths for some specific antenna lengths to show that the enhancements correspond to different wavelengths.

On the other hand, tilting the antenna by 30° out of the horizontal plane, makes less efficient its excitation using an in-plane polarization beam. Figure 3.1c shows two significant antenna properties with respect to angular tilt. The first one is the enhancement (Enh, red) as previously defined, the second is the ratio between the left

(HSL) and right (HSR) hotspots intensities (blue), both quantities recorded by horizontal monitors located 15 nm below the antenna. According to the simulations, for a tilt <10° and >40° the ratio between the two hotspots intensities is comparable. For tilt values >30° the enhancement drops considerably due to low excitation efficiency and both HSL and HSR become negligible. Figure 3.1c shows that, for antennas operating at ∼670 nm and of a length of ∼180 nm the optimal tilt is of 30° (green area), since it provides still ∼75% of the flat probe enhancement, but only one hotspot interacting with emitters. Besides these properties, the tilted probe preserves the resonant behaviour typical of a flat dipolar antenna. Figure 3.1d shows how the 30° TDA probe has a dipolar resonance that red-shifts increasing its length, a probe of 180 nm length is resonant at 670 nm. Also Figure 3.1e shows how the enhancement increases in the visible and near-infrared regimes with the increase of antenna length, mainly because the absorption cross section of the probe increases. In Figure 3.1e the colored numbers indicate how the reported enhancements correspond to resonances at different colors (wavelength) of the light.

Even though conceptually the TDA probe only presents a slight change compared to the flat antenna tip, its realization requires the development of a novel, ad hoc nanofabrication procedure. The main core of the fabrication is based on the process already discussed in section 2.3, but in this case the additional degree of freedom of the 3D antenna orientation has to be controlled. In Figure 3.2 are described the nanofabrication steps involved in the realization of the tilted probes. The antenna support is obtained by heat-pulling of a piece of optical fiber, that has a typical size at the end of ∼100 nm, as depicted in the SEM image in Figure 3.2a. The green rectangles in Figure 3.2a, d, e, represent the areas etched by Gallium focused ion beam (FIB) technology, the arrow the etching direction. These steps provide the base for the antenna fabrication, defining the final orientation of the probe, as

reported in Figure 3.2b. In Figure 3.2c is presented the probe after the metal deposition by thermal evaporation, 3 nm of titanium as adhesion layer and 50 nm of aluminum. At this stage the tilted antenna has to be sculpted by Ga FIB milling. The main difficulty is given by the fact that the fabrication area is not perpendicular to the Ga beam, but tilted by 30°.

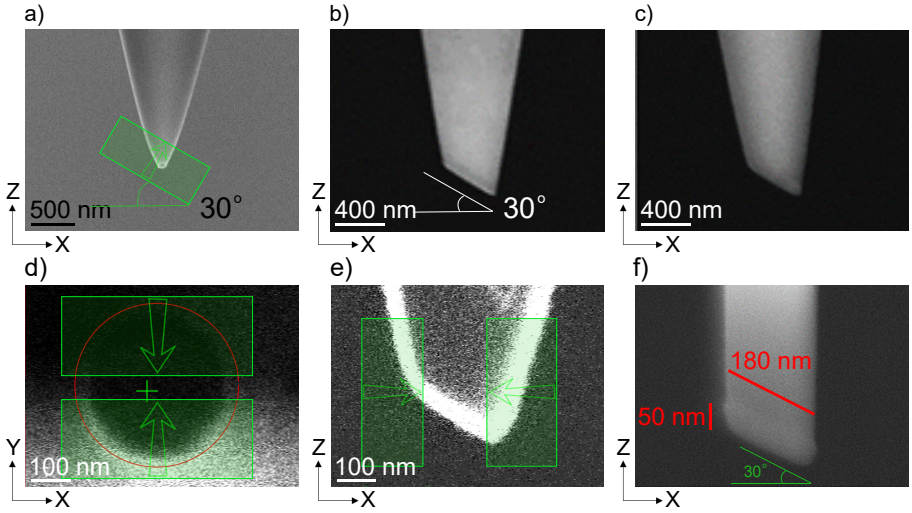

Figure 3.2: Fabrication steps of a 30° tilted dipolar antenna probe. (a) SEM image of a tapered end optical fiber, obtained by heat-pulling, cut by Ga FIB with a 30° tilted rectangular etching profile. The green rectangle and the arrow represent the milled area with its respective etching direction. (b) SEM image of the resulting glass fiber after the Ga FIB cut, showing a 30° tilted surface of a diameter of ∼400 nm. (c) SEM image showing the cut fiber after thermal deposition of 3 and 50 nm layers of titanium and aluminum respectively. (d) Ga FIB top view of an aluminum coated fiber as presented in (c) with etching steps depicted. The last step of fabrication provides a slice of metal with a lateral size of 50 nm laying on glass, defining the final lateral size of the probe. (e) Ga FIB lateral view of the result obtained in (d) step. The two lateral cuts represented by the green rectangles define the final length of the antenna. (f) SEM lateral view of a 30° tilted nanoantenna probe of lateral size of 50 nm and length of 180 nm.

The tilt constitutes potentially a serious problem, since working on a tilted surface introduces problems of beam astigmatism and divergence. In fact the nominal lateral size of the Ga FIB of ∼7 nm is referred to perfectly focused conditions on a flat surface, perpendicular to the Ga ion beam. To overcome such limitation, we fabricate the antenna in two steps. Figure 3.2d is a Ga FIB top-view image of the probe at the stage relative to Figure 3.2c. The two green rectangles represent the etched areas, located at a distance of ∼50 nm. This cut happens to be on a tilted surface. Nevertheless, as reported in the Ga FIB image of Figure 3.2e, it results in the fabrication of an homogeneous 50 mn thick aluminum slice. At this stage the additional lateral cuts shown in Figure 3.2e define the final length of the antenna. Figure 3.2f shows an SEM image of a 30° tilted dipolar antenna of a lateral size of 50 nm and a length of 180 nm, supported on a glass socket of a length of a few hundreds of nanometers. The glass socket has the double purpose of supporting the antenna and decoupling it optically and electrically from the rest of the probe, providing a stand-alone single nanoantenna probe.

3.3 Optical characterization of TDA probes

The TDA probe shown in Figure 3.2f is expected to provide a single bright spot of 50 nm lateral size with an excitation enhancement of at least a factor of ∼5x if excited with linear polarization, as shown in the FDTD total field intensity map located 15 nm below the antenna of Figure 3.3a. In the map is also shown the presence of a single hotspot, confirming that the probe only interacts at a single point. In order to test the optical properties we employ molecular beads of ∼20 nm size (section 2.4). Figure 3.3b is a probe scan over a continuously illuminated single molecular bead (section 2.5).

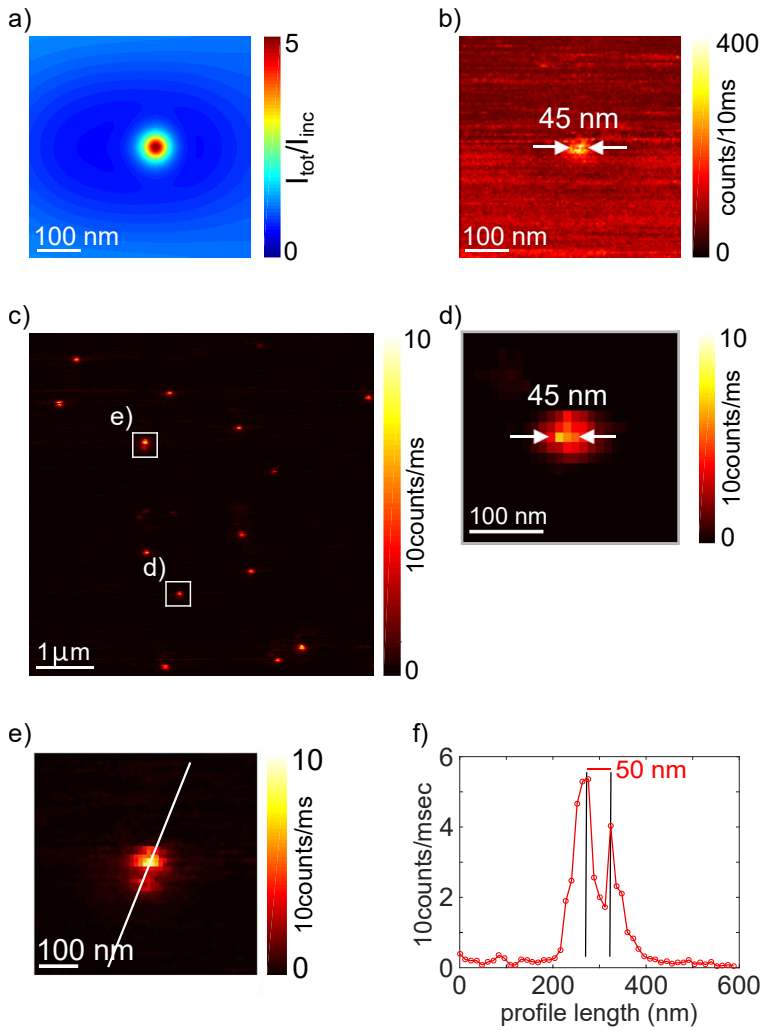

Figure 3.3: Nanoimaging of single molecular beads with a 30° tilted dipolar nanoantenna probe. (a) Total field intensity horizontal map located at a distance of 15 nm below the probe, calculated by FDTD at 670 nm wavelength with linear polarization. (b) Near-field probe scan on a single molecular bead. The probe provides a single hotspot of 45 nm (fwhm), with a fluorescence enhancement of a factor or 4x. (c) Sample scan of single molecular beads using a 30° tilted dipolar antenna. (d) Zoom of a single bead scanned in (c), showing again a single 45 nm fluorescence spot per bead. (e) Zoom of a detail in (c) with two very close beads. The profile shown in (f) reveals that the distance between the beads is of 50 nm. Excitation at 650 nm wavelength.

A single bright spot of 45 nm size (fwhm) is detected, with a fluorescence enhancement of ∼4x, in good agreement with the simulations. Furthermore, the tilted probe can be used for high resolution microscopy of molecular systems. Figure 3.3c shows a fluorescence image obtained by scanning the sample, keeping the probe continuously illuminated (section 2.5). Again, as shown in the zoom in Figure 3.3d, the probe provides a single, enhanced, sub-wavelength bright spot per bead, of 45 nm size. Compared to state-of-the-art near-field images obtained by flat dipolar antenna probes [19, 27, 29], the presence of a single spot per emitter provides a better resolution and emitter discrimination while preserving the enhancement, as proven by the zoom in Figure 3.3e. In this image are depicted two molecular beads at the sub-wavelength distance of ∼50 nm, as reported in the Figure 3.3f profile. The spatial extent of the two spots is big enough to ensure that it is not a single bead. The reason why one bead has a lower intensity than the other is that probably they are embedded at different depth in the polymer, hence in one case (brighter) the antenna can approach the emitter better than the other (darker).

An additional advantage of the tilted dipolar probe is given by the relatively small contact area. Indeed, in this case only the lowest part of the antenna is interacting with the sample. As an important advantage, the 30° titled antenna probes provide better topographical characterization of the sample than the flat ones. In Figure 3.4a, b are reported respectively a fluorescence and a topography image of molecular beads. We decided to use molecular beads in order to have isotropic absorber and emitters, since they are made of hundreds of molecules randomly oriented in order to test the total intensity of field of the antenna hotspot. Since in this specific case the beads were emerging a few nanometers out of the flat polymeric layer, thanks to the low contact area of the probe, it is possible to correlate the fluorescence emitted by each molecular bead with its physical position with high resolution.

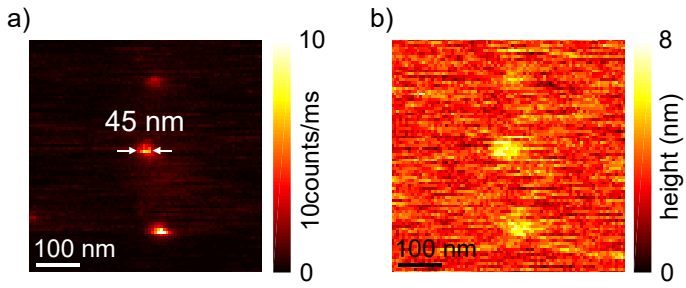

Figure 3.4: High resolution optical and topographical images with 30° tilted dipolar nanoantenna probe. (a) Near-field optical image providing the emitters position with a 45 nm fwhm single spot per emitter. (b) Topographical image, with high precision information about the physical position of the emitters, thanks to the small contact area of the probe. The beads are emerging from the flat thin polymeric layer of a few nanometers. The brightest spots are the ones that emerge the most outside of polymeric layer, since they are more accessible to the probe. Excitation at 650 nm wavelength.

The widths of the fluorescence spot provided by the tilted probe are the result of the convolution between the antenna hotspot and physical size of the ∼20 nm molecular beads. Considering that our detected single spot fwhm is comparable to the expected value, we conclude that the bead size is negligible with respect to antenna bright spot lateral size. The width of the spots presented in the topography map of Figure 3.4b are the result of convolution between the antenna part that interacts with the sample and the physical size of the molecular beads. The comparison of the topography and fluorescence images shows that the beads that are emerging the most out of the polymeric layer (Figure 3.4b) exhibit a higher fluorescence intensity (Figure 3.4a). This is due to the fact that the first ones are more accessible to the probe than the others and therefore experience a higher excitation enhancement.

3.4 Optical resolution limit of TDA probe

Considering the promising optical performances of TDA probes, we asked ourselves what is the theoretical limit of their light confinement capability. Advanced nanofabrication technologies based on He FIB microscopy allow the sculpting of highly precise nanostructures, with a control of a few nanometers [67]. Inspired by novel scenarios provided by this technology, we calculated the optical properties of 30° TDAs similar to the one presented in Figure 3.2f resonant at 670 nm wavelength, with an additional sharp element (needle) or thin cut groove at the bottom, as depicted in Figure 3.5a and Figure 3.6a. In both cases the probe is located at ∼10 nm distance from a glass substrate and it benefits from a strong plasmonic resonance (not significantly influenced by such small modifications) and supports the tiny metallic protrusion where an extreme level of light confinement occurs.

We studied two cases of TDAs with sharp needles at the bottom, one with cylindrical shape and a radius of curvature of 5 nm at the bottom and one with conical shape and a radius of curvature of 0.5 nm at the bottom, both needles extend for 10 nm under antenna. The total field intensity maps presented in Figure 3.5a insets, show a very high level of field enhancement and confinement in the proximity of the metallic needles. The total intensity enhancement is particularly sensitive with respect to z distance below the probe, as shown in left part of Figure 3.5b. The maxima excitation intensity enhancement for the two types of needles of 5 and 0.5 nm radii of curvatures are close to 500x and 1400x respectively in contact with the metal. They progressively decreases at higher z distances (d_z), but remain in the order of a few tens of times enhancement for $d_z < 10$ nm. Regarding the light confinement capability of the probe, we report in the graph in Figure 3.5b (right) the fwhm of the hotspot with respect to z distance. The minima fwhm are of ∼3 and ∼1.5 nm, with the antenna needles in contact. The rapid decrease

of field enhancements and increase of fwhm with the z distance is due to the strong field gradient and divergence around the needles, a direct consequence of very high light confinement. Indeed the sharpest needle provides a higher level of light confinement, and for this reason both enhancement and fwhm respectively decrease and increase with z distance faster than the other case.

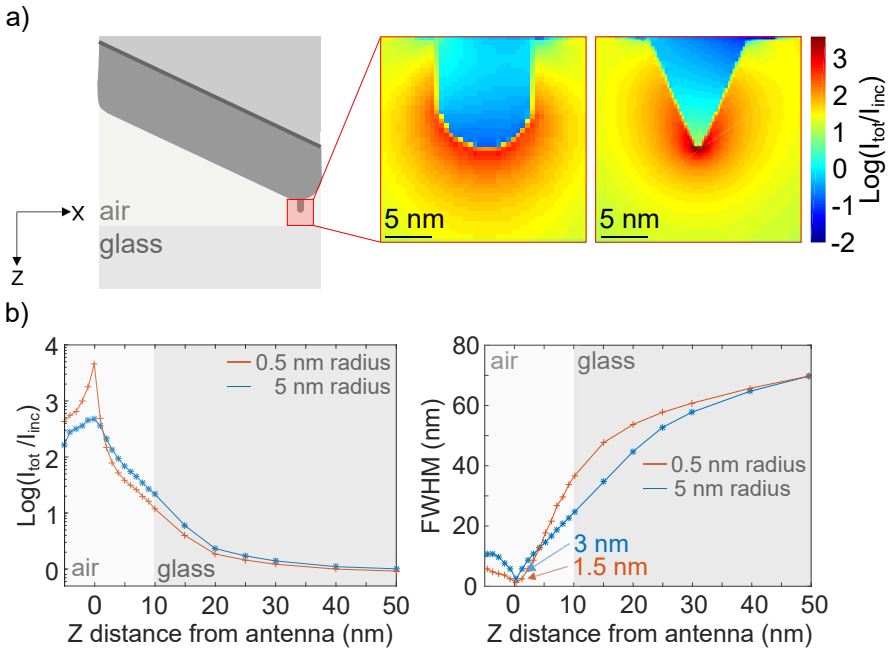

Figure 3.5: Optical resolution FDTD study of very sharp 30° TDA probes. (a) Sketch of a 30° TDA probe, with a sharp lowest part (needle). The needle is positioned at a distance of 10 nm from the glass substrate. Zoomed insets are total field intensity maps around needles of 5 (left) and 0.5 (right) nm radii of curvature. (b) Graph on the left shows dependence of the total near-field intensity enhancement calculated below the needles, with respect to antenna z distance. (b) Graph on the right shows dependence of the full-width half-maximum (fwhm) of the needles hotspot, for the total near-field intensity, with respect to the z distance from the antenna. The probe is located in air. Excitation at 660 nm wavelength, with linear polarization. The initial radius of curvature of the TDA lowest edge is of 25 nm.

If on the one hand the presence of such small needles at the bottom of a TDA probe provides higher levels of light confinement and intensity enhancement, on the other one it requires a very high level of nanofabrication and operation skills, given the high mechanical fragility of such small suspended objects.

In order to overcome such fabrication limitations we studied another type of TDA with a sharp cut at the bottom of 5 nm size in X direction and 10 nm in Z direction, as shown in Figure 3.6a sketch. In this case the fabrication only requires a single cut located in antenna lowest part. Additionally, the lack of small parts suspended at the bottom of the probe makes it much more robust than the previously discussed cases with needles. Nevertheless, the total field intensity map presented in Figure 3.6a inset shows a relatively high level of field enhancement and confinement in the proximity of the cut metallic part. Such enhancement is due to a combination of antenna resonance and proximity effect of the metal, more than an effective gap mode. In the specific case, the field enhancement in proximity to the two cut metallic edges is not symmetrical, but the majority of the enhancement corresponds to the right edge, closer to antenna end. In fact below antenna we find two close high intensity spots of which the right one is 50% more intense than the other. In the following discussion we considered the hotspot fwhm in x-direction as the one of the more intense spot located under right edge of small cut. The total field intensity enhancement is still sensitive with respect to z distance below the probe, as shown in left part of Figure 3.6b. The maximum excitation intensity enhancement for such system is close to 200x in contact with the metal. The enhancement decreases progressively for higher z distances (d_z), but remains in the order of a few tens of times enhancement for $d_z <$ 10 nm, with actually higher enhancement values than needle cases for 5 nm $< d_z <$ 10 nm, the typical probe-sample operating z distance. We report in the graph in Figure 3.6b (right) the fwhm in x-direction of the hotspot with respect to z distance. The minimum

fwhm is of ∼2 nm, with antenna in contact, while in the range of 5 nm < d_z < 10 nm this configuration performs slightly worse than the needle cases described above, since it only provides confinement in X direction.

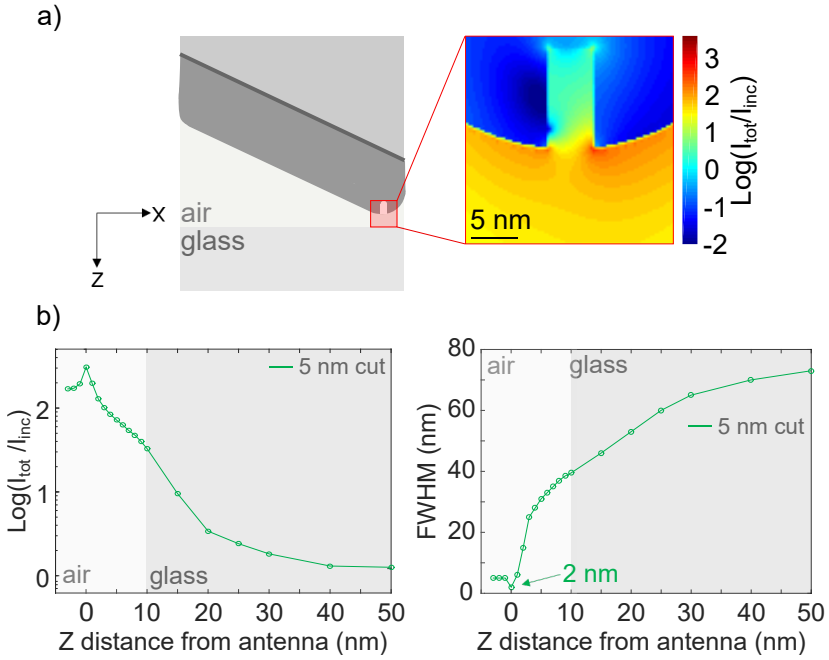

Figure 3.6: Optical resolution FDTD study of a 30° TDA with a thin cut at the bottom. (a) Sketch of a 30° TDA probe, with a sharp cut at lowest part. It is positioned at a distance of 10 nm from the glass substrate. Zoomed inset is total field intensity map around 5 nm width cut in X direction. (b) Graph on the left shows dependence of the total near-field intensity enhancement calculated below the sharp cut, with respect to antenna z distance. (b) Graph on the right shows dependence of the full-width half-maximum (fwhm) of the hotspot under antenna, for the total near-field intensity, with respect to the z distance from antenna. The probe is located in air. Excitation at 660 nm wavelength, with linear polarization. The initial radius of curvature of the TDA lowest edge is of 25 nm.

To summarize, our considerations imply that when increasing the level of light confinement and field enhancement on TDA probes

as discusses above, the emitter-tip distance becomes more and more crucial in such systems. In fact, the last one is a key point in NSOM technique. The probe-surface distance is ultimately limited by the shear-force feedback loop operation that controls the antenna-surface z distance (section 2.5). The other critical aspect is relative to the depth at which the emitter is embedded in the sample matrix. The optical stability of SPEs is normally strongly dependent on the thickness of such protective layers [69, 81, 82]. A novel class of SPEs is represented by the ones located in so called 2D materials [12, 83], that are in principle promising due to their stability and accessibility. According to our calculations, considering such emitters in 2D materials, operating the NSOM with a minimal force feedback distance and using the tip with a 0.5 nm radius of curvature protrusion would provide an extreme level of light confinement, with a single spot of 1.5 nm fwhm and three orders of magnitude excitation intensity enhancement.

3.5 Design and fabrication of MGTDA probe

Apart from sharp tips and gap, an alternative light confinement is offered by the sharp transition at the interface between different materials, due to abrupt discontinuities of refractive indices. The field intensity map of a 30° tilted antenna in Figure 3.1b shows the presence of two hotspots located at different heights. A close look to the hotspots reveals a strong field confinement at the metal-glass interface, even stronger than the enhancement at the surface. In a TDA probe, this discontinuity is located on the probe side, where the metal-glass transitions are located, making it inaccessible to emitters.

In order exploit light confinement due to sharp metal-glass transition, we developed a so-called metal-glass interface 30° tilted probe (MGTDA), as represented in Figure 3.7a. Such a probe exhibits the same angular tilt as the TDA, with an additional sharp metal-glass

transition area located at its apex, accessible to SPEs embedded in the sample. According to the FDTD total field intensity map shown in Figure 3.7b, the antenna still exhibits two hotspots, and only one is close enough to the surface to interact with it. The simulation in Figure 3.7b also shows how the lowest hotspot is exactly located at the sharp glass-metal interface, as expected. The Figure 3.7c is an horizontal map of the total field intensity located 15 nm below the probe. It shows the presence of a single sharp hotspot of 50 nm lateral size and a total intensity enhancement of $\sim$10x. One of the main differences to the TDA, is that in the case of MGTDA the lowest antenna edge has a sharper triangular shape, as shown in Figure 3.7a, b. Nevertheless, MGTDA probe still exhibits a resonant behaviour, mainly dependent on its length, as reported in Figure 3.7d. This is due to the fact that for the probe resonance the sharp part of the antenna is negligible compared to the rest of the structure. The total field intensity enhancement is also correlated to antenna length, as described in Figure 3.7e. Figure 3.7e shows how in the visible and near-infrared the size increase determines an increase in absorption cross section, hence a higher enhancement. The colored numbers in Figure 3.7e representing the resonance wavelengths corresponding to some specific antenna lengths show the progressive resonance red-shift with antenna length increase. Furthermore, increasing the MGTDA probe length means decreasing the effect of this sharp part compared to the rest of the structure.

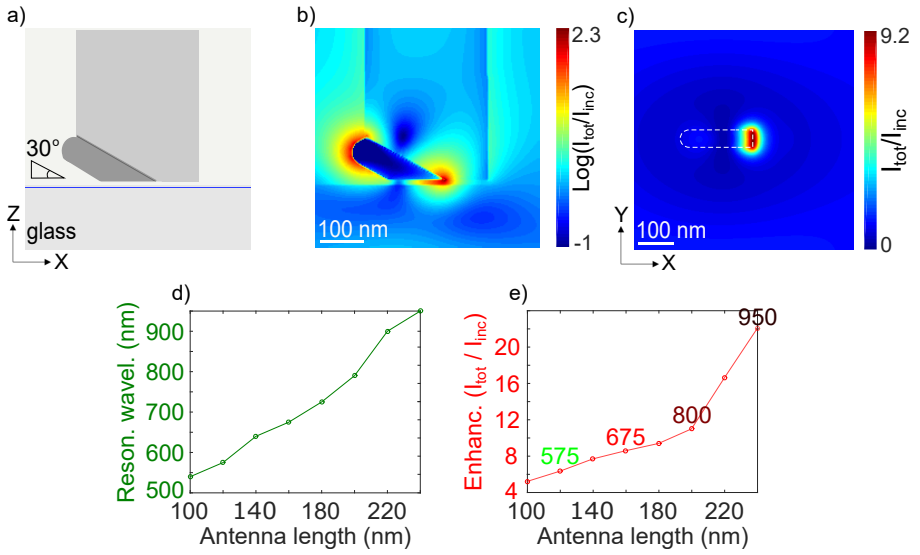

Figure 3.7: Optical properties of a metal-glass interface 30° tilted dipolar antenna probe, FDTD calculations. (a) Sketch of a 30° tilted dipolar antenna, with a sharp metal-glass transition located at the apex. (b) Total near-field intensity map of the probe at 670 nm wavelength,excited with linear polarization. (c) Total field intensity map calculated 15 nm below the antenna, at same wavelength. The antenna is represented by the white dotted line. (d) Dependence of antenna resonance with respect to its length. (e) Dependence of total field intensity enhancement with respect to antenna length. In e) are reported with the respective colors the resonance wavelengths for some specific antenna lengths to show that the enhancements correspond to different wavelengths.

Conversely, particularly short antennas are strongly affected by the sharp metallic part. In conclusion, according to the calculations presented in Figure 3.7, the use of a metal-glass sharp interface doesn't affect the level of light confinement, but increases the total intensity enhancement by a factor of ∼2x with respect to the previously discussed TDA.

The realization of a MGTDA probe requires a novel, ad hoc nanofabrication procedure. The first three steps of nanofabrication, dedicated to the preparation of the 30° tilted glass support

coated with metal are the same as already discussed in Figure 3.2a-c. Figure 3.8 shows the Ga FIB fabrication processes required for the realization of a MGTDA probe. To obtain such sharp materials transition, a probe is etched from the side as shown in Figure 3.8a.

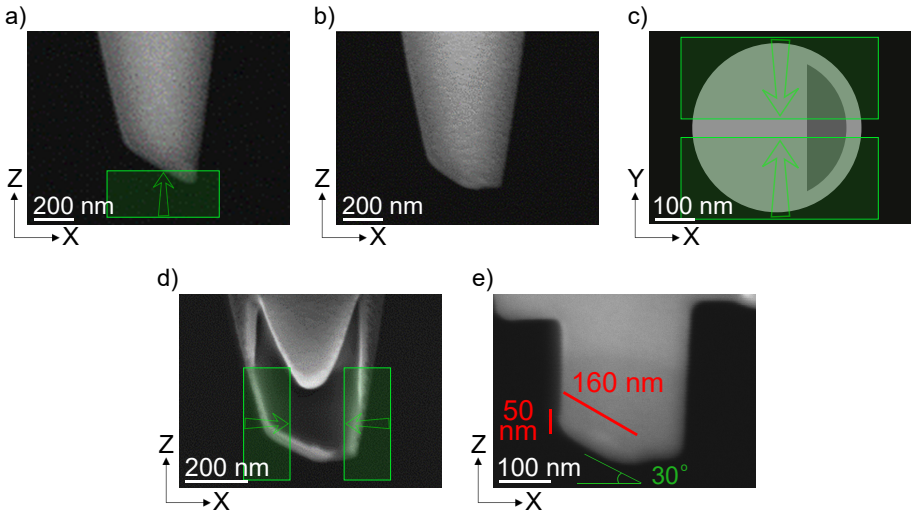

Figure 3.8: Nanofabrication procedures for the metal-glass interface 30° tilted dipolar antenna probe. (a) SEM lateral view of a 30° tilted cut fiber, aluminum coated, as presented in Figure 3.2c. The green rectangle represents the etching area, performed by Ga FIB. (b) SEM image of lateral view, showing the result of the etching step depicted in (a). (c) Sketch of (b) top view, with the next etching step. Two rectangular areas are milled from top, leaving a metal-glass slice of a lateral size of 50 nm, as shown in (d). (d) SEM image of lateral view of the structure obtained after (c). The milling of two rectangular areas defines the final length of the antenna probe. (e) SEM image of lateral view of the final result obtained, a 30° tilted dipolar nanoantenna, with a length of 160 nm and a lateral size of 50 nm. It provides a sharp metal-glass transition at the apex.

The result of such step is shown in Figure 3.8b. At this stage at the bottom of the probe we have a metal-glass transition, the next steps define the antenna structure. In Figure 3.8c a sketch shows with a bottom view the state of the probe at this stage, while the

two green rectangles, located at ∼50 nm distance, represent the subsequent etching steps. The result of this material milling is shown in Figure 3.8d. What is obtained is a structure similar to the one presented in Figure 3.2e, however this time at its bottom both metal and glass are exposed. The last step of nanofabrication is depicted in Figure 3.8d. With the lateral etching of two rectangular areas the length, hence the resonance, of the probe is set. The result of the full process is shown in Figure 3.8e. A single nanoantenna of 50 nm lateral size and 160 nm in length, tilted of 30° is positioned at the apex of a glass support. At the lowest part of the probe is the sharp metal-glass transition area, where, according to our calculations, the majority of the electric field enhancement is concentrated.

3.6 Optical characterization of MGTDA probe

We tested the optical properties of the MGTDA probe again using ∼20 nm size molecular beads (section 2.4). Figure 3.9a is a fluorescence image of a single beads sample obtained with a metal-glass 30° tilted probe. It shows the presence of confocal spots of a typical size of ∼300 nm with single, sharp and bright spots superimposed. The zoom in Figure 3.9b shows a single bead fluorescence spot, with a high resolution sharp peak of 50 nm fwhm, enhanced by ∼3.5x. Compared to the expected excitation enhancement of ∼10x, described in Figure 3.7c, we obtain experimentally a value that is ∼3x lower. The zoom presented in Figure 3.9c explains such unexpected performance: the lowest part of the probe is indeed not perfectly flat.

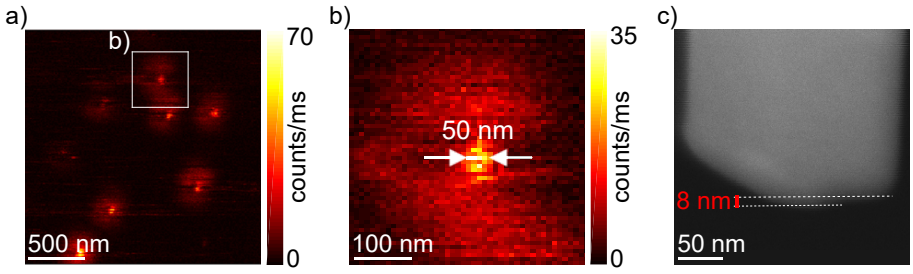

Figure 3.9: Optical characterization of a metal-glass interface 30° tilted dipolar antenna probe, with single molecular beads. (a) Nanoimaging of single molecular beads by means of a metal-glass interface 30° tilted dipolar antenna probe, showing a typical confocal spot with the presence of a sharp enhanced peak due to the interaction with the probe. (b) Zoom of a molecular bead in (a). It shows a single bright spot per molecular bead of a size of 50 nm and an enhancement of ∼3.5x. (c) SEM image of lateral view of the tip shown in Figure 3.8e: due to the different metal and glass Ga FIB etching rates, the metallic part of the antenna extends in Z ∼8 nm more than the glass part. Excitation at 650 nm wavelength, with linear polarization.

The nanofabrication step depicted in Figure 3.8a is the Ga FIB cut that defines the metal-glass interface lateral profile, the one that interacts with the emitters. Figure 3.9c shows how, due to different etching rates of glass and aluminum, at the apex of the probe the metallic part is longer than the glass part by ∼8 nm. This difference constitutes a physical obstacle that prevents the probe from efficiently approaching the surface of the sample where the emitter is embedded. The additional z distance between materials interface and sample surface limits the excitation enhancement of the emitter, preventing the full exploitation of the probe potential in terms of light confinement.

3.7 Conclusion

In this chapter we presented our implementation of the novel concept of titled dipolar antenna probes for NSOM applications. The

novelty of the 30° tilted dipolar probe is that, while keeping the dipole rod resonance, only one of the hotspots is close enough to the surface to interact with emitters. We focused on two different systems, TDA and MGTDA, with an additional sharp metal-glass interface for further light confinement.

We designed the optical properties of TDA probe by FDTD simulations. We found that, for both TDA and MGTDA aluminum antennas of 180-160 nm length, corresponding to a plasmonic resonance at 670 nm wavelength, the optimal tilt of the antenna is ∼30°. Such resonance can be engineered through antenna length control. We noticed how the systems are both resonant despite being tilted, the metallic lowest part of the MGTDA is very sharp at the materials interface. In the case of the MGTDA, the majority of the field enhancement is concentrated at the glass-metal interface. We have chosen aluminum for the fabrication of our probes because of its strong plasmonic activity and its mechanical stability and high resistance to oxidation compared to other metals like silver. Furthermore, due to its limited skin depth aluminum allows the realization of extremely small metallic protrusions that would otherwise be transparent to visible light if made of gold.

We developed a nanofabrication procedure that allowed us to have the full control on the shape, size and 3D orientation of both the types of antennas. Then we tested the probes optical performances using single molecular beads of ∼20 nm size. The measurements reveled that the TDA is providing a single hotspot of 45 nm fwhm and an average fluorescence enhancement of 4x, in good agreement with the calculations. Furthermore, due to small contact area of the 30° tilted antenna, it provides better quality topographical images than the flat ones. In the case of the MGTDA the probe provided a single hotspot of 50 nm fwhm. Nevertheless, due to fabrication limitations, the probe was not perfectly flat at its apex, and this limited the fluorescence enhancement at ∼3.5x, instead of the 10x excitation enhancement expected. We believe that, making use

of helium FIB technology, given the smaller etching rate compared to Ga FIB one, it might be possible to overcome the problem of non accessibility of the hotspot for the MGTDA. We noticed how both the probes have a superior optical and topographical resolution compared to state-of-the-art flat dipolar antennas, especially in densely packed SPEs systems.

Compared to a vertically oriented monopole or dipole antenna excited by radial polarization, our intermediate 30° tilted dipolar probe excited by in-plane polarization is mechanical more stable and robust. In fact our nanoantenna is located on a glass socket and extents only 50 nm in z direction. A metallic vertical monopole or dipole antenna would be sticking out of the glass support at the bottom of the probe for 100-200 nm in order to be resonant in the visible. Such long suspended metallic protrusion would be quite fragile and limit the probe lifetime.

We provided a theoretical study on the optical resolution limits of very sharp TDA probes, achievable by state-of-the-art nanofabrication techniques. We considered two configurations, locating at antenna bottom a very small metallic part (5 nm and 0.5 nm radii of curvature) or a small single cut (5 nm width) on an antenna edges with an initial radius of curvature of 25 nm. Our FDTD study on a TDA with a sharp needle at the bottom reported extremely high level of maxima field intensity enhancement ($\sim$500-1400x) and light confinement ($\sim$3-1.5 nm), depending on their radii of curvature. At the same time a strong dependence on the antenna-emitter z distance has been found. In the case of a TDA with a sharp single cut at its bottom, we report on smaller values of field intensity enhancement ($\sim$200x) compared to needle cases, but a less strong dependence on z distance. In contact such system still provides confinement down to $\sim$2 nm in x-direction.

In perspective we expect that, making use of such advanced strategies of extreme light confinement it will be possible to push

further the fundamental limits of light confinement and field enhancement.

Chapter 4

Nanoantenna Imaging and Control of hBN Defects

This chapter describes the high-resolution imaging of hexagonal boron nitride (hBN) photon emitting defect centers by means of a dipolar nanoantenna. The chapter starts with the introduction of the potential of such novel single-photon emitters for the realization of future ultra-stable single-photon sources, and the description of their optical properties. Then, the challenge of antenna-hBN emitter coupling is introduced. Photon time-gating is employed to discriminate the hBN-defect emission from the antenna luminescence. Subsequently, the experimental results are presented, employing both the dipolar antenna, in a resonant configuration and of a tilted dipolar probe, in out-of-resonance configuration. Surprisingly, we obtain high-resolution imaging of the emitters showing photon emission reduction. A theoretical model is presented that explains the antenna-emitter coupling both in excitation and emission. Finally, the theoretical limits of the near-field antenna coupling with hBN defects are exposed, and a novel configuration is proposed that provides one order of magnitude photon emission enhancement.

This work has been partially published in Nicola Palombo Blascetta, Matz Liebel, Xiaobo Lu, Takashi Taniguchi, Kenji Watanabe, Dmitri K. Efetov, and Niek F. van Hulst, *¨Nanoscale Imaging and Control of Hexagonal Boron Nitride Single Photon Emitters by a Resonant Nanoantenna¨*, in: Nano Letters 20 (2020) pp 1992-1999.

4.1 Introduction

Bright and stable single-photon sources are highly requested for emerging quantum technologies, such as quantum computing [84] or encryption schemes [85], where non-classical light sources are required, to provide on-demand indistinguishable photons, one at a time. To this end, quantum dots (QD) [86], organic molecules in crystalline matrices [6, 87], diamond nitrogen and silicon vacancy centers [88, 89], and 2D transition metal dichalcogenides (TMDC) [83] are all actively explored. Recent progress in efficient coupling of single molecules [87], NV centers [90] or QDs [91] to waveguides is paving the way to top-down fabricated single-photon sources on-chip, which ultimately might lead to the production of integrated quantum systems. In fact technologies like quantum cryptography [85] require on demand, bright sources of entangled photons. Quantum computation [84] as well might profit from the use of controlled high-purity and indistinguishable single photons sources since photons are well suited for the encoding and transportation of quantum information. To obtain a SPE configuration able to meet the high standards and performances required for quantum technologies is not expected to be an easy task. Nevertheless recent results involving QDs have been quite encouraging demonstrating MHz counts of entangled and indistinguishable photons [92], paving the way to the use of SPEs for quantum applications.

However, the applications of single photon emitters face intrinsic limits. The achievable brightness is limited by the luminescence lifetime and intermediate dark states. At room temperature, molecules tend to bleach, while both molecules and QDs tend to blink. The blinking and bleaching can be alleviated by embedding the molecules in a suitable crystalline matrix [69], or encapsulating the QDs in an engineered higher bandgap shell. Notably, the brightness can be boosted by enhancing the radiative rate (reducing

the lifetime) with an engineered plasmonic antenna at nanometer distance [21, 44]. Unfortunately, the necessary thickness of the protecting shell for photostability, such as the crystalline matrix around molecules or the diamond surrounding the NV center, do prevent the close proximity of plasmonic antennas.

Recently, the hexagonal boron nitride (hBN) atomic defect is attracting major attention as an alternative promising candidate for a high-performance single photon source [12, 93]. The hBN defects are reported to be photo-stable, free of blinking and bleaching, even at elevated operation temperatures as high as 800K [12, 45], even though the emission of indistinguishable photons from such emitters has not been demonstrated yet. Most importantly the emitter is stable in a hBN monolayer, of only nanometer thickness, readily accessible for local nanoscale control, for top-down fabrication and potential on-chip implementations. Despite the key advantages of photostability and accessibility, also the hBN-defect is still limited in brightness as a single-photon source, due to its intrinsic luminescence lifetime of several nanoseconds. The atomically thin hBN seems ideal for local enhancement by a plasmonic nanoantenna. To this end, one needs to optimize the coupling between the hBN-emitter and the nanoantenna by deterministic control of position, distance, orientation and resonance. A few attempts have been reported: Tran et al. relied on nanoantenna arrays [47] and Nguyen et al. used atomic force microscopy to couple individual hBN-defects to gold nanospheres [40]. Both studies reported a slight decrease in radiative lifetime alongside a minor increase in absolute photon emission rates, however in both cases the crucial emitter-positioning accuracy, was a limiting factor [40, 47]. Additionally, the experiments were performed in static systems, with fixed positions, complicating the systematic study of emitter-nanostructure interactions.

Here we present, for the first time, a systematic spatially resolved

study of the coupling of hBN-defect single photon emitters to resonant optical nanoantennas, with nanometric position-control and optical resolution of 40 nm. By nanosecond time-gating we separate the hBN-defect emission, to record lifetime interaction maps and quantify the interaction strength between emitter and antenna. Based on our findings we propose a nanoantenna-hBN-defect design, with an order of magnitude enhanced brightness, suitable for on-chip top-down fabricated configuration.

4.2 hBN defects optical properties

First, we analyzed the general optical properties of hBN-defect emitters (Figure 4.1). Thin hBN-flakes are exfoliated onto a quartz substrate, according to optical microscope observations of the flake optical contrast on quartz substrate their thickness is ∼5 nm. These pristine flakes show a relatively low defect-density of, on average, less than one luminescent site per 50x50 µm [70], moreover mainly located along the flakes' edges. As these areas are generally not well suited for antenna probe scanning, we opt for Argon plasma etching, followed by high temperature annealing, to induce optically stable hBN defects across the entire flake [70]. A typical luminescence image of a treated hBN flake, recorded with a 1.3 NA confocal microscope (section 2.5), is shown in Figure 4.1a. We observe a near-constant luminescence background, of approximately 30 counts/ms, across the entire flake and diffraction-limited emission sites distributed over the entire flake, and pronounced emission along the flake's edges. While the former are mainly induced during plasma etching, the latter are predominantly native defects. The emission spectra of individual defects (Figure 4.1b) show large heterogeneity, covering a spectral range from 550 nm to 700 nm with the mean emission wavelength for plasma-etching induced luminescent sites centered around 620 nm (Figure 4.1c), in agreement with previous [72, 94].

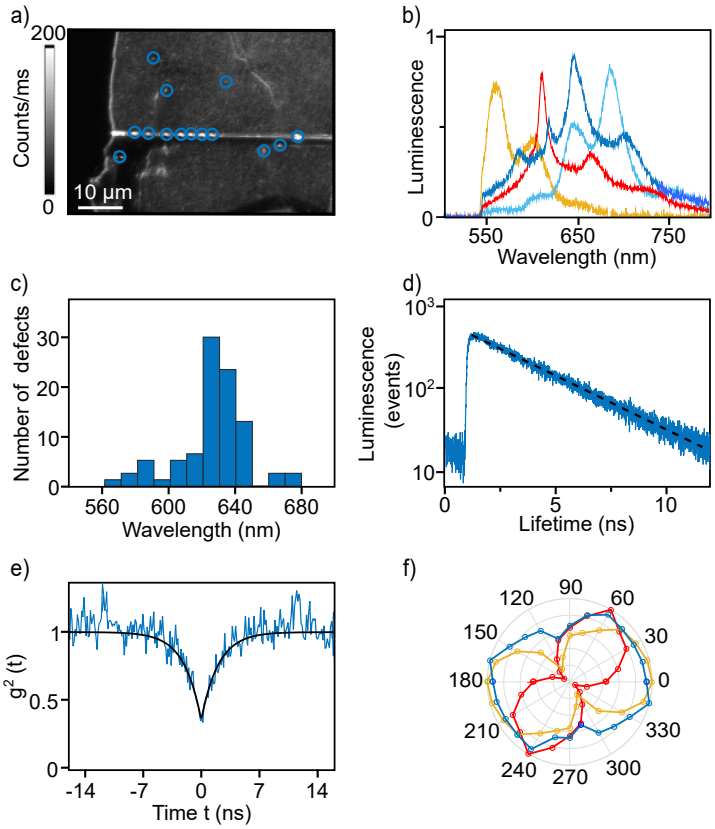

Figure 4.1: Optical characterization of hBN defects.(a) Confocal fluorescence image of an exfoliated hBN flake. The majority of the emittersis located at the edges of the flake with few, oxygen-plasma induced, defects being present on the flake itself. (b) Representative hBN-defect emission spectra. (c) Histogram representation ofthe spectral emission maxima of a total of ∼100 hBN defects. (d) Typical luminescence decay (blue)alongside single-exponential fit (black, dashed) with a lifetime of 3.5 ns. (e) Anti-bunching curve (blue) of the defect highlighted in (a) alongside an exponential fit (black). (f) Representative fluorescence excitation polarization dependence of three hBN emission sites with degrees of linear polarization (DOLP) of 0.1, 0.67 and 0.9, respectively. The typical power used for the measurements is of 300 kW/cm^2.

The photo-luminescence decay of individual defects shows a single exponential decay of tau=3.5 ns (Figure 4.1d), in line with

previously reported values of a few nanoseconds [12, 93]. To verify the single-photon-emitter nature of the hBN-defects, we record the second-order autocorrelation function, or anti-bunching curve. Here 5% of the measured hBN-defects does exhibit a dip below 0.5 at zero time delay, confirming single photon emission, while the majority of the defects does not exhibit single photon emission character [70]. A typical anti-bunching curve is shown in Figure 4.1e, exhibiting a g(2)(0) value of 0.4. This relatively high g(2)(0) value is due to the fact that roughly 20% of the collected photons comes from bulk emission of the hBN flake. Finally, we determine the dipole orientation of the emission sites by recording the luminescence response on the orientation of incident polarization (Figure 4.1f). The observed degree of polarization (DOP), computed as $(I_{max}\text{-}I_{min})/(I_{max}+I_{min})$, varies broadly from 0.1 to 0.9, without any preferred orientation with respect to the hBN lattice [95]. The occurrence of near-isotropic excitation probabilities intuitively agrees with the low fraction of single-photon emitting-defects, suggesting the presence of multiple emitters inside a typical 300 nm confocal spot of our microscope. The density of closely packed hBN defects probably depends on the plasma etching conditions, used to increase the number of emitters in the exfoliated hBN flakes (2.4).

4.3 The problem of hBN defects-antenna coupling

Next, we turn to controlled nanoscale coupling of the hBN-defect emitter to a nanoantenna. To this end, we employ a home-build scanning probe microscope (section 2.5), which allows to scan a nanofabricated antenna over a single photon emitter, at a constant distance using shear-force distance control [29]. Figures 4.2a and b show SEM images of the aluminum-nanoantennas probes employed in this study, fabricated onto the apex of a heat-pulled op-

tical fiber by focused ion beam milling (2.3) [29, 44]. The length of the 50x50nm cross-section Al antenna is chosen 160 nm to be resonant with excitation or hBN emission. The probe has been engineered taking into account the presence on the quartz surface of a thin (∼5 nm) layer of hBN material, with a refractive index of n=2.2 [96], following the simulation procedures explained in section 2.2.

The Al nanoantenna does show weak photon luminescence. Therefore, we compared representative hBN-defect luminescence to the antenna signal. Typically a fluence of 40 kW/cm2 is used, which is one order of magnitude below the fluences typically used to excite hBN-defects [12, 40], and prevents thermal damage of the nanoantenna. Figures 4.2c and d show confocal luminescence images of an isolated hBN-defect as well as the dipolar Al-nanoantenna, excited with circular polarization, while the antenna is kept about 20 nm from a clean quartz cover glass. Surprisingly, the weak antenna-emission is still two times brighter than the hBN-defect, due to its very small absorption cross section. In fact, the hBN emission is very weak, which represents a considerable challenge for the antenna coupling experiments, as the respective signals have to be separated. An obvious solution would be to employ spectrally selective detection; however the respective emission spectra exhibit considerable overlap (Figure 4.2e). Moreover, the intrinsic hBN emission-heterogeneity (Figure 4.2b, c) complicates spectral filtering for enhancing the signal-contrast as different detection filters would be necessary for each defect.

As an alternative to distinguish hBN and antenna, we employ time-gating of the collected luminescence signal (section 2.5). A comparison of the luminescence time-traces (Figure 4.2 f) shows a rapid decay, with <200 ps lifetime, of the antenna luminescence. After 2 ns the antenna-signal has essentially decayed to zero, while the hBN signal has gone down only half. Thus, time-gating allows

hBN-defect specific detection, in a post-processing manner, using time-correlated single photon counting detection.

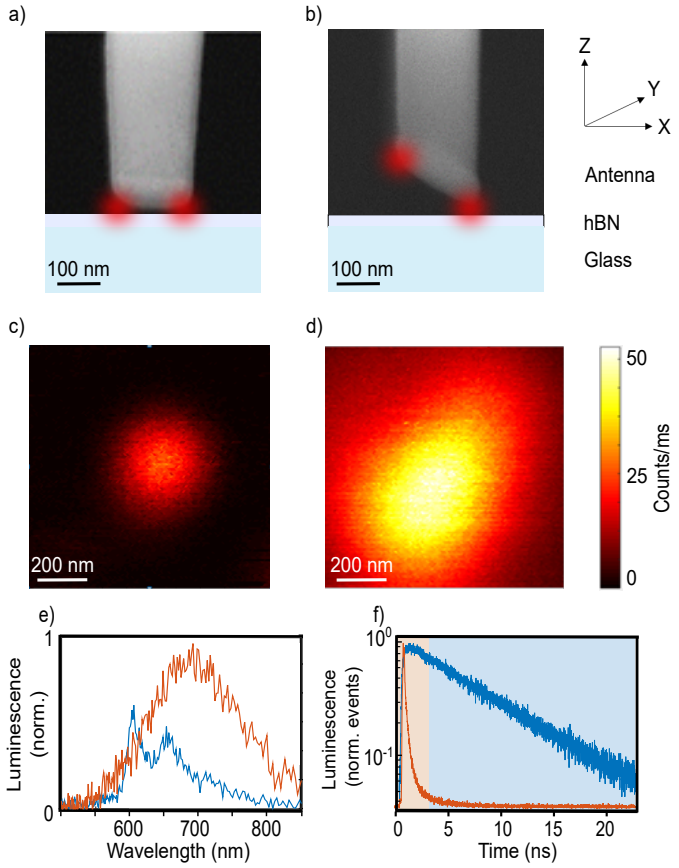

Figure 4.2: Comparing near-field probes and hBN-defects. (a,b) SEM images of an aluminium near-field probe alongside schematics of a typical coupling experiment for two different antenna configurations relying on either a flat (a) or a 30° tilted (b) dipolar antenna. (c) Confocal image of an hBN emission-site and (d) of the dipolar antenna shown in (a), positioned in close proximity of a clean quartz-coverglass, both images are plotted using the same intensity-scale. (e) Spectra of both antenna luminescence (orange) and hBN defect-emission (blue). (f) Photon-arrival histograms for the nanoantenna emission (orange) and the uncoupled hBN defect (blue). The typical power used for the measurements is of 40 kW/cm^2.

4.4 Resonant antenna near-field mapping of hBN defects

After characterization of hBN and antenna emission, we now turn towards antenna scanning experiments to acquire interaction maps on the nanoscale. As we already pointed out in section 4.1, in order to get a strong antenna-emitter interaction it is important to control relative distance, orientation and most importantly tune the resonance of the antenna with the excitation laser, as reported in Figure 4.3a. Considering such a probe in resonant configuration, it is possible to perform expereiments as the one schematically represented in Figure 4.3b. First, we position the hBN-defect of interest in the center of our confocal excitation spot. Once positioned, we raster-scan the antenna probe in close proximity across the emission site, while keeping illumination and sample geometry constant, and detect the photon emission as a function of the antenna position.

Figure 4.3c displays a near-field luminescence map with the antenna probe in close proximity to the hBN-defect. Here, we use the flat-dipolar Al nanoantenna (Figure 4.2a) fabricated with 160 nm length for spectral resonance at 620 nm, i.e. resonant with the excitation laser. Figure 4.3c shows a bright spot, approximately 300 nm in diameter, with two darker spots superimposed, slightly offset to the top right of the image, due to non-perfect alignment of the hBN-defect within the confocal illumination spot. The 300 nm spot is due to the antenna-luminescence, which is confirmed by the fact that for a retracted antenna one observes constant, uniformly distributed, h-BN-defect photon-emission, irrespective of the antenna-position, as shown in Figure 4.3d. The two darker spots are indicative of antenna hotspots, localized at the apexes of the antenna, where coupling is maximized. To quantify the analysis, we exploit the previously mentioned time-gating to separate the fast antenna luminescence (<2ns) from the slower h-BN emission.

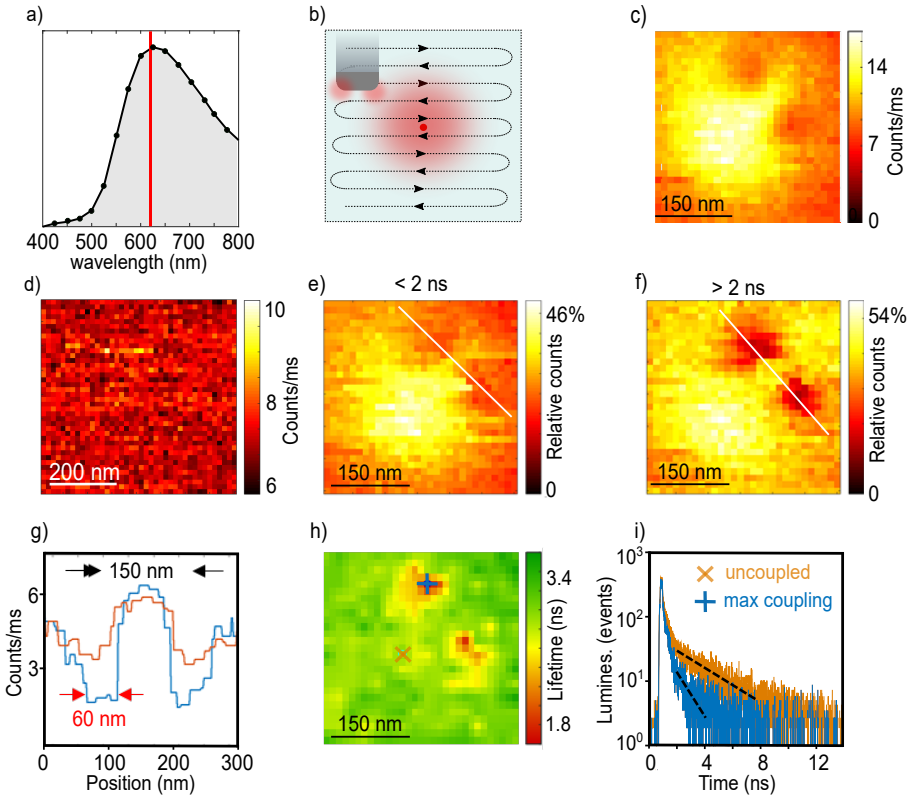

Figure 4.3: Near-field mapping of individual hBN emission centres. (a) Representation of calculated antenna resonance and excitation laser wavelength. (b) Sketch of a typical antenna probe scan over a continuously illuminated emitter. (c) Near-field image of an hBN emission centre using the flat dipolar antenna. (d) Near-field-like image of the same hBN emission centre without the presence of any dipolar antenna probe. (e-f) Time gated interaction maps using bins of 0-2 ns (left) and 2-25 ns (right). (g) Line profiles along the path indicated in (e-f). (h) Fluorescence lifetime-map obtained by fitting the 2-25 ns time-bin to a single exponential decay. (i) Photon-arrival histograms for the two points indicated in (h) alongside single-exponential fits (black dashed) indicating coupling-induced lifetime reduction.

We detect all photons in a time-tagged fashion, which allows the generation of arrival-time filtered images during post-acquisition analysis [74]. Figures 4.3e and f show respectively the result of

the time-gating analysis with the luminescence separated into two time-windows: 0-2 ns and 2-25 ns intervals. The first image contains mainly antenna as well as some hBN-defect contributions and therefore strongly resembles the initial interaction-map presented in Figure 4.3d. The second image, however, almost exclusively contains hBN-defect luminescence, exhibiting a markedly enhanced double-spot contrast, while the antenna luminescence spot is almost fully suppressed leaving a near-constant background across the entire image. Figure 4.3g further quantifies the effect of the 2 ns time-gating with an approximate 2-fold contrast-improvement. The hBN-defect luminescence shows two depletion spots of 60 nm, with maximum depletion approximately 75%, and separated by 150 nm, in agreement with the aluminum antenna length of 160 nm. We remark that these hotspot features are qualitatively typical for either vertical or isotropic oriented emitters coupling to flat dipolar antennas as previously shown [29]. Time-gating the hBN-signal (>2ns) facilitates the extraction of quantitative lifetimes under varying coupling-conditions, thus allowing generation of a full interaction lifetime map, as shown in Figure 4.3h. Here, the uncoupled hBN-defect exhibits a lifetime of about 3.5 ns, in agreement with the value presented previously (Figure 4.1d). Once entering a hotspot the lifetime decreases to approximately 1.6 ns, i.e. a reduction of 2.2 times (Figure 4.3i).

4.5 Non-resonant antenna near-field mapping of hBN defects

These observations are somewhat surprising, as the observed local antenna-defect coupling and lifetime reduction does not result in the anticipated luminescence enhancement. To concentrate the antenna-field further and allow a smaller separation between

antenna-apex and hBN-defect, we performed the experiment presented above with a 30° tilted dipolar antenna probe, which is excited out-of-resonance at 520 nm wavelength (Figure 4.4a, b).

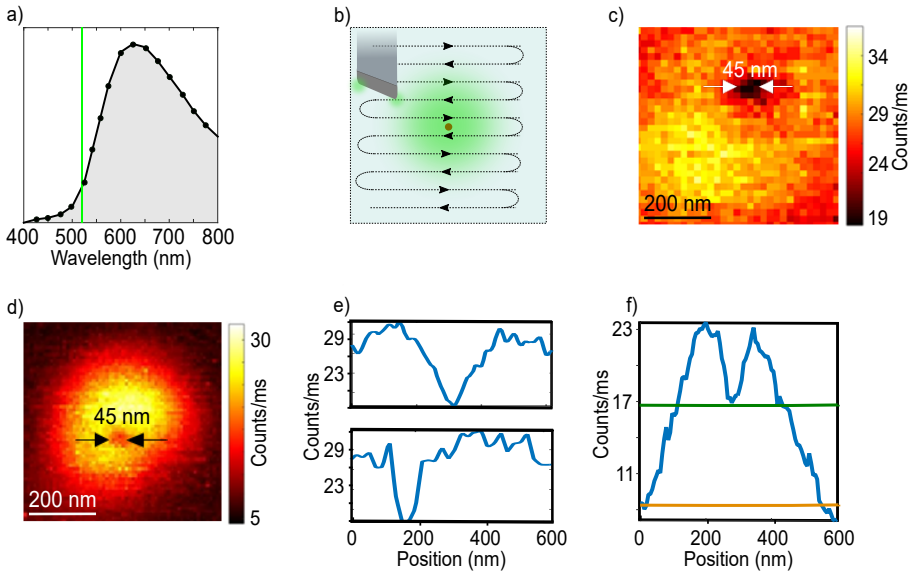

Figure 4.4: Imaging with a tilted dipolar antenna.(a) Representation of calculated antenna resonance and excitation laser wavelength. (b) Probe scan image of an hBN emission center with the tilted dipolar antenna shown in Figure 4.2b. (c) Near-field image (probe scan) of an hBN defect using a 30° tilted antenna, obtained scanning the probe over a continuously illuminated emitter. (d) Confocal fluorescence image of the same hBN defect with the antenna positioned above the confocal spot, scanning the sample. In (c) and (d) the emitter is localized with a 45 nm size depleted spot. (e) Horizontal (top) and vertical (bottom) profiles obtained from the antenna-scan (c). (f) Horizontal profile of the confocal image (d).

The chosen tilted antenna configuration allows a tighter spatial light-confinement compared to the previously employed flat antenna probe, thus providing higher resolution of the hBN emission center and better coupling efficiency. Indeed, using the tilted antenna, we observe a single interaction-spot exhibiting a full-width half-

maximum of only 45 nm (Figure 4.4c, d). The improved interaction-strength and light confinement of the tilted antenna-probe results in even more reduction in antenna-luminescence, as shown in the profiles reported in Figure 4.4e and f. The antenna luminescence is slightly decreased with respect to the hBN defect emission, as the antenna is excited out-of-resonance, yet the tilted antenna is unable to increase the hBN emission-intensity beyond its free-space level.

4.6 Modeling the hBN defect-antenna coupling

As such, both the flat-dipolar as well as the tilted-dipolar antenna experiments presented in Figure 4.3 and 4.4 , indicate that the antenna-hBN-defect interaction exclusively results in an overall emission depletion.

We have performed FDTD simulations to explain our observations results. Figure 4.5 presents an overview of the simulation results for the flat dipole antenna. The calculation-geometry is outlined in Figure 4.5a. Here, the hBN-defect is located inside the hBN flake, at a depth of 5 nm, while the antenna is located at a distance of 20 nm from the hBN surface, unless stated otherwise. The long resonant nanoantenna-axis is aligned with the x-direction. The calculated total electric field intensity in the vicinity of the antenna is shown in Figure 4.5b. Close to the surface, we observe an approximately 100-fold intensity increase, with respect to the incoming field. However, due to the high refractive index of hBN (n=2.2) as well as the high radius of antenna-curvature of 25 nm the intensity enhancement inside the hBN-flake is only slightly above unity [96]. As a consequence, the antenna-induced excitation enhancement is approximately unity and, hence, negligible.

Figure 4.1c compares the calculated normalized radiative and non-radiative rates, alongside the luminescence lifetime, for three different emission-dipole moment orientations. We concentrated on x-, z- and isotropic-oriented emitters.

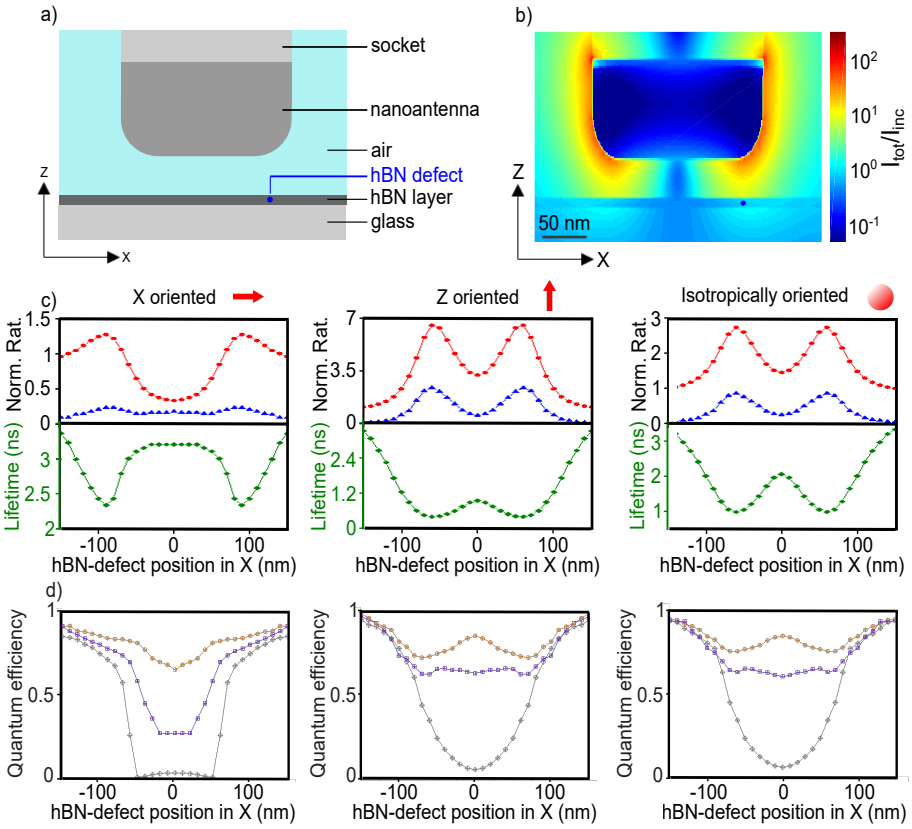

Figure 4.5: FDTD simulations of the excitation and emission properties of an hBN-defect located in close proximity to a dipolar nanoantenna. .(a) Sketch of the typical antenna-hBN emitter configuration during a probe scan. The aspect ratio is elongated by a factor of two in the z-dimension for the sake of clarity. (b) Electric field intensity map across the antenna when driven by a plane wave with a wavelength of 620 nm.(c) Simulated normalized radiative (red) and non-radiative rates (blue) as well as the lifetime-shortening (green) at an antenna to defect distance of 25 nm for x-oriented (left), z-oriented (centre) and isotropically-oriented emitters (right).(d) Quantum efficiency-simulations of hBN emitters located at different z-distances of 25 nm (orange), 15 nm (purple) and 3 nm (grey) for x-oriented (left), z-oriented (centre) and isotropically-oriented emitters (right).

We omitted the y-oriented case since it exhibits a characteristic

4-lobe pattern [29] which we did not observe in our measurements. We decided to include the isotropic case, as only 5% of all characterized hBN-defects showed anti-bunching, while the majority exhibited a very low DOP, suggesting that a large fraction of the hBN-defect emitters is composed of more than a single emitter. For all 3 cases, we observe a rate increase near the apex of the nanoantenna, both for the radiative as well as the non-radiative contribution, as expected for a resonant dipole-antenna. Assuming a luminescence lifetime of 3.5 ns, the reduction is plotted in Figure 4.1c. A direct comparison with the experimentally observed lifetimes (Figure 4.3f) reveals a quantitatively good agreement, with lifetime-minima separated by approximately 150 nm. Yet assigning an emission-dipole orientation based on the results presented is rather difficult.

To further understand our observations we simulated the emission quantum efficiency (QE) of the emitters, where we assume unity QE for uncoupled defects, based on previously reported literature values [97, 98]. As a result, upon interaction with the nanoantenna, the QE cannot be improved by enhanced radiative rate and can only be reduced by enhanced non-radiative rate (Figure 4.5c). Figure 4.5d reports the resulting QE values for the nanoantenna located 25 nm, 15 nm and 3 nm above the hBN surface, again for x-, z- and isotropic-oriented emitters. Indeed, QE depends strongly on the antenna-emitter configuration, in fact we notice the difference with the results shown in Figure 2.4c, due to different emitter orientation, emitter-antenna distance and different refractive index of the matrix where it is embedded. At a distance of 25 nm, we observe predominantly radiative decay with limited losses, but already at a distance of 15 nm, the non-radiative rate becomes non-negligible and at 3 nm we observe pronounced quenching with the QE reaching values below 10%.

Based on the simulations presented in Figure 4.5c and 4.1d we re-examine the experimental results (Figure 4.3). Firstly, the observed lifetime reduction shows quantitatively good agreement with

the lifetime-simulations and does confirm considerable hBN-defect-antenna coupling. The simulations indicate that the excitation enhancement is strongly screened-off, due to the high refractive index of hBN, therefore we concentrate our analysis on the emission intensities (Figures 4.5c, d). In silico, x-oriented emitters exhibit emission profiles with a minimum at the center of the antenna, which fails to reproduce our experimental double-spot observations. Instead, z- and isotropic-oriented emitters do show two local minima, exhibiting a QE decrease of 30% and 20%, respectively. The measured emission depletion is 50% to 75%, depending on the time-gating. The antenna is modelled as a perfectly smooth, single crystalline, metallic object (section 2.2). In reality, SEM images and optical measurements show that, depending on fabrication conditions, a typical Al antenna is polycrystalline with 20-40 nm size grains [66] which can explain the differences in emission-quenching (section 2.3). Overall, the simulations reported in Figure 4.5d suggest that, the hBN emitter is either z- or isotropic-oriented as for such cases and an emitter-antenna vertical distance of 25 nm we observe a double-lobe pattern (two local QE minima) rather than a central spot (single QE minimum), as expected for an x-oriented dipole. Based on these observations we conclude that the hBN-defect must be isotropically oriented as the z-orientation is unlikely given the in-plane excitation polarization. In other words, the hBN emission center measured in Figure 4.3 is most likely composed of more than a single emitter, all of which randomly oriented, thus forming an average isotropic emission-center.

The overall picture suggests that, in this specific configuration, luminescence cannot be enhanced by manipulating the emission properties. First, internal QE of the hBN-emitters is already near-unity. Second, the excitation enhancement is not sufficient to compensate for the antenna losses, which is a direct result of the high refractive index of hBN and the large index step to the air-gap between defect and antenna. As a result, the interaction between

antenna and hBN-defect leads to an overall emission-depletion, resulting in the observed dark spots at the antenna-apexes.

4.7 Ideal hBN defect-antenna coupling

We asked ourselves if the lack of photon emission enhancement is due to our specific experimental antenna-emitter configuration. Indeed our NSOM can only scan the probe at a fixed antenna-surface distance, in the order of a couple of tenths of nanometers maximum.

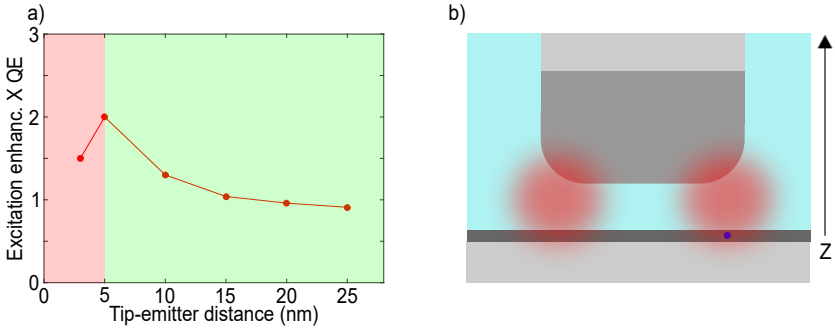

Figure 4.6: FDTD simulations of the total photon emission enhancement due to antenna-emitter coupling. (a) Total photon emission enhancement of an hBN defect coupled to a dipolar antenna, depending on their relative z distance. The emitter has been considered as isotropic. The higher total enhancement is obtained at a distance of 5 nm and is of 2x. (b) Sketch of the typical antenna-emitter configuration, the emitter is always located below one of the two antenna hotspots.

Figure 4.6a shows the FDTD simulated trend of the total enhancement $E_{tot} = E_{exc}$ x QE, where E_{exc} represents the excitation enhancement and QE the internal quantum efficiency of an approximately isotropic emitter, at different z distances from the antenna. In all cases the emitter is located below one of the antenna hotspots, as depicted in Figure 4.6b. According to Figure 4.6a, for vertical distances d>5 nm (green area) the E_{tot} is always close to unity,

peaking at 5 nm, where it reaches a maximum value of 2x. For d<5 nm E_{tot} decreases, entering the quenching regime (red area). These simulations show that, for a highly densely packed hBN emission center that most probably behave as an isotropic emitter, the maximum total enhancement due to the coupling with a resonant dipolar antenna is of a factor of 2, at a relative distance of 5 nm. Our FDTD simulations consider perfectly monocrystalline probes, without structural defects, underestimating their imperfections. Such a low total enhancement (2x) for a perfect antenna probe, most probably results in a near to unity effect for the real case, showing how novel antenna-emitter configurations are required for relevant photon emission enhancement.

An important insight from our scanning antenna results is the fact that one needs to avoid the low index air gap to gain hBN-defect emission enhancement by antenna interaction. An alternative configuration is sketched in Figure 4.7a. Here, the aluminum antenna is fabricated directly on exfoliated hBN. Such configuration can be realized fabricating the nanoantennas directly on the hBN layer by e-beam lithography, while the hBN defect in close proximity might be induced by gallium FIB exposure, as reported recently in the literature [99]. The nanoantenna directly on the hBN flake, with sharp metal-hBN transition, results in a local field intensity enhancement of two orders of magnitude inside the hBN layer (Figure 4.7b). The strong excitation enhancement can compensate for the decrease of QE due to antenna losses. FDTD simulations of the total excitation-emission enhancement, for an X and isotropic oriented hBN-defect emitter embedded inside a 5 nm thick hBN layer at 5 nm lateral distance from the antenna, show, respectively, 15x and 10x total enhancement of photon emission. Nguyen et al. [40] reported 3x emission enhancement for hBN coupled to a gold nanosphere. However, they did not employ time-gating in order to discriminate between hBN and gold particle luminescence,

thus probably overestimating the enhancement. The presented configuration design in Figure 4.7 enables an order of magnitude higher luminescence emission, i.e. a brighter single photon source. Importantly, the local excitation enhancement at the defect, will make the defect emission dominate over the intrinsic antenna luminescence, allowing direct hBN photon emission detection, without the need of time-gating.

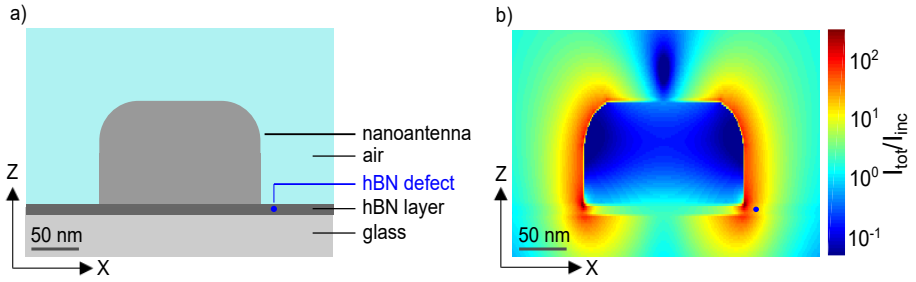

Figure 4.7: FDTD simulations of total photon emission properties of an hBN defect fabricated in close proximity of a dipolar nanoantenna. (a) Sketch of a dipolar nanoantenna directly fabricated on top of a 5 nm thick hBN layer. The hBN emitter is located inside the hBN layer at a lateral distance of 5 nm from the antenna, via Ga FIB edge cutting. (b) Vertical map of electric field intensity around the structure shown in (a) at a wavelength of 620 nm, with the emitter-position being indicated by the blue dot.

4.8 Conclusion

To summarize, we presented, for the first time, the experimental near-field coupling of a hBN-defect emitter to a tailor-made resonant plasmonic nanoantenna, which we systematically scanned through the hBN-defect near-field, to generate a nanoscale interaction map. We employed dipolar nanorod antennas, both in planar and tilted geometry. The latter revealed single-hotspot images with 45 nm FWHM, indicating that individual hBN emission sites are confined to an area in size smaller than few tenths of nanometers.

We quantified both the antenna-position dependent luminescence intensity as well as the luminescence lifetime and, furthermore, implemented a time-gating strategy to separate the defect emission from the considerable intrinsic nanoantenna luminescence. Our data show that by relying on a resonant antenna configuration and the aforementioned time-gating it is possible to localize hBN-emission centers with nanometric accuracy within a 75% depletion dip while, simultaneously, shortening the lifetime by a factor of 2.2.

The anticipated antenna enhancement was not observed, in our near-field coupling experiments. The presented FDTD modelling suggests that emission enhancement is indeed difficult to achieve. This manifestation is due both to the non-coupled QE being close to unity and the fact that the high index hBN-layer serves as a screening layer, shielding the defect of the enhanced field in the vicinity of the nanoantenna. The latter point has important implications for plasmonic-coupling to solid-state emitters in general. Even though they are promising candidates for single-photon sources their small cross-sections and resulting small emission rates calls for efficient enhancement strategies to ensure competitive performance when compared to other promising alternatives such as single molecules. Here, plasmonic cavities might, at first, seem like a valid strategy but the large refractive index of typical materials such as TMDCs, silicon or diamond prevents efficient electric field concentration. As such, it is necessary to reduce the materials' thickness to a minimum and to deterministically place the plasmonic antenna at a defined distance thus balancing excitation enhancement and quenching effects. At first, these constraints might appear prohibitive but the recent advances in nanofabrication based on He-based focused-ion-beam milling (section 2.3) and TMDC-manipulation put assembling such a coupled system within reach. Given that it is now possible to deterministically induce hBN-defects at well-defined positions within an hBN-layer [99] we used our experimental observations to propose a top-down fabricated on-chip single-photon source, based

on hBN-defects coupled to plasmonic nanoantennas, that could allow an absolute luminescence enhancement of 10 to 15-fold, thus providing a one order of magnitude brighter single photon source, with no need for time-gating detection.

Chapter 5

Single molecule control through antenna phase engineering

In this chapter we present the first controlled generation and optical visualization of cold spots, sub-wavelength areas with strongly suppressed electric field intensity, complementary to well-known hot spots where the field is strongly enhanced. The chapter starts introducing the problem of excitation interference between illumination and scattered light, in close proximity to a nanoantenna. Then a complete model is described that defines the necessary conditions for hot and cold spots generation, based on interference effect, by means of antenna phase engineering through lenght control. A single molecule is used to image both hot and cold spots, respectively with a dipolar and a detuned nanoantenna probe. The problem of emission interference (Drexhage experiment) is presented, discussing how it is possible to manipulate a single molecule emission, engineering the antenna phase at emission wavelength. It is shown for the first time the increase of lifetime due to the coupling to a detuned metallic nanoantenna and explain it in interferometric terms.

This work has been partially published in Nicola Palombo Blascetta, Pietro Lombardi, Costanza Toninelli, and Niek F. van Hulst, *¨Cold and Hot Spots: From Inhibition to Enhancement by Nanoscale Phase Tuning of Optical Nanoantennas¨*, in: Nano Letters 20 (2020) pp 6756-6762.

5.1 Introduction

It is well understood, that the emission of molecules or atoms is directly influenced by their immediate surrounding, equivalent to the radiation resistance of an antenna depending on its environment [53, 100, 101]. Indeed in his 1966 milestone experiment, Karl-Heinz Drexhage placed Eu+ atoms in front of a mirror and showed the luminescence lifetime becoming longer or shorter depending on the relative distance. This was intuitively explained as the Eu+ atom interfering with "its own mirror image" [53]. More strictly, as pointed out by Purcell [100], the local vacuum electromagnetic field, which is coupled to the molecular transition dipole, is altered, thus inhibiting or accelerating the radiative transition [101]. A large variety of optical cavity systems has been designed to control such coupling: concave mirror (laser) cavities, micro-resonators [49, 102, 103], photonic crystals with defects [104, 105] and many more. Photonic crystal cavities, with typically wavelength dimensions (diffraction limited), have been proven valuable to reduce the local density of states and thus inhibit radiative decay [55, 106, 107]. Beyond the diffraction limit, metallic plasmonic designs are exploited, such as surface plasmon polariton cavities [108, 109] or true localized plasmon nanoantenna systems such as spheres, cubes, rods [44, 54, 110]. Some indications of inhibition were reported [111, 112]. Ultimate confinement of the electromagnetic field has been achieved in gap-plasmon systems, with Purcell enhancement up to even a million times [80].

Most works on enhancing the emitters' radiative decay rate focus on minimizing the mode volume, tuning the resonance, and improving the resonator quality, achieving high Purcell factors in the range from 10^2 to 10^4 [19, 31]. Indeed, nanoantenna hot-spots have been shown to produce record enhancement, intense SERS signal and even single-molecule strong-coupling at room temperature [80]. Besides the high local field, the local phase is equally important.

For reflection at a mirror or interface the phase step is fixed, zero or π, depending on transition to a low or high index medium. For a photonic crystal, the reflection phase can be changed from zero to π by tuning the wavelength through the stop band [113–115]. For plasmonic antennas, the local phase depends strongly on specific shape and resonance conditions, providing even larger flexibility to engineer the local field. Indeed, plasmonic phased arrays, and planar optical components based on arrays of antennas ("metasurfaces") have proven effective for spatial beam shaping and directional control [39, 116]. Surprisingly the local phase has hardly been exploited to control the actual coupling to photon emitters.

Here we present phase tuning of local spots at a nanoantenna. Changing the antenna length, we tune the hot-spot out of phase, creating a nanoscale pocket with full suppression of the excitation field: a cold-spot [52]. We map the sub-wavelength cold-spots using single molecules as local field probes, and show the importance of balance between phase and amplitude to create such coldspots. Next, turning from the excitation to the emission, we present the first inhibition of emission close to a plasmonic nanoantenna. Tuning the phase of the antenna we create subwavelength volumes in which the fluorescence lifetime of a single molecule is lengthened, confirming the slowdown of radiative decay. Thus, we present Drexhage's experiment revisited, with a single molecule, in 3 dimensions and in a subwavelength volume.

5.2 Antenna-single molecule control: excitation effects

5.2.1 Excitation interference effects

Consider light reflected from a flat metallic mirror. An incident plane wave is reflected, maintaining a plane wavefront, acquiring

a fixed phase shift $\phi = \pi$ (Figure 5.1). A metallic nanoantenna scatters the incident field with a phase ϕ and amplitude that are structured on a subwavelength scale, depending on the shape, size, and resonance wavelength of the nanoantenna.

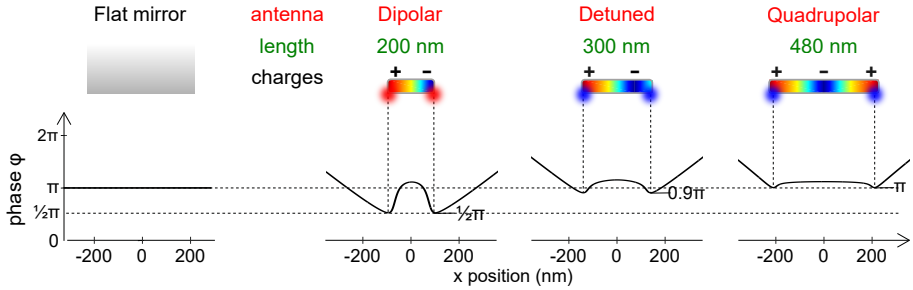

Figure 5.1: Phase of light scattered by a flat mirror or a nanoantenna. Phase of the optical field scattered at a nanoantenna. The phase shift ϕ of a plane-wave reflected on a flat metallic mirror, is simply a π phase shift at the surface. The phase shift ϕ profiles for nanoantennas of increasing lengths, 200 nm (dipolar), 300 nm (detuned), and 480 nm (quadrupolar) are position dependent. The phase shift ϕ at the antenna field maxima changes continuously from $1/2\ \pi$ to π upon increasing the antenna length. On each antenna is sketched the typical charge oscillation, due to the resonance condition, together with the charge accumulation points. The incoming field is linearly polarized along the main antenna axis.

In Figure 5.1 we show the phase profile of the scattered field for Al rod antennas of 200, 300, and 480 nm length, for an incident plane wave ($\lambda = 780$ nm) polarized along the rod. The 200 nm antenna supports a $\lambda/2$ mode (dipolar resonance) and introduces a localized phase $\phi = 1/2\pi$ at the rod ends, the hotspots of the dipole antenna. The 300 nm antenna is detuned with respect to the incident field (out-of-resonance) and the scattered field acquires a larger phase shift, $\phi = 0.9\pi$, at its ends. The scattered field becomes completely out-of-phase, $\phi = \pi$, for the 480 nm long rod, which supports a λ mode (quadrupolar resonance). Moreover,

the scattered phase also changes depending on the relative position to the antenna. The creation of such localized phase patterns is relevant for the tailoring of both the local excitation field and the local density of states (LDOS) experienced by a local emitter. The effective excitation field is the sum of the driving and the local scattering fields, which will interfere constructively or destructively depending on their relative amplitude and phase, generating subwavelength "hot spots" or "cold spots", respectively (depicted in Figure 5.1 as red and blue spots). Thus, the fact that amplitude and phase of the field scattered by antennas are both position- and resonance dependent provides a unique knob for interference and LDOS control on a subwavelength scale, through antenna detuning.

5.2.2 Resonant and detuned antenna excitation interference

First, we analyze the effect of detuning on the constructive and destructive near-field interference. Specifically, we compare the local field around a resonant and a detuned antenna.

In Figure 5.2 the electric field intensity distributions are plotted in the near-field of a 200 nm long dipole rod antenna. Figure 5.2a is a sketch of the typical resonant antenna probe-SPE sample configuration in our near-field measurements. In Figure 5.2b the three components of the total electric field intensities (I_x, I_y, I_z), as determined from FDTD simulations, are plotted, normalized to the incoming beam intensity (I_{inc}). We notice how I_y and I_z show respectively four and 2 bright spots on a dark background. For I_x, one appreciates the two bright spots (hot spots with $I_x > I_{inc}$), with excitation enhancement 3.5 $\times$, 50 nm fwhm, and 220 nm separation. The antenna field is surrounded by a bright external ring at a distance of $\sim \lambda/2$ in the x-y-plane. Remarkably, a large central

part of the intensity map shows areas with reduced excitation intensity, where the field is less intense than the incoming beam, $I_x < I_{inc}$, as result of interference with the incoming beam.

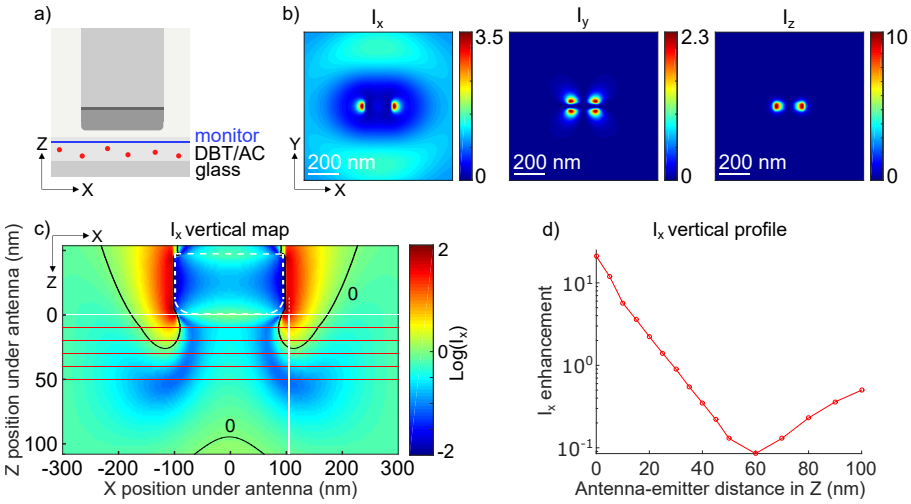

Figure 5.2: Electric-field intensity maps in close proximity of a $\lambda/2$ resonant nanoantenna.(a) Sketch of a $\lambda/2$ resonant nanoantenna located 10 nm on top of a glass surface, illuminated with a plane-wave linearly polarized along x. (b) FDTD calculated horizontal near-field maps of electric field intensities 15 nm below the nanoantenna. (c) Calculated x-field intensity vertical map cutting through the system. (d) Graph of the x-field intensity enhancement with respect to antenna-emitter z distance, along the white line in (c), zero is located at the bottom of antenna. The antenna is 200 nm long and resonant in excitation at 750 nm wavelength. The scales in x and z are different, the second one has been elongated for the sake of clarity. The horizontal red lines are located at 10 nm Z distance from each other. The field intensities are normalized to the incoming beam.

Figure 5.2c shows vertical x-z maps of the field intensity I_x. In very close proximity to the metal, the resonant dipole antenna generates over 100× excitation enhancement. The black unity contour line ($I_x = I_{inc}$) nicely outlines the enhanced zones at antenna edges, extending until z = 30 nm below. For a quantitative analysis, in

Figure 5.2d, we plot the vertical profiles of I_x along the white vertical lines in Figure 5.2c, at 110 x-distance from the antenna center, for hot spot and cold spot, respectively. The dipolar antenna mainly provides strong I_x enhancement for short-range interaction, until 30 nm where the incident field becomes suppressed.

In Figure 5.3 the electric field intensity distributions are plotted in the near-field of a 300 nm long detuned rod antenna. Figure 5.3a is a sketch of the typical detuned antenna probe-SPE sample configuration.

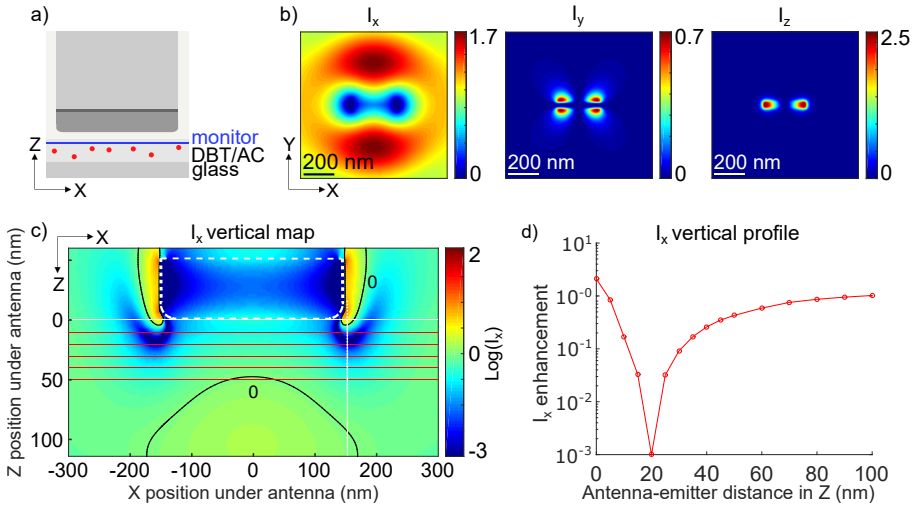

Figure 5.3: Electric-field intensity maps in close proximity of a detuned nanoantenna. (a) Sketch of a 300 nm length detuned nanoantenna at 10 nm Z distance from a glass surface. (b) FDTD calculated horizontal near-field maps of electric field instensities 15 nm below the nanoantenna. (c) Calculated x-field intensity of a vertical cut through the system. The map shows 2 destructive interference lobes. (d) Graph of the x-field intensity with respect to antenna-emitter Z distance, along the white line in (c), zero is located at the bottom of antenna. The antenna is detuned with a plane-wave at 750 nm wavelength, linearly polarized along x. The scales in x and z are different, the second one has been elongated for the sake of clarity. The horizontal red lines are located at 10 nm z distance from each other. The field intensities are normalized to the incoming beam.

In Figure 5.3b are reported the three components of the total electric field intensities for the detuned antenna. For I_y and I_z we notice a qualitatively similar behaviour compared to dipolar antenna, with respectively four and 2 bright spots on a dark background, but in general lower intensities. For I_x the in-plane I_x map looks radically different. The center of the map, instead of two bright "hot spots", now shows two dark spots, "cold spots", with local intensity $I_x = 10^{-5}$ far below the incident intensity I_{inc}, with 100 nm fwhm and 320 nm separation. The cold spots are slightly larger in size than the hot spots of the resonant case but nicely show that local enhancement can be turned into local reduction. The two cold spots are partially connected by a thinner area, also of reduced intensity. Also for detuned antenna we find a bright external ring at $\sim \lambda/2$ from the center of the intensity map. The vertical map for the detuned antenna presented in Figure 5.3c is markedly different to the resonant antenna case. First of all, we notice how I_x is much lower compared to the resonant case, with tiny unity contour lobes, much closer to the antenna edge and extending very shortly in the z-direction (<5 nm). Outside these areas, the detuned antenna mainly generates Ix reduction ($I_x < 1$), with two very dark lobes separated 320 nm in x and at a depth of z = 10-30 nm. These lobes are the zones of full destructive interference between the incoming and scattered light and correspond to the two dark areas (cold spots) shown in the in-plane map. Figure 5.3d shows that the field is suppressed already at 10 nm vertical distance under antenna, with maximum suppression (10^{-5}) predicted for z = 20 nm, extending until very deep ∼100 nm.

5.2.3 Nanoantenna length as a knob for resonance control

As we have seen, antenna resonance can be tuned through length control. In Figure 5.4 are shown the dependencies of dipolar, detuned and quadrupolar resonances with respect to antenna lengths.

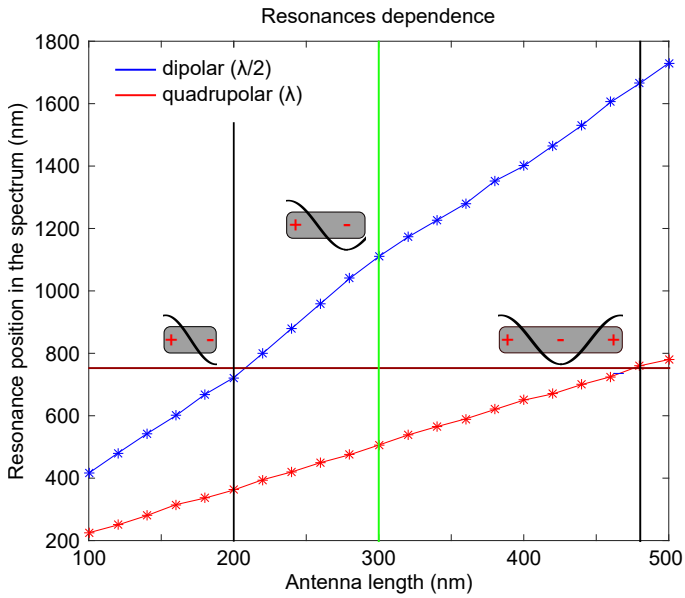

Figure 5.4: Dependence of nanaoantenna resonances with respect to length. FDTD calculated dipolar and quadrupolar resonances of nanoantennas used as near-field probes. Each antenna supports a dipolar and a quadrupolar resonance, located in different areas of the spectrum. At 750 nm wavelength the dipolar resonance ($\lambda/2$) is supported by a 200 nm lenght antenna, the quadrupolar resonance (λ) by a 480 nm lenght one. The 300 nm length antenna at 750 nm wavelength acts like an hybrid antenna. The nanoantenna is excited asymmetrically with a dipolar emitter source. The probes are located at 10 nm Z distance from a glass substrate.

Such results have been calculated with FDTD simulations, placing antennas at 10 nm Z distance from a glass support mimicking the sample. In order to efficiently excite quadupolar mode as well, that is a symmetric one for this reason also called "dark mode", antennas have been excited asymmetrically with a dipolar source. Both the resonances redshift increasing antenna length, in general dipolar resonance is red shifted with respect to quadrupolar one. At a wavelength of 750 nm, where the absorption peak of DBT molecule is located, the dipolar resonance is supported by a 200

nm lenght antenna, as already pointed out in previous sections. The quadrupolar resonance is supported by a 480 nm length antenna. An antenna of 300 nm length, has the two resonances respectively red and blueshifted with respect to 750 nm wavelength. This means that in this regime our 300 nm detuned antenna operates like an hybrid one, partially supporting dipolar and quadrupolar resonances. The dipolar part of resonance gives it scattering strength, the quadrupolar one makes that scattered light is strongly out-of-phase. This makes of it the most appropriate antenna for strong destructive interference, hence coldspots generation.

5.2.4 Nanoantenna excitation interference: complete model

To investigate how the local antenna phase can turn local field enhancement into suppression, we consider the antenna rod length as a continuous variable. Figure 5.5 shows the vertical (z-direction, in green in Figure 5.5a) profile of both field intensity and phase while tuning the antenna length continuously 100-500 nm. Panels b-d of Figure 5.5 show the scattered intensity Iscat, its phase ϕ, and the total intensity I_x, respectively, all for the x-field component, with intensities on a log-scale and normalized to incoming beam. The intensity of the scattered light I_{scat} (Figure 5.5b) shows a clear maximum for the dipole antenna length of 200 nm, which decreases when tuning the length out of dipolar resonance. The unity intensity contour ($I_{scat} = I_{inc}$) is indicate in red. The phase ϕ of the scattered x-field (Figure 5.5c) shows a strong dependence on both depth z and length. For z = 0 the phase ϕ increases from $\phi = 0$ for a very short antenna, to $\phi = \pi/2$ for the dipolar antenna, to a value of $\phi = \pi$ for a length of 480 nm, the quadrupole antenna. At the same time, ϕ increases with z, due to the delay accumulated by propagation in space.

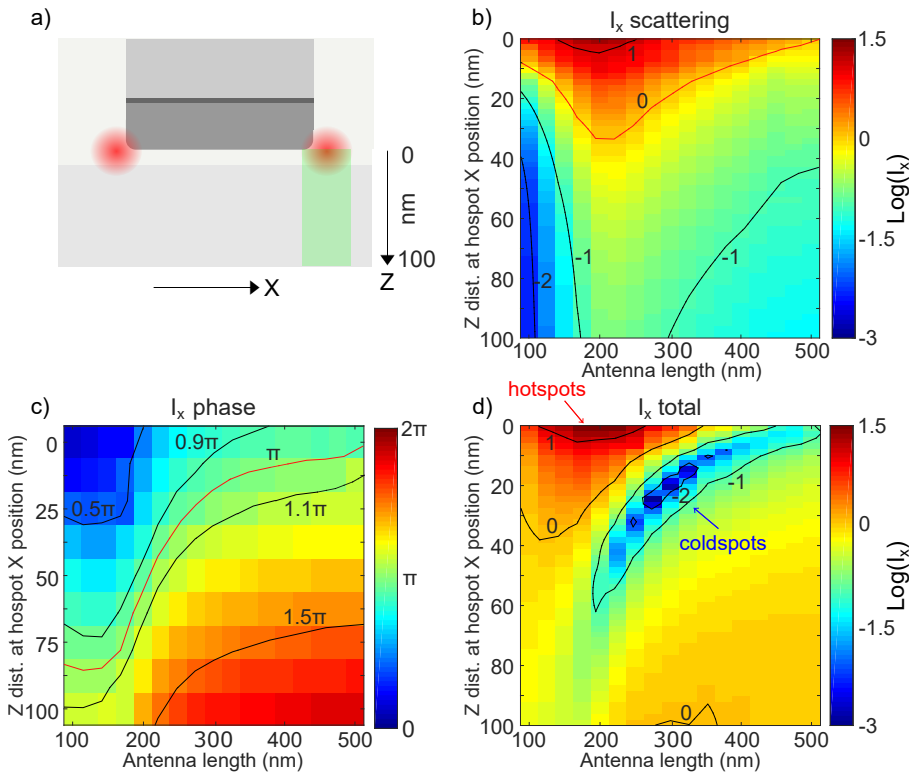

Figure 5.5: Excitation interference effect for nanoantenna near-field probes.(a) Sketch of a dipolar near-field probe with hotspots. The green rectangle represents the area under the antenna integrated in x and shown as intensity maps columns. (b), (c) and (d) are respectively FDTD calculated x-field scattered intensity, scattered phase and total intensity for different antenna lengths and Z distances. The x-field intensities are normalized to the incoming beam.

As a result, the contour line $\phi = \pi$ extends through both depth and length (red line in Figure 5.5c). The total intensity I_x (Figure 5.5d) shows the effective excitation field due to interference of I_{scat} with I_{inc}. The regions defined in Figure 5.5d with respect to antenna length and vertical distance under antenna, which are antenna phase-dependent, lead to hot and cold spots. The hot-spot region is centered at the 200 nm length dipolar antenna, with almost two-orders of magnitude enhancement at z = 0. The cold-spot

zone is wider, from 200 to 400 nm length detuned antenna and extends until z = 100 nm. Most excitation reduction ($I_x << 1$) occurs for a 300 nm antenna at z = 25 nm, with $I_x = 10^{-5}$, where I_x has been normalized to incoming beam intensity. The hot-spot region in Figure 5.5d is mainly dictated by the strong intensity I_{scat}, with $I_{scat} >> I_{inc}$, and negligible interference. On the other hand, the cold spots are located where we obtain full destructive interference between I_{scat} and I_{inc}, hence at locations where $I_{scat} = I_{inc}$ and $\phi = \pi$. Thus, the area with minimal I_x in Figure 5.5d corresponds to the region where the contour $I_{scat} = 1$ in Figure 5.5b crosses the contour $\phi = \pi$ in Figure 5.5c. By tuning the antenna phase right, one can obtain 100% full destructive interference. Moreover, the cold spot can be pulled into the near field zone, at only 25 nm distance, with a fwhm in depth of 20-30 nm.

In Figure 5.6 we show FDTD simulated X-field phase horizontal maps located 15 nm under antenna. Three cases are presented, for 200 nm (dipolar), 300 nm (detuned) and 480 nm (quadrupolar) length antennas.

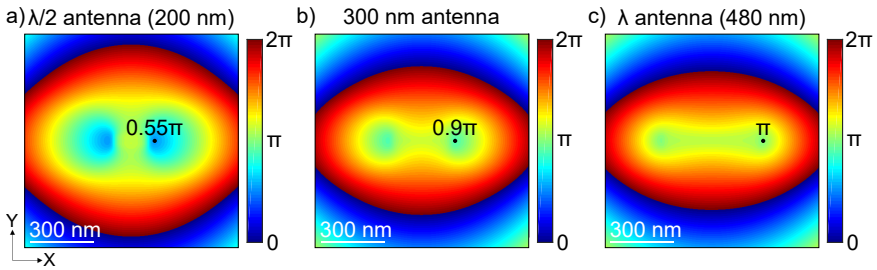

Figure 5.6: X-component scattered field phase horizontal maps. FDTD calculated X-component phase horizontal maps of the light scattered by the antenna, 15 nm under it. (a), (b) and (c) Phase maps of respectively a $\lambda/2$ antenna of 200 nm length, a 300 nm length antenna, and of a λ antenna of 480 nm length. The phase values indicated correspond to the hot/coldspots potitions.

In Figure 5.6a), the dipolar antenna case, we notice the presence of two spots with ϕ_x=0.55π. Increasing antenna length to 300 nm,

Figure 5.6b) shows two spots with ϕ_x=0.9π, while for quadrupolar antenna in Figure 5.6c) we find $\phi_x \sim \pi$ under antenna edges positions. These are xy positions where hot and coldspots are located. This means that for dipolar antenna case we get hotspots with an intermediate x-field phase value. For 300 nm antenna case, where we get coldspots, ϕ_x is strongly out-of-phase. The same happens for quadrupolar antenna in Figure 5.6c). Figure 5.6 shows how crucial ϕ_x is for coldspots generation.

5.3 Hot and cold-spots high resolution imaging

We now turn to the experiment. Aluminum nanoantennas of 200 and 300 nm in length are fabricated on a glass support by focused-ion-beam milling, to accurately define the proper length for phase control (Figure 5.7a,b), For more details about fabrication see section 2.3. The illumination wavelength is 750 nm, the x-field intensities are normalized to the incoming intensity. The laser power used for the measurements if of $\sim 1 KW/cm^2$, we verified that the emitters are not in a saturation regime, hence it is possible to use their fluorescence to map the excitation field.

To probe the field around the antenna, we use a single fluorescent molecule: dibenzoterrylene (DBT) embedded in anthracene (AC) thin crystals [69] (see section 2.4). DBT molecules are all oriented parallel to each other along the flake [117], providing x-oriented molecules, parallel to the antenna. The antenna is scanned in close proximity to the AC-flake at about 10 nm, as described in section 2.5. The DBT molecules are oriented along the x direction, parallel to the nanoantenna rods

In Figure 5.7c,d we show the measured field around the dipole and detuned antennas as probed by a DBT molecule for both antenna types, together with the FDTD simulated near-field maps.

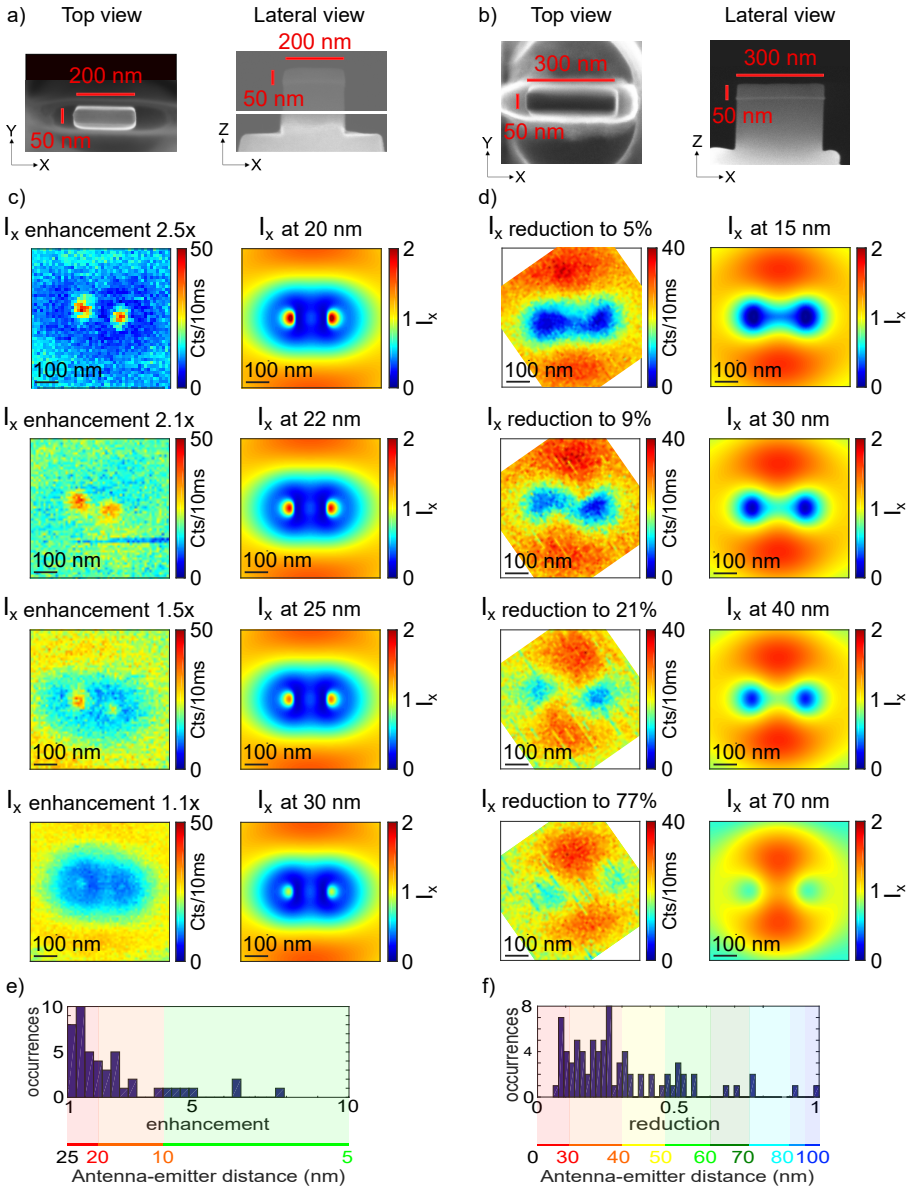

Figure 5.7: Single DBT molecule near-field hot and cold-spots mapping.(a, b) SEM images of dipole (200 nm) and detuned antenna (300 nm). (c) Measured fluorescence (left) and simulated (right) intensity maps of dipole antenna scans over a single DBT molecule, for different antenna-DBT distances. (d) Same as (c) for detuned antenna.(e, f) Distributions of the measured near-field enhancement and reduction, for both probes, with antenna-emitter z distances. The x-field intensities are normalized to the incoming beam.

For the dipolar antenna, we observe two bright spots of 50 nm fwhm, separated by 220 nm, in agreement with the FDTD simulations. Comparing the measured excitation enhancement to the calculated values, we estimate the relative antenna-emitter distance (z): the enhancements of 2.5×, 2.1×, 1.5×, and 1.1× (top to bottom) correspond to the z = 20, 22, 25, and 30 nm distance of the DBT molecule. As expected, with increasing depth z, the antenna effect becomes progressively weaker.

Notably, for the detuned antenna we observe the opposite behavior. Figure section 5.7d reveals the manifestation of two dark spots, 100 nm fwhm, separated by 320 nm, the first direct experimental demonstration of the predicted cold spots. Also, we notice the presence of two extended bright lobes at $\lambda/2$ distance from the center. Both the dark spots and halo are due to near-field interference, as confirmed by the simulations on the right. In the cold-spot area, the DBT fluorescence is strongly reduced, corresponding to an excitation intensity of only 5%. From top to bottom, we present antenna scans over different DBT molecules, with excitation reductions to respectively 5%, 9%, 21%, and 77%, corresponding to z $\sim$ 15, 30, 40, and 70 nm. The destructive near-field interference is most effective at short distance and fades out at the longer distance z. Interestingly, the further away constructive interference lobes at $\lambda/2$ distance grow toward the center area for increasing z-distance, until bridging the center at 70 nm distance, in perfect agreement between experiment and theory.

Panels e and f of Figure sectio 5.7 show the distribution of measured excitation enhancement/suppression for different molecules. The maximum excitation enhancement for the dipole antenna is 8×, while the average value is 2.4×, corresponding to calculated z-distances of $\sim$8 and 15 nm, respectively. We only find excitation enhancement up to 25 nm, consistent with simulations (Figure 5.2c). The maximum excitation reduction, for the detuned antenna, is down to 5% for a calculated z-distance of $\sim$15 nm, while the mean

reduced value is 28%, for z = 40 nm. In agreement with our simulations (Figure 5.2c), the z-range affected by reduction extends much deeper toward 100 nm, confirming that cold-spot generation is mediated by interference effects.

5.4 Antenna-single molecule control: emission effects

5.4.1 Emission interference effects

Now we consider control of spontaneous emission, exploiting the local phase tuning of nanoantennas. We have shown above that the local excitation field can be largely suppressed, using the proper choice of antenna detuning; therefore, it should equally be possible to create points in which a quantum emitter would experience a lower LDOS, i.e., inhibition of the spontaneous emission, in agreement with Fermi golden rule expressed in equations 1.2 and 1.3. Here we address the engineering of subwavelength areas in the space with increased or decreased radiative decay rate Γ, i.e., local spots with fast and slow decay.

When a molecule, that we describe as a dipolar emitter, is emitting in close proximity to a light scatterer like a nanoantenna the fluorescence light scattered can interfere with emitted light at dipole position, modifying locally the LDOS. In Figure 5.8 are presented to sketches illustrating a dipolar emitter located in front of a flat metallic mirror (on the left) or a metallic nanoantenna (on the right). The first case is the well known configuration described by Drexhage in the sixties [53, 101]. Depending on mirror-emitter z distance, interference can be constructive or destructive. Thus the decay rate can increase or decrease, affecting emitter lifetime. When an emitter is in close proximity to a nanoantenna, again

the scattered light will interfere with emitted one at dipole position. This time scattered light intensity and phase will depend on antenna-emitter full position and on antenna resonance. This means that in principle, controlling antenna resonance, it is possible to engineer scattered field, hence interference at dipole position. The consequence of this fact is that we can exploit antenna resonance in order to control emitter decay rate and lifetime.

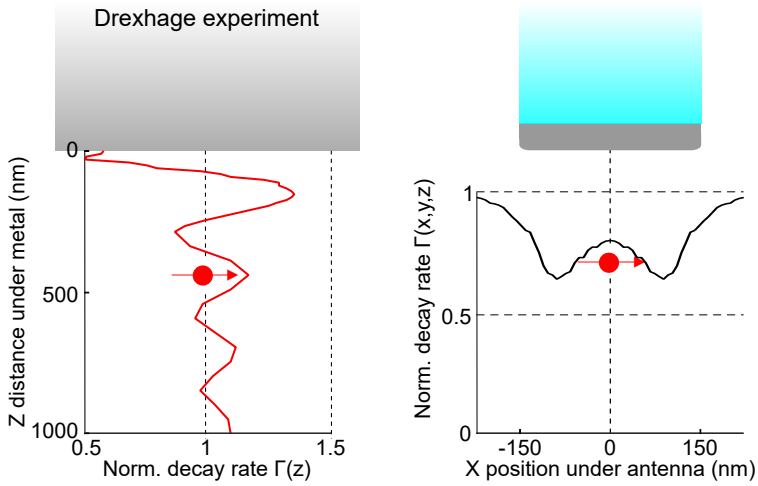

Figure 5.8: Sketches of a dipole emitting in front of a flat metallic mirror or a metallic nanoantenna. In the first case (Drexhage experiment configuration [53, 101]), the light emitted by the dipole is reflected by the mirror and interferes with the emitter at its position, modifying locally the decay rate. The change in decay rate is only z distance dependent. A dipole located in front of a metallic nanoantenna also experiences constructive or destructive interference with the scattered light, depending on the relative position and on antenna resonance conditions. In our case the dipole is located 50 nm under a 300 nm length antenna. Engineering antenna resonance we can control intensity and phase of the scattered light, hence affect interference and induce increase or inhibition of emission. Simulations have been performed for an emitter centered at 780 nm wavelength.

5.4.2 Modeling nanoantenna mediated emission effects.

In Figure 5.9a,b we present FDTD simulations of the decay rate and lifetime of an x-oriented dipolar emitter, located under respectively a 200 nm dipolar and 300 nm detuned antenna, as a function of the antenna-emitter relative position in the (x,z)-plane. For both antennas, the x-oriented emitter experiences a strong decay rate increase and lifetime decrease in close proximity to the antenna ends. The fastdecay spots, of 50 nm fwhm, are separated 220 and 320 nm for both antennas, respectively. The fast-rate zones extend for several tenths of nanometers in depth, ∼60 and ∼25 nm, respectively, with a maximal rate increase (Purcell factor) of 8× and 2.6×. For the detuned antenna case, we notice the presence of two distinct slow-decay spots, 100 nm in fwhm, separated by 200 nm, at a depth of ∼40 nm. In the spots, the relative decay rate is decreased to ∼0.55: local areas of spontaneous emission inhibition. To appreciate the decay rate dependence on antenna resonance, Figure 5.10 and Figure 5.11 show vertical x-z maps of the scattered x and z-field intensities $I_{x,scat}$, $I_{z,scat}$ (log-scale) on top and phases ϕ_x, ϕ_z for both antennas and the x-oriented dipole at the bottom. We modeled our molecule as a point dipolar emitter of ∼0.1 D ($3.2{\cdot}10^{-31}$Cm), a more realistic representation of the molecule that takes into account its real size and exceeds dipolar approximation goes beyond our computational capabilities. $I_{x,scat}$ is relatively strong under overall antenna structure and decreases with z-distance, while $\phi_x \sim \pi$ mainly under antenna ends. For a point-like dipolar emitter which is x-oriented at its position the x-component emitted intensity diverges while the other components are null, our calculations are defined only for distances from the dipole bigger than 0.5 nm.

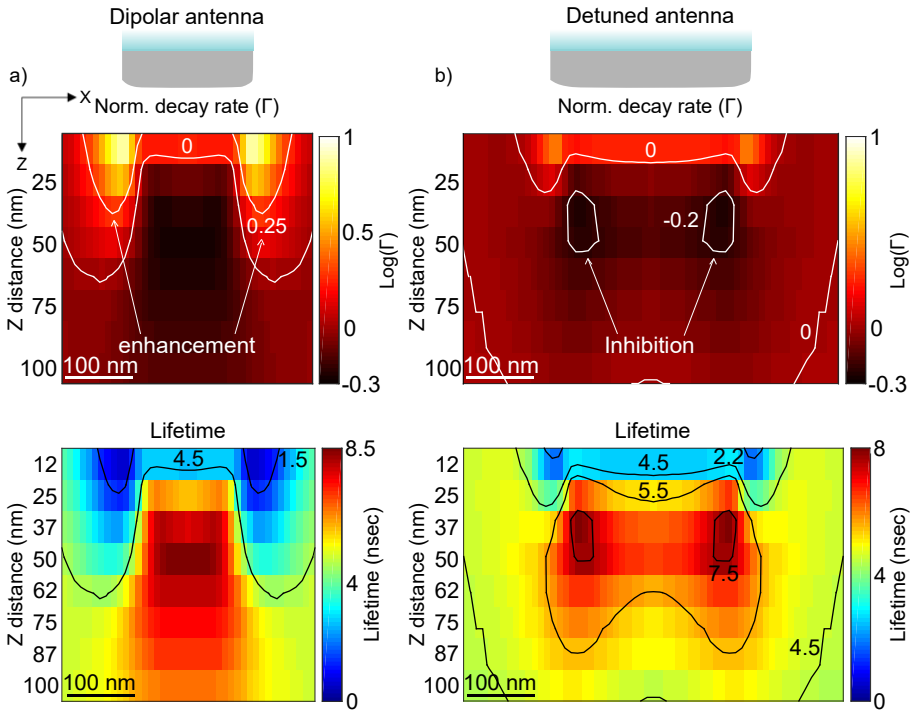

Figure 5.9: Normalized decay rate and lifetime FDTD simulations of a dipolar emitter in close proximity to nanoantennas. (a), (b) FDTD simulated vertical 2D maps of an X oriented emitter positioned under 200 nm dipolar and 300 nm length detuned antennas. The emitter is located under main axis of antennas, oriented parallel to them. At the top and bottom there are respectively the normalized decay rate and the lifetime of the emitter. The lifetime of the emitter alone has been set at 4.5 nsec, its internal quantum efficiency as unity.

However, $I_{x,em}$, the intensity of x-field component emitted by the dipole at 2 nm nanometer distance from it, is already in the order of$\sim 10^{12}$ $(V/m)^2$. Compared to such value, $I_{x,scat} \leq 10^4$ $(V/m)^2$, the intensity of of x-field component scattered by the antenna in close proximity to the emitter, we notice that $I_{x,scat} << I_{x,em}$ because the emitter is x-oriented. Thus we deduce that emission interference on x-field component at molecule position is negligible and doesn't really affect its decay rate.

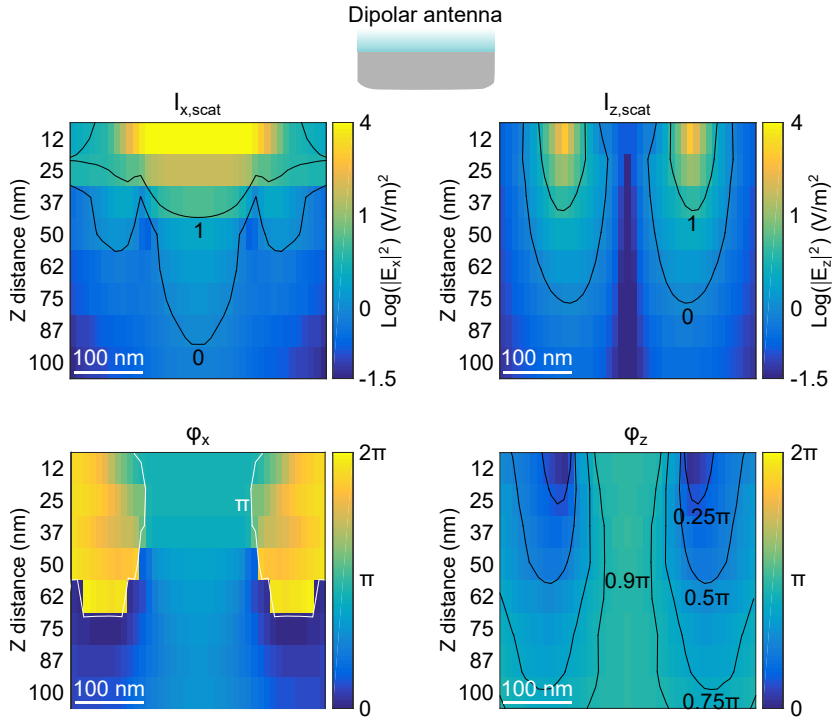

Figure 5.10: FDTD simulations of field intensity and phase scattered by dipolar antenna. (a) Antenna scattered x and z-field intensity and phases calculated by FDTD for an emitter x-oriented, located under the main axis of a 200 nm dipolar antenna. The Y component has been neglected since it is null for symmetry reasons. The decay rate modulations in Figure 5.9 can be explained in terms of constructive/destructive interference between the emitted and scattered z component of the electric field, at the molecule position. Simulations have been performed for a dipole emitting at 780 nm wavelength.

The scattered y-component of field intensity $I_{y,scat}$ has been neglected since it is null for symmetry reasons at dipole position. $I_{z,scat}$ is particularly strong under the antenna ends (Figure 5.10), where ϕ_z is minimal, corresponding to the spots of enhanced rate in Figure 5.9a. Notably, contour lines with $\phi_z \sim \pi$ occur as two distinct contours under the ends of the detuned antenna (Figure 5.11). The spots of inhibition in Figure 5.9b correspond to the internal zones

where the contour $\phi_z \sim \pi$ under antenna and $I_{z,scat}$ is not negligible in Figure 5.11.

Even if $I_{z,em}$ is null at dipole position in our model, it might be non-null in case of a real molecule that has a finite size and where $I_{z,em}$ might have a small non-zero value at molecule position that might interfere with $I_{z,scat}$, constructively in the case of dipolar antenna, destructively in case of detuned antenna.

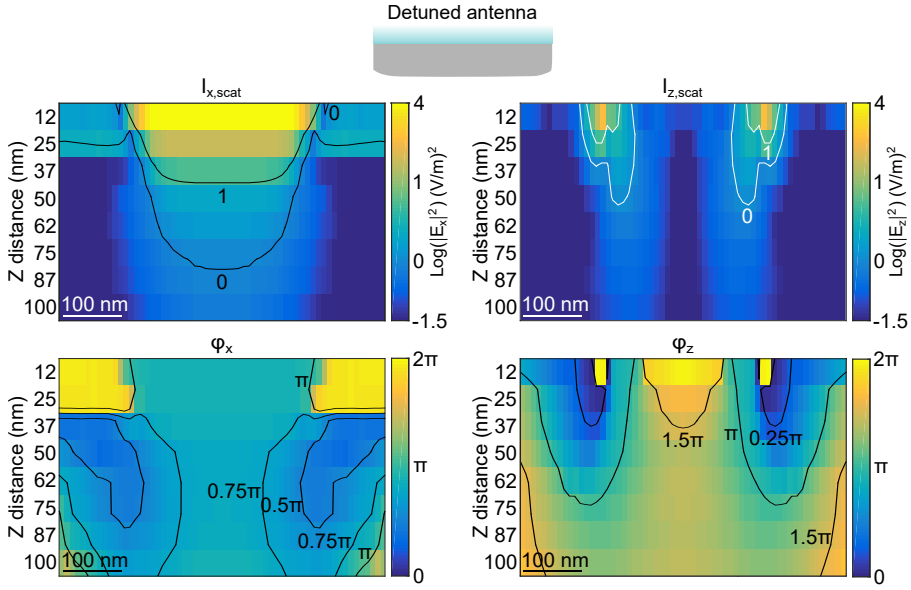

Figure 5.11: FDTD simulations of field intensity and phase scattered by detuned antenna. (a) Antenna scattered x and z-field intensity and phases calculated by FDTD for an emitter x-oriented, located under the main axis of a 300 nm detuned antenna. As in Figure 5.10, here are reported the values corresponding to x and z-components of the field and y-component has been neglected since it is null for symmetry reasons. The decay rate modulations in Figure 5.9 can be explained in terms of constructive/destructive interference between the emitted and scattered z-component of the electric field, at the molecule position. Simulations have been performed for a dipole emitting at 780 nm wavelength.

5.5 Emission coupling high resolution imaging

5.5.1 Emission control through nanoantenna coupling

Finally, we return to the experiment and examine the changes in decay rate in the data presented in Figure 5.7. Panels a and b of Figure 5.12 present fluorescence and lifetime maps of a DBT molecule in close proximity to the 300 nm length detuned antenna. Figure 5.12c shows the lifetime and fluorescence profiles extracted in correspondence of the white lines from a and b. The fluorescence profile shows the cold-spots, with the measured intensity profile minima at a distance of ∼300 nm, matching the calculations. The fluorescence is reduced to 40% corresponding to a DBT molecule at a depth of z = 50 nm.

Figure 5.12b shows the corresponding fluorescence lifetime map.

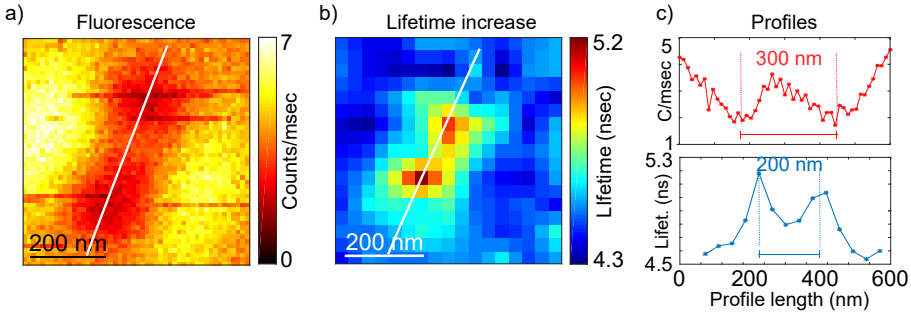

Figure 5.12: Single DBT molecule near-field intensity and lifetime map with a detuned antenna. (a) Fluorescence near-field map of a detuned 300 nm length antenna scanned on a single DBT molecule, we observe the typical two copldspots at a distance of 300 nm. (b) Lifetime image corresponding to the near-field scan reported in (a), the lifetime of the molecule is in average 4.5 nsec. We observe two maxima at a distance of 200 nm with a lifetime increase of 15%. The lifetime map has been obtained time-gating the photons, rejecting the ones with arrival time <0.3 nsec after the laser pulse and then fitting the photon distributions with a single exponential curve. (d) Profiles extracted from (a) and (b) along the white lines.

Remarkably, two spots with increased lifetime show up, i.e., slow decay. At the outer zones of the lifetime map, we find a lifetime of 4.5 ns for the uncoupled case. In the central part with maximum antenna coupling the lifetime gets as long as 5.2 ns, corresponding to an increase of ∼16%. Looking at the lifetime profile along the antenna axis in Figure 5.12c, one appreciates the two slow-decay spots with size 100 nm fwhm, separated by 200 nm. The lifetime profile calculated for an x-oriented emitter located at z = 50 nm shows good agreement, with two spots at a distance of 200 nm from each other. The calculated lifetime increase of 1.5× is larger than measured. Theory assumes a perfect single crystalline antenna and a perfect molecule with 100% quantum efficiency [118]. The nanofabricated polycrystallinity of the antenna and slight non-radiative decay can easily reduce the lifetime enhancement.

5.5.2 Time-gated photon detection and lifetime calculation

Lifetime 2D maps, as the one shown in Figure 5.12b), require the detection of a higher number of photons compared to standard fluorescence imaging. In fact the lifetime extraction at every pixel is based on the fit of photon histograms and in order to get significant values the fit has to be robust and reliable. Our case is additionally complicated by the fact that our detuned 300 nm length antenna has been engineered to provide cold-spots in excitation, hence the amount of photons that we can collect is substantially limited.

In order to overcome this limitation we implemented time-gated photon detection and then calculated lifetime. The idea of time-gated detection is depicted in Figure 5.13a), where a typical photons histogram in logaritmic scale is presented, with photons arrival times taken with respect to the laser pulse (black vertical line), located shortly after zero time. The technique consists in considering only photons arrived into a specific time interval, included between t_{start} and t_{stop}, the green area. In Figure 5.13b) and c) are presented

photons histograms of a coupled and an uncoupled case, with solid lines representing single exponential fits for lifetime calculation. We notice from the fits how the antenna-emitter coupled case shows a longer lifetime.

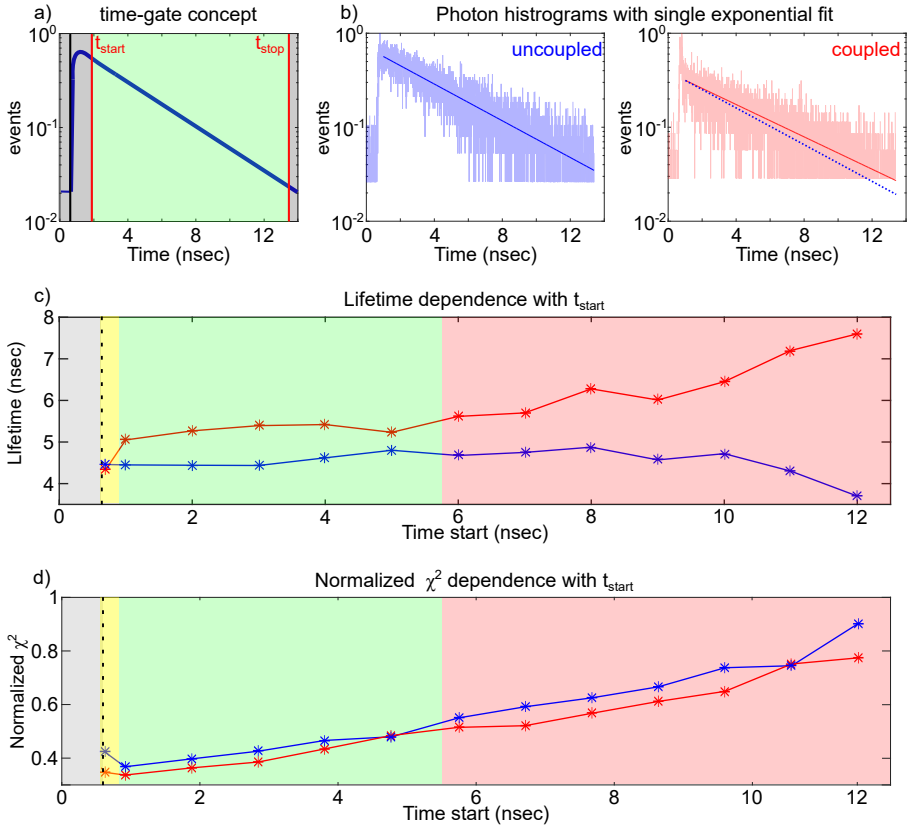

Figure 5.13: Lifetime analysis through time-gating and fit of the photons histogram. Sketch of a typical photons histogram distribution with respect to arrival time. For lifetime calculation, we apply a time-gate and only consider the photons arriving into the interval between tstart and tstop. (b) Photons histograms of an uncoupled and a coupled case. The solid lines represent single exponential fit obtained after rejecting the photons with arrival time <0.3 nsec after the laser pulse. (c) Lifetime graphs of the coupled and uncoupled cases with respect to tstart. (d) Normalized χ^2 dependence with respect to tstart. The green area corresponds to a region where the normalized χ^2 is <0.5.

In the coupled case shown in Figure 5.13b) we also notice the presence of a sharp peak in photons histogram for very small arrival times. Such peak is due to fast antenna metallic self-luminescence, a process that happens in a few hundreds of femtoseconds. Since this contribution is one order of magnitude smaller than a typical single molecule fluorescence as DBT, we don't see it for the uncoupled case in Figure 5.13b). Nevertheless, because of the fact that we deplete excitation in the coupled case with our detuned probe, the molecule emission is also reduced and the antenna self-luminescence peak dominates molecule fluorescence. An effective way to exclude such contribution and retrieve molecular lifetime is to time-gate the data and reject the photons with very short arrival time.

In Figure 5.13c) are reported the lifetimes of the coupled and uncoupled case with respect to t_{start}. Decreasing t_{start} the lifetime values converge to 5.2 nsec and 4.5 nsec, as previously discussed in section 5.5. For $t_{start}<1$ nsec, yellow, area, we notice a strong decrease of coupled case lifetime. This effect is due to the peak located at very short arrival time, due to antenna self-luminescence. Hence we reject such artifact excluding yellow region in lifetime calculation. It is interesting to note how, regardless of t_{start} choice, Figure 5.13c) shows that coupled case lifetime is always longer than uncoupled one, validating our emission inhibition conclusion.

In Figure 5.13d) we plot the trend of normalized χ^2:

$$\frac{\chi^2}{N} = \frac{\sum_{k=1}^{N} \frac{(M^k - C^k)^2}{C^k}}{N} \tag{5.1}$$

with respect to t_{start}, where M and C are respectively the measured and calculated values, and N is the number of time measurements. Such graph shows how decreasing t_{start} we also decrease normalized χ^2, improving fitting precision. The green area in Figure 5.13d) corresponds to normalized $\chi^2<0.5$, therefore presents more stable fitting results than the red one. The normalized χ^2

minimum is found for t_{start}=1 nsec, that is the time-gating parameter that we have chosen for lifetime calculation reported in Figure 5.12b). The analysis of lifetime calculation reported in Figure 5.12 supports data presented in section 5.5, with the conclusion that our detuned antenna can induce partial emission inhibition on a single DBT molecule.

5.5.3 Data modeling through emission analysis

In section 5.5 we estimated $d_z \sim 50$ nm as z antenna-molecule distance for data reported in Figure 5.12b). We can now perform FDTD lifetime and scattered field intensity simulations for such specific d_z value in order to fit data.

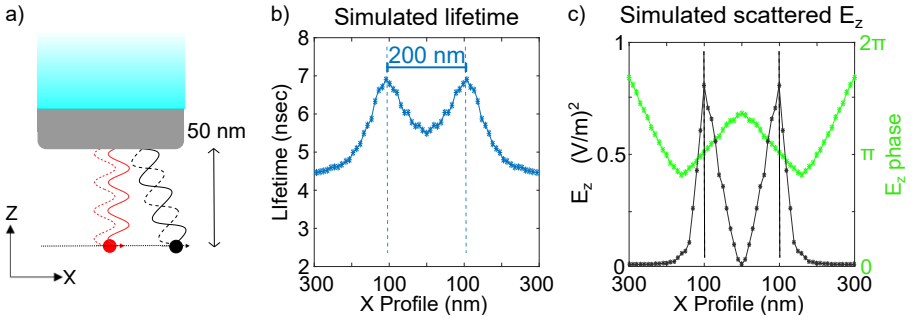

Figure 5.14: Modeling of emission inhibition shown by data. (a) Sketch of a dipole emitting in close proximity to a nanoantenna. The size of the wavelength has been reduced for the sake of clarity. (b) Lifetime profile obtained at a z distance of 50 nm under the antenna by FDTD simulation. It shows the presence of two maxima at a distance of 200 nm. (c) Profiles of the scattered z-component of the electric field for the same antenna-emitter z distance. The z component of the field shows two maxima at a distance of 200 nm, with a phase of π. Simulations have been performed for a dipole emitting at 780 nm wavelength.

Figure 5.14a) shows a sketch of a nanoantenna with two dipolar emitters at 50 nm vertical distance, but different x positions. In solid and discontinuous lines there are represented emitted and

scattered light. The size of wavelength has been decreased with respect to antenna for the sake of clarity. The idea is that at a fixed d_z, depending on emitter position, it can experience constructive or destructive interference with a direct effect on decay rate. Figure 5.14b) shows a FDTD simulated lifetime horizontal profile of an X oriented dipolar emitter located 50 nm under antenna. It shows the presence of two spots with increased lifetime of ∼1.5x, at a distance of ∼200 nm. Such result is in good qualitative agreement with data shown in Figure 5.12b), where we observe two spots at ∼200 nm distance. In Figure 5.14c) we report scattered z-field intensity and phase ϕ_z horizontal profiles at different dipole positions and at the same d_z. Scattered z-field intensity exhibits two maxima at a distance of ∼200 nm, where we previously found lifetime maxima. At such positions the scattered $\phi_z \sim \pi$, suggesting that z-component of scattered light is strongly out-of-phase with emitted one at emitter position. Our calculations confirm that the measured lifetime maxima, hence the partial emission inhibition, reported in our data in Figure 5.12b) is due to z-field destructive interference between emitted and antenna-scattered light at single DBT molecule position.

5.6 Conclusion

In conclusion, we have presented a first complete study on the use of local phase to control the nanoantenna coupling to a single photon emitter, both in excitation and emission. Varying the length of a nanorod antenna, we tuned away from resonance, to control the local phase. Exploiting near-field interference, we designed local zones with suppressed fields and decreased LDOS.

On the excitation side, we have shown for the first time a direct, optical visualization of subwavelength cold-spots, with excitation intensity reduced to percent level, mapped with high resolution (50

nm) using a single molecule. By tuning the antenna off and on resonance the interference switches from cold to hot-spot generation. Together with hot-spots, the cold-spots provide strong field contrast with high resolution and allow to enhance the dynamic range to 3 orders of magnitude. They constitute alternative building blocks for full light manipulation at the nanoscale.

On the emission side, we have presented the first inhibition of spontaneous emission of a single molecule mediated by a metallic nanoantenna: slow-decay spots, with a lifetime increase by a factor 16%. Compared to the inhibition close to a metallic surface (Drexhage3) or in a photonic crystal defect cavity [55, 104–106], here we achieve inhibition in a sub-wavelength volume. It is remarkable, that inhibition does occur in such an open and lossy nanoantenna-cavity system [119].

The cold spots are an attractive alternative to high-resolution microscopy. Particularly, for localization microscopy of rapidly bleaching labels, the cold spots can act as a near-field alternative to the far-field MINFLUX super-resolution microscopy [51], with the advantage of superior resolution due to the sub-wavelength spatial response. Beyond high-resolution imaging, since cold-spots provide an almost completely dark area located inside a diffraction limited confocal spot, they might find application in study of energy transfer at the nanoscale. Additionally, the capability to influence the decay rate of a single photon emitter might be used to actively manipulate energy transfer at the nanoscale, with the potential to change energy paths in complex multi-chromophoric systems. Finally, the possibility to switch between hot and cold-spots tuning antenna phase provides a direct knob for electric field gradients control at the subwavelength scale, with possible applications in the field of optical trapping and particles manipulation.

Chapter 6

Conclusion

In this thesis I have described our efforts towards the active manipulation of SPEs by deterministic coupling with plasmonic nanoantennas. Our approach involved the design and fabrication of nanoantennas at the end of a fiber tip, scanned in close proximity to a single SPE using scanning near-field microscopy. This allowed us to have deterministic coupling with nanometer precision and controlled distance and relative orientation.

Our work demonstrated that it is possible to have a resonant near-field probe and at the same time provide enhanced, high resolution imaging with a single spot per emitter. We showed how using cutting edge nanofabrication facilities like a helium FIB it is in principle possible to push even further the level of light confinement and localization down to a few nanometers FWHM and theoretically three orders of magnitude excitation enhancement. Our results leave space for further increase of light confinement that might surely be beneficial for the study of extremely small natural molecular systems like photosynthetic membranes.

Our near-field high resolution imaging and emission control on hBN defects has been the first experimental demonstration that scanning antenna technology can be successfully applied to expand the knowledge of novel emitters where sub-wavelength resolution is required. Compared to classical far-field super resolution techniques, our approach provides an additional degree of freedom, the capability to modify the optical properties of the emitter. Nevertheless, we realized that working with novel SPEs in 2D materials also brings additional challenges, mainly due to the high refractive

index of the material itself. Such limitations may be overcome with specific control on material thickness, by index matching or solid immersion, and using advanced techniques as time-gated photon detection.

Finally, using well-established single molecules samples, we showed for the first time that the use of nanoantennas for SPEs manipulation provides the possibility to engineer the local phase of an antenna probe by length control, which allows to switch between enhancement (hot-spots) and suppression (cold-spots) of the excitation field, on a sub-wavelength scale with orders of magnitude of dynamic range. At the same time, antenna phase engineering can be exploited for emission control of an emitter. Remarkably we proved experimentally that it can provide emission inhibition despite the well-know lossy behaviour of metallic nanoantennas. Our first optical visualization of cold-spots paves the way to the miniaturization of far-field based super resolution localization techniques, with interesting potential for imaging rapidly bleaching emitters or particle trapping.

Bibliography

1. Lounis, B. & Orrit, M. Single-photon sources. *Reports on Progress in Physics* **68,** 1129 (2005).
2. McKeever, J. *et al.* Deterministic generation of single photons from one atom trapped in a cavity. *Science* **303,** 1992–1994 (2004).
3. Hennrich, M., Legero, T., Kuhn, A. & Rempe, G. Photon statistics of a non-stationary periodically driven single-photon source. *New Journal of Physics* **6,** 86 (2004).
4. Keller, M., Lange, B., Hayasaka, K., Lange, W. & Walther, H. Continuous generation of single photons with controlled waveform in an ion-trap cavity system. *Nature* **431,** 1075–1078 (2004).
5. Maurer, C., Becher, C., Russo, C., Eschner, J. & Blatt, R. A single-photon source based on a single Ca+ ion. *New journal of physics* **6,** 94 (2004).
6. Lounis, B. & Moerner, W. E. Single photons on demand from a single molecule at room temperature. *Nature* **407,** 491–493 (2000).
7. Lombardi, P. *et al.* Photostable molecules on chip: integrated sources of nonclassical light. *ACS Photonics* **5,** 126–132 (2018).
8. Schmidt, M. *et al.* Deterministically fabricated spectrally-tunable quantum dot based single-photon source. *Optical Materials Express* **10,** 76–87 (2020).
9. Tamariz, S. *et al.* Toward bright and pure single photon emitters at 300 K based on GaN quantum dots on silicon. *Acs Photonics* **7,** 1515–1522 (2020).
10. Kurtsiefer, C., Mayer, S., Zarda, P. & Weinfurter, H. Stable solid-state source of single photons. *Physical review letters* **85,** 290 (2000).

11. Wu, E *et al.* Room temperature triggered single-photon source in the near infrared. *New Journal of Physics* **9,** 434 (2007).
12. Tran, T., Bray, K., Ford, M., Toth, M. & Aharonovich, I. Quantum emission from hexagonal boron nitride monolayers. *Nature nanotechnology* **11,** 37 (2016).
13. Koperski, M. *et al.* Single photon emitters in exfoliated WSe 2 structures. *Nature nanotechnology* **10,** 503–506 (2015).
14. Eisaman, M. D., Fan, J., Migdall, A. & Polyakov, S. V. Invited review article: Single-photon sources and detectors. *Review of scientific instruments* **82,** 071101 (2011).
15. Aharonovich, I., Englund, D. & Toth, M. Solid-state single-photon emitters. *Nature Photonics* **10,** 631–641 (2016).
16. Moerner, W. E. & Kador, L. Optical detection and spectroscopy of single molecules in a solid. *Physical review letters* **62,** 2535 (1989).
17. Novotny, L. & Hecht, B. *Principles of nano-optics* (Cambridge university press, 2012).
18. Purcell, E. M. Spontaneous Emission Probabilities at Radio Frequencies. *Phys. Rev.* **69,** 681 (1946).
19. Hugall, J., Singh, A. & van Hulst, N. F. Plasmonic cavity coupling. *Acs Photonics* **5,** 43–53 (2018).
20. Akselrod, G. M. *et al.* Probing the mechanisms of large Purcell enhancement in plasmonic nanoantennas. *Nature Photonics* **8,** 835–840 (2014).
21. Hoang, T., Akselrod, G. & Mikkelsen, M. Ultrafast room-temperature single photon emission from quantum dots coupled to plasmonic nanocavities. *Nano letters* **16,** 270–275 (2015).
22. Hoang, T. B. *et al.* Ultrafast spontaneous emission source using plasmonic nanoantennas. *Nature communications* **6,** 1–7 (2015).

23. Greffet, J.-J. Nanoantennas for light emission. *Science* **308,** 1561–1563 (2005).
24. Novotny, L. & Van Hulst, N. Antennas for light. *Nature photonics* **5,** 83–90 (2011).
25. Muehlschlegel, P., Eisler, H.-J., Martin, O. J., Hecht, B & Pohl, D. Resonant optical antennas. *Science* **308,** 1607–1609 (2005).
26. Taminiau, T., Stefani, F., Segerink, F. & Van Hulst, N. Optical antennas direct single-molecule emission. *Nature photonics* **2,** 234–237 (2008).
27. Singh, A., Hugall, J., Calbris, G. & van Hulst, N. F. Fiber-based optical nanoantennas for single-molecule imaging and sensing. *Journal of Lightwave Technology* **33,** 2371–2377 (2015).
28. Mivelle, M., van Zanten, T. & Garcia-Parajo, M. Hybrid photonic antennas for subnanometer multicolor localization and nanoimaging of single molecules. *Nano letters* **14,** 4895–4900 (2014).
29. Singh, A., Calbris, G. & van Hulst, N. F. Vectorial nanoscale mapping of optical antenna fields by single molecule dipoles. *Nano letters* **14,** 4715–4723 (2014).
30. Vahala, K. J. Optical microcavities. *Nature* **424,** 839–846 (2003).
31. Koenderink, A. F. Single-photon nanoantennas. *ACS photonics* **4,** 710–722 (2017).
32. Wientjes, E., Renger, J., Curto, A., Cogdell, R. & Van Hulst, N. F. Strong antenna-enhanced fluorescence of a single light-harvesting complex shows photon antibunching. *Nature communications* **5,** 4236 (2014).
33. Wientjes, E., Renger, J., Cogdell, R. & van Hulst, N. F. Pushing the photon limit: nanoantennas increase maximal photon stream and total photon number. *The journal of physical chemistry letters* **7,** 1604–1609 (2016).

34. Saemisch, L., Liebel, M. & van Hulst, N. F. Isolating strong nanoantenna–molecule interactions by ensemble-level single-molecule detection. *Nanoscale* **12,** 3723–3730 (2020).
35. Acuna, G. *et al.* Fluorescence enhancement at docking sites of DNA-directed self-assembled nanoantennas. *Science* **338,** 506–510 (2012).
36. Shen, B., Kostiainen, M. A. & Linko, V. DNA origami nanophotonics and plasmonics at interfaces. *Langmuir* **34,** 14911–14920 (2018).
37. Busson, M. P., Rolly, B., Stout, B., Bonod, N. & Bidault, S. Accelerated single photon emission from dye molecule-driven nanoantennas assembled on DNA. *Nature communications* **3,** 1–6 (2012).
38. Luo, Y. *et al.* Deterministic coupling of site-controlled quantum emitters in monolayer WSe 2 to plasmonic nanocavities. *Nature nanotechnology* **13,** 1137–1142 (2018).
39. Curto, A. G. *et al.* Unidirectional emission of a quantum dot coupled to a nanoantenna. *Science* **329,** 930–933 (2010).
40. Nguyen, M. *et al.* Nanoassembly of quantum emitters in hexagonal boron nitride and gold nanospheres. *Nanoscale* **10,** 2267–2274 (2018).
41. Andersen, S. K., Kumar, S. & Bozhevolnyi, S. I. Ultrabright linearly polarized photon generation from a nitrogen vacancy center in a nanocube dimer antenna. *Nano letters* **17,** 3889–3895 (2017).
42. Michaelis, J, Hettich, C., Mlynek, J & Sandoghdar, V. Optical microscopy using a single-molecule light source. *Nature* **405,** 325–328 (2000).
43. Frimmer, M., Chen, Y. & Koenderink, A. F. Scanning emitter lifetime imaging microscopy for spontaneous emission control. *Physical Review Letters* **107,** 123602 (2011).

44. Singh, A., de Roque, P., Calbris, G., Hugall, J. & van Hulst, N. Nanoscale mapping and control of antenna-coupling strength for bright single photon sources. *Nano letters* **18,** 2538–2544 (2018).
45. Kianinia, M. *et al.* Robust solid-state quantum system operating at 800 K. *Acs Photonics* **4,** 768–773 (2017).
46. Feng, J. *et al.* Imaging of optically active defects with nanometer resolution. *Nano letters* **18,** 1739–1744 (2018).
47. Tran, T. *et al.* Deterministic coupling of quantum emitters in 2D materials to plasmonic nanocavity arrays. *Nano letters* **17,** 2634–2639 (2017).
48. Palombo Blascetta, N. *et al.* Nanoscale Imaging and Control of Hexagonal Boron Nitride Single Photon Emitters by a Resonant Nanoantenna. *Nano Letters* **20,** 1992–1999 (2020).
49. Buchler, B., Kalkbrenner, T, Hettich, C & Sandoghdar, V. Measuring the quantum efficiency of the optical emission of single radiating dipoles using a scanning mirror. *Physical review letters* **95,** 063003 (2005).
50. Johnson, T. *et al.* Highly reproducible near-field optical imaging with sub-20-nm resolution based on template-stripped gold pyramids. *ACS nano* **6,** 9168–9174 (2012).
51. Balzarotti, F. *et al.* Nanometer resolution imaging and tracking of fluorescent molecules with minimal photon fluxes. *Science* **355,** 606–612 (2017).
52. Haggui, M. *et al.* Spatial confinement of electromagnetic hot and cold spots in gold nanocubes. *Acs Nano* **6,** 1299–1307 (2012).
53. Drexhage, K. Beeinflussung der Fluoreszenz eins Europiumchelates durch einen Spiegel. *Ber. Bunsenges. Phys. Chem.* **70,** 1179 (1966).
54. Kühn, S., Håkanson, U., Rogobete, L. & Sandoghdar, V. Enhancement of single-molecule fluorescence using a gold nanoparticle as an optical nanoantenna. *Physical review letters* **97,** 017402 (2006).

55. Lodahl, P. *et al.* Controlling the dynamics of spontaneous emission from quantum dots by photonic crystals. *Nature* **430,** 654–657 (2004).
56. Palombo Blascetta, N., Lombardi, P., Toninelli, C. & van Hulst, N. F. Cold and Hot Spots: from Inhibition to Enhancement by Nanoscale Phase Tuning of Optical Nanoantennas. *Nano Letters* (2020).
57. Kinkhabwala, A. *et al.* Large single-molecule fluorescence enhancements produced by a bowtie nanoantenna. *Nature Photonics* **3,** 654–657 (2009).
58. Punj, D. *et al.* A plasmonic 'antenna-in-box'platform for enhanced single-molecule analysis at micromolar concentrations. *Nature nanotechnology* **8,** 512 (2013).
59. Saemisch, L., Liebel, M. & van Hulst, N. F. Control of Vibronic Transition Rates by Resonant Single-Molecule-Nanoantenna Coupling. *Nano Letters* (2020).
60. Blauth, M. *et al.* Coupling single photons from discrete quantum emitters in WSe2 to lithographically defined plasmonic slot waveguides. *Nano letters* **18,** 6812–6819 (2018).
61. Proscia, N. V. *et al.* Near-deterministic activation of room-temperature quantum emitters in hexagonal boron nitride. *Optica* **5,** 1128–1134 (2018).
62. Bidault, S. *et al.* Picosecond lifetimes with high quantum yields from single-photon-emitting colloidal nanostructures at room temperature. *ACS nano* **10,** 4806–4815 (2016).
63. Anger, P., Bharadwaj, P. & Novotny, L. Enhancement and quenching of single-molecule fluorescence. *Physical review letters* **96,** 113002 (2006).

64. Neumann, L., van't Oever, J. & van Hulst, N. F. A resonant scanning dipole-antenna probe for enhanced nanoscale imaging. *Nano letters* **13,** 5070–5074 (2013).
65. Rodrigo, S. G., García-Vidal, F. & Martín-Moreno, L. Influence of material properties on extraordinary optical transmission through hole arrays. *Physical Review B* **77,** 075401 (2008).
66. Albrecht, G., Ubl, M., Kaiser, S., Giessen, H. & Hentschel, M. Comprehensive study of plasmonic materials in the visible and near-infrared: linear, refractory, and nonlinear optical properties. *Acs Photonics* **5,** 1058–1067 (2018).
67. Kollmann, H. *et al.* Toward plasmonics with nanometer precision: nonlinear optics of helium-ion milled gold nanoantennas. *Nano letters* **14,** 4778–4784 (2014).
68. Mais, S. *et al.* Terrylenediimide: A novel fluorophore for single-molecule spectroscopy and microscopy from 1.4 K to room temperature. *The Journal of Physical Chemistry A* **101,** 8435–8440 (1997).
69. Toninelli, C. *et al.* Near-infrared single-photons from aligned molecules in ultrathin crystalline films at room temperature. *Optics express* **18,** 6577–6582 (2010).
70. Xu, Z. *et al.* Single photon emission from plasma treated 2D hexagonal boron nitride. *Nanoscale* **10,** 7957–7965 (2018).
71. Choi, S. *et al.* Engineering and localization of quantum emitters in large hexagonal boron nitride layers. *ACS applied materials & interfaces* **8,** 29642–29648 (2016).
72. Tran, T. *et al.* Robust multicolor single photon emission from point defects in hexagonal boron nitride. *ACS nano* **10,** 7331–7338 (2016).
73. Rabouw, F. T. *et al.* Non-blinking single-photon emitters in silica. *Scientific reports* **6,** 21187 (2016).

74. Wahl, M., Rahn, H., Gregor, I., Erdmann, R. & Enderlein, J. Dead-time optimized time-correlated photon counting instrument with synchronized, independent timing channels. *Review of Scientific Instruments* **78,** 033106 (2007).

75. Betzig, E. & Chichester, R. Single molecules observed by near-field scanning optical microscopy. *Science* **262,** 1422–1425 (1993).

76. Veerman, J., Garcia-Parajo, M., Kuipers, L & Van Hulst, N. Single molecule mapping of the optical field distribution of probes for near-field microscopy. *Journal of microscopy* **194,** 477–482 (1999).

77. Matsuzaki, K. *et al.* Strong plasmonic enhancement of biexciton emission: controlled coupling of a single quantum dot to a gold nanocone antenna. *Scientific reports* **7,** 42307 (2017).

78. Ernandes, C. *et al.* Exploring the magnetic and electric side of light through plasmonic nanocavities. *Nano letters* **18,** 5098–5103 (2018).

79. Mivelle, M., van Zanten, T., Neumann, L., van Hulst, N. & Garcia-Parajo, M. Ultrabright bowtie nanoaperture antenna probes studied by single molecule fluorescence. *Nano letters* **12,** 5972–5978 (2012).

80. Chikkaraddy, R. *et al.* Single-molecule strong coupling at room temperature in plasmonic nanocavities. *Nature* **535,** 127–130 (2016).

81. Guo, X. *et al.* Shell-dependent blinking behavior and fluorescence dynamics of single ZnSe/CdS core/shell quantum dots. *Nanoscale* **10,** 18696–18705 (2018).

82. Petrakova, V. *et al.* Luminescence properties of engineered nitrogen vacancy centers in a close surface proximity. *Physica status solidi (a)* **208,** 2051–2056 (2011).

83. He, Y.-M. *et al.* Single quantum emitters in monolayer semiconductors. *Nature nanotechnology* **10,** 497–502 (2015).

84. Aspuru-Guzik, A. & Walther, P. Photonic quantum simulators. *Nature physics* **8,** 285 (2012).

85. Lo, H., Curty, M. & Tamaki, K. Secure quantum key distribution. *Nature Photonics* **8,** 595 (2014).

86. Reimer, M. *et al.* Bright single-photon sources in bottom-up tailored nanowires. *Nature communications* **3,** 737 (2012).

87. Lombardi, P. *et al.* Photostable molecules on chip: integrated sources of nonclassical light. *ACS Photonics* **5,** 126–132 (2017).

88. Doherty, M. W. *et al.* The nitrogen-vacancy colour centre in diamond. *Physics Reports* **528,** 1–45 (2013).

89. Hepp, C. *et al.* Electronic structure of the silicon vacancy color center in diamond. *Physical Review Letters* **112,** 036405 (2014).

90. Siampour, H., Kumar, S. & Bozhevolnyi, S. I. Chip-integrated plasmonic cavity-enhanced single nitrogen-vacancy center emission. *Nanoscale* **9,** 17902–17908 (2017).

91. Katsumi, R. *et al.* Quantum-dot single-photon source on a CMOS silicon photonic chip integrated using transfer printing. *APL Photonics* **4,** 036105 (2019).

92. Liu, J. *et al.* A solid-state source of strongly entangled photon pairs with high brightness and indistinguishability. *Nature nanotechnology* **14,** 586–593 (2019).

93. Martinez, L. *et al.* Efficient single photon emission from a high-purity hexagonal boron nitride crystal. *Physical Review B* **94,** 121405 (2016).

94. Tawfik, S. *et al.* First-principles investigation of quantum emission from hBN defects. *Nanoscale* **9,** 13575–13582 (2017).

95. Exarhos, A., Hopper, D., Grote, R., Alkauskas, A. & Bassett, L. Optical signatures of quantum emitters in suspended hexagonal boron nitride. *ACS nano* **11,** 3328–3336 (2017).

96. Lee, S., Jeong, T., Jung, S. & Yee, K. Refractive Index Dispersion of Hexagonal Boron Nitride in the Visible and Near-Infrared. *Physica status solidi (b)* **256,** 1800417 (2019).

97. Schell, A., Svedendahl, M. & Quidant, R. Quantum emitters in hexagonal boron nitride have spectrally tunable quantum efficiency. *Advanced Materials* **30,** 1704237 (2018).

98. Nikolay, N. *et al.* Direct measurement of quantum efficiency of single-photon emitters in hexagonal boron nitride. *Optica* **6,** 1084–1088 (2019).

99. Ziegler, J. *et al.* Deterministic Quantum Emitter Formation in Hexagonal Boron Nitride via Controlled Edge Creation. *Nano letters* **19,** 2121–2127 (2019).

100. Purcell, E. M. Spontaneous emission probabilities at radio frequencies. *Phys. Rev.* **69** (1946).

101. Drexhage, K. Influence of a dielectric interface on fluorescence decay time. *Journal of luminescence* **1,** 693–701 (1970).

102. Chizhik, A. I. *et al.* Probing the radiative transition of single molecules with a tunable microresonator. *Nano letters* **11,** 1700–1703 (2011).

103. Frimmer, M., Mohtashami, A. & Femius Koenderink, A. Nanomechanical method to gauge emission quantum yield applied to nitrogen-vacancy centers in nanodiamond. *Applied Physics Letters* **102,** 121105 (2013).

104. Yablonovitch, E. Inhibited spontaneous emission in solid-state physics and electronics. *Physical review letters* **58,** 2059 (1987).

105. John, S. Strong localization of photons in certain disordered dielectric superlattices. *Physical review letters* **58,** 2486 (1987).

106. Fujita, M., Takahashi, S., Tanaka, Y., Asano, T. & Noda, S. Simultaneous inhibition and redistribution of spontaneous light emission in photonic crystals. *Science* **308,** 1296–1298 (2005).

107. Jakubczyk, T. *et al.* Inhibition and enhancement of the spontaneous emission of quantum dots in micropillar cavities with radial-distributed Bragg reflectors. *ACS nano* **8,** 9970–9978 (2014).

108. Frimmer, M. & Koenderink, A. F. Spontaneous emission control in a tunable hybrid photonic system. *Physical review letters* **110,** 217405 (2013).

109. Ozelci, E. *et al.* Quantitative measurements of the pH-sensitive quantum yield of fluorophores in mesoporous silica thin films using a drexhage-type experiment. *The Journal of Physical Chemistry C* **123,** 20468–20475 (2019).

110. Hoang, T. B., Akselrod, G. M. & Mikkelsen, M. H. Ultrafast room-temperature single photon emission from quantum dots coupled to plasmonic nanocavities. *Nano letters* **16,** 270–275 (2016).

111. Bouchet, D. *et al.* Enhancement and inhibition of spontaneous photon emission by resonant silicon nanoantennas. *Physical Review Applied* **6,** 064016 (2016).

112. Hoogenboom, J. P. *et al.* The single molecule probe: nanoscale vectorial mapping of photonic mode density in a metal nanocavity. *Nano letters* **9,** 1189–1195 (2009).

113. Istrate, E. & Sargent, E. H. Measurement of the phase shift upon reflection from photonic crystals. *Applied Physics Letters* **86,** 151112 (2005).

114. Arcari, M. *et al.* Near-unity coupling efficiency of a quantum emitter to a photonic crystal waveguide. *Physical review letters* **113,** 093603 (2014).

115. Lecamp, G, Lalanne, P & Hugonin, J. Very large spontaneous-emission β factors in photonic-crystal waveguides. *Physical review letters* **99,** 023902 (2007).

116. Yu, N. *et al.* Light propagation with phase discontinuities: generalized laws of reflection and refraction. *Science* **334,** 333–337 (2011).

117. Nicolet, A. A. *et al.* Single dibenzoterrylene molecules in an anthracene crystal: main insertion sites. *ChemPhysChem* **8,** 1929–1936 (2007).

118. Major, K. D. *et al.* Growth of optical-quality anthracene crystals doped with dibenzoterrylene for controlled single photon production. *Review of Scientific Instruments* **86,** 083106 (2015).

119. Hadad, Y. & Engheta, N. Possibility for inhibited spontaneous emission in electromagnetically open parity–time-symmetric guiding structures. *Proceedings of the National Academy of Sciences* **117,** 5576–5581 (2020).